

THÈSE DE DOCTORAT

Présentée à

l'Université du Maine

spécialité:

Physique

par

Alina Daniela CRISAN

Pour obtenir le grade de DOCTEUR de l'UNIVERSITÉ DU MAINE

et

DOCTEUR de l'UNIVERSITÉ de BUCAREST

SYNTHÈSE ET CARACTÉRISATION DES ALLIAGES
MAGNÉTIQUES NANOSTRUCTURÉS
À BASE DE FePt

Soutenue le 5 Février 2009 devant la commission d'examen:

M. Jean-Marc GRENÈCHE

M. Jean-Marie LE BRETON

M. Voicu GRECU

M. Nirina RANDRIANANTOANDRO

M. Mircea MORARIU

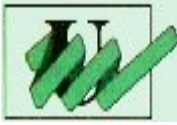
Directeur de Recherche, Université du Maine (Président)

Professeur, Université de Rouen (Rapporteur)

Professeur, Université de Bucarest (Rapporteur)

Professeur, Université du Maine (Directeur de thèse)

Professeur, INPM Bucarest (Co-directeur de thèse)



*Laboratoire de Physique de l'Etat Condensé, UMR CNRS 6087,
Université du Maine. Le Mans. France*

**National Institute
of Materials Physics**



*National Institute for Materials Physics,
Bucharest-Magurele, Romania*

*Synthesis and characterisation
of nanostructured magnetic
FePt-based alloys*

Drd. Alina Daniela Crisan

Coordinators:

Prof. Dr. Nirina Randrianantoandro

Prof. Dr. Mircea Morariu

Acknowledgements

- I wish to express my profound gratitude to Prof. N. Randrianantoandro, Director of the thesis, for his guidance, advices and all the scientific training I benefit from, throughout this thesis. His priceless contribution in performing Mossbauer and magnetic analysis was extremely valuable and helped me a lot for the understanding of the phenomena involved in exchange spring magnets.

- I express also my entire gratitude to Prof. M. Morariu, Co-Director of the thesis, for the loads of knowledge regarding solid state physics and notably the Mossbauer spectrometry technique and many valuable discussions that he shared with me during the 5 years of working together at the NIMP, Bucharest.

- Prof. M. Grecu and Prof. J.M. Le Breton made me the honor to report on the present work and to be members of the jury. Their reports helped me to improve the quality of my results and the way they are presented. I wish to express here my gratitude to them.

- I also wish to express my gratitude to Dr. J.M. Grenèche, Director of Research, for his valuable help regarding the interpretation of Mossbauer spectrometry results and for many fruitful advices he gave me during this thesis and especially for the thesis defense.

- I express my deep gratitude to Prof. I. Skorvanek, Kosice, J.M.D. Coey, Dublin, O. Cador and F. Grasset, Rennes for the magnetic measurements and annealing the samples, to A.M. Mercier, Le Mans for X-ray diffraction measurements, and C. Galven, Le Mans for densitometry and EDX results. I acknowledge the precious work of P. Svec, Bratislava regarding the transmission electron microscopy images, E. Burkel and R. Nicula, Rostock and Hamburg, for the help in performing DSC and in-situ X-ray diffraction of synchrotron radiation. I wish to express my deep gratitude to Prof. M. Valeanu, Bucharest, for her priceless advices regarding the world of magnetic materials and valuable discussions regarding my results. I also acknowledge the precious help from my colleagues in Bucharest, M. Sofronie and F. Lifei for the help in the ribbons synthesis and the good atmosphere during my 5 years of activity at NIMP.

- My deepest sentiments go towards my parents and my family, daughter Nereia and husband Ovidiu. Without their constant warm presence and encouragements this work would not have been possible.

Table of contents:

Introduction	6
Chapter 1: State of the art	7
Chapter 2: Synthesis and characterization of as cast FePtNbB ribbons	17
2.1 The Fe-Pt-Nb-B alloys.....	17
2.1.1 FePt binary phase diagram.....	17
2.1.2 Choice of chemical composition.....	19
2.2 Synthesis of the Fe-Pt-Nb-B ribbons.....	22
2.2.1 Choice of the synthesis method.....	22
2.2.2 The principle of method of the rapid solidification from the melt.....	25
2.2.3 Experimental procedure of synthesis.....	27
2.3 Structural characterization of as-cast ribbons.....	28
2.3.1 Experimental techniques of characterization.....	28
2.3.2. Elemental characterization of as-cast state by energy dispersive X-ray spectroscopy (EDX)..	34
2.3.3. X-ray diffraction (XRD)	35
2.3.3.1. Fitting methods.....	35
2.3.3.2. Experimental XRD results.....	39
2.3.4. As-cast state characterization by Mössbauer spectrometry	44
2.3.5. Magnetic characterization of the as-cast state by Vibrating sample Magnetometry (VSM).....	52
2.4 Thermal analysis.....	55
2.5 Formation and evolution of nanocrystalline magnetic phases in FePtNbB: <i>in situ</i> temperature dependent synchrotron XRD study.....	65
2.5.1 Characteristics of synchrotron radiation and schematics of synchrotron X-ray diffraction experiments.....	65
2.5.2 Temperature and pressure driven disorder-order phase evolution in FePtNbB.....	69
Chapter 3: Structural characterization of annealed Fe-Pt-Nb-B ribbons	80
3.1 Isothermal annealing and phase structure of Fe rich ribbons.....	80
3.1.1 Case of crystalline samples.....	81
3.1.2 Case of disordered sample.....	82
3.2 Isothermal annealing of Pt – rich alloys.....	91
3.2.1 Modifications in the chemical compositions of the FePtNbB alloys: structural effects.....	91
3.2.2 Choice of the annealing conditions.....	92

3.3. Phase structure of the annealed Pt – rich alloys.....	94
3.3.1 XRD studies.....	94
3.3.2 Transmission electron microscopy.....	97
3.3.3 Mössbauer spectrometry on annealed ribbons. Identification of the Phase structures.....	100
Chapter 4: Magnetic properties of the $\text{Fe}_{51}\text{Pt}_{27}\text{Nb}_2\text{B}_{20}$ and $\text{Fe}_{52}\text{Pt}_{28}\text{Nb}_2\text{B}_{18}$ annealed ribbons.	
Exchange spring effects and energy product for exchange coupled magnets.....	110
4.1 Hysteresis loops for the $\text{Fe}_{51}\text{Pt}_{27}\text{Nb}_2\text{B}_{20}$ and $\text{Fe}_{52}\text{Pt}_{28}\text{Nb}_2\text{B}_{18}$ annealed ribbons...	110
4.1.1 $\text{Fe}_{51}\text{Pt}_{27}\text{Nb}_2\text{B}_{20}$ annealed ribbons.....	110
4.1.2 $\text{Fe}_{52}\text{Pt}_{28}\text{Nb}_2\text{B}_{18}$ annealed ribbons.....	114
4.2 The exchange spring magnet criteria. Reversibility effects.....	117
Conclusions.....	121
Perspectives.....	123
References.....	125
Annex I.....	129
Annex II.....	138
Annex III.....	140

Introduction

The present work is devoted to a thoroughly detailed study of nanocomposite magnets made of FePtNbB alloys. From the synthesis of the samples to the characterization by means of a wide range of experimental techniques, from the analysis of the formation and evolution of magnetic phases in the alloys to the determination and optimization of the magnetic properties, the present work is aimed to bring a significant contribution in the field of exchange spring magnets based on FePt. The manuscript is structured into 4 main Chapters.

Chapter 1 reports the state of the art of the research in this field, starting with the permanent and exchange spring magnets, discussing the importance of the FePt alloy as permanent magnet and detailing the advancements of FePt-based alloys in this field.

Chapter 2 presents the Synthesis and characterization of as cast FePtNbB ribbons. It is discussed first the FePt diagram and the choice of the chemical compositions of the investigated alloys. Then, among various synthesis methods available, that are briefly described, the melt spinning is chosen to be the method of synthesis. This choice is argued based on consideration linked to the desired stoichiometry and the possibility to obtain amorphous precursors. Then, structural characterization of the as-cast samples by a variety of experimental techniques is provided and thermal analysis is undertaken. The formation and evolution of magnetic phases is studied also by means of in-situ X-ray diffraction of synchrotron radiation.

Chapter 3 describes structural and Mössbauer characterization of annealed alloys. After detail the results of isothermal annealing, the obtained phase structure is quantified using Mössbauer data.

Chapter 4 presents the magnetic results obtained on the annealed alloys. The magnetic properties are investigated and magnetic parameters are obtained from hysteresis loops recorded at 5K and 300K. Energy products are derived and then correlated with the microstructure and phase composition in each sample. It is finally shown that the exchange spring criteria, reversibility, full exchange coupling between hard and soft phases, are fulfilled for these FePt-based alloys.

After the Conclusions drawn based on presented results, Perspectives for further research directions in the field are pointed out.

Chapter 1:

State of the art

The modern society is today strongly dependent on automation and miniaturization in many aspects. Magnetic materials are widely used in almost any important technical fields. Technological applications such as: electrical and mechanical power, transformers, electromotors, computer and IT industry, telecommunication, navigation, aviation and space operations, automation, micro-electro-mechanics, magnetocaloric refrigeration, materials testing and household applications, have created increasing demands for new and improved magnets [1]. With the advent of the new synthesis procedures that allow preparation of magnetic materials with nanometric structural characteristics, such as nanoparticles, thin films, multilayers, etc. the area of possible applications for nanometric-sized magnetic materials has considerably broadened. Nowadays, such nanoscopic magnetic materials are used in magnetic recording [2-4], as magnetic sensors, in magnetoelectronics [5-7] or in a wide range of biomedical applications [8,9].

From the point of view of their properties of interest for various applications, magnetic materials may be classified as soft magnets and hard magnets. Most of the important properties of any magnetic material are described by its magnetization, or hysteresis curve, which plots the magnetic flux, B , induced in the material (measured in units of gauss or tesla) against applied magnetic field, H (measured in units of oersted or A/m). The nature of this curve determines whether a material is considered as 'soft' or 'hard'.

An ideal soft magnetic material is one whose magnetic flux increases constantly with magnetic field and shows no hysteresis. Soft magnetic materials make good transformer cores because they can be easily magnetized, reproduce exactly the changes in applied magnetic field, and minimize losses due to hysteresis. However, they make poor permanent magnets because they do not remain magnetized once the applied field is removed.

In contrast, an ideal hard magnetic material is one whose magnetization curve is strongly nonlinear, and which follows a broad hysteresis loop. If gradually removing the

applied magnetic field, the magnetization has large non-zero values at zero applied field (remanent magnetization) and needs applying field with an opposite sign to bring the magnetization back to zero (coercive field). Hard magnetic materials are potentially good permanent magnets because they retain a large degree of magnetization, known as the remanent magnetization, and exhibit high magnetostatic energy required for applications.

A key characteristic by which permanent magnets are judged is their energy product $(BH)_{\max}$ - which provides a measure of the total magnetic energy that can be stored within them. In general, the higher the energy product, the more useful the material is for permanent magnet applications. During the 20th century, the experimentally achieved energy product maximum $(BH)_{\max}$ values have been increased exponentially from 2 kJ/m³ to more than 450 kJ/m³. The decisive breakthrough started in the 60's with the intermetallic rare-earth transition metal compounds, such as SmCo₅ (1960), Sm₂Fe₁₇N₃ (1970) and Nd₂Fe₁₄B (1983), nowadays commercially produced: they exhibit energy products exceeding 400 kJ/m³ [10-11]. Addition of rare-earth exchange coupled with Fe yields strong uniaxial anisotropy and increases coercivity but strongly diminishes the saturation magnetization. The search for other ternary phases with improved magnetization has given no practical results; interstitial modifications with N, C (as in Sm₂Fe₁₇C), Al, Ga or Si allowed only enhancement of Curie temperature and anisotropy but the global magnetic properties remains the same [12-15].

A promising new approach to elaborate high-performance permanent magnets has been proposed in 1991 by Kneller and Hawig [16] and in 1993 by Skomski and Coey [17]. This new pathway consists of making a composite material of two or more crystallographically coherent magnetic phases, one hard and other soft, suitably dispersed in the form of a refined grain microstructure. Such assembly of nanoscale magnetic phases, called "exchange-spring magnets", which are based on interfacial exchange coupled soft and hard ferromagnetic nanophases, combine the high magnetization of the soft phase with the high anisotropy of the hard phase to attain an extremely high energy product. In such a way, the maximum remanence-to-saturation ratio of 0.5, predicted by Stoner-Wohlfarth model may well be exceeded. Kneller and Hawig [16] have shown that for an exchange spring magnet the nanoscale soft phases must have sizes comparable to the exchange correlation length of the hard one (size estimated to \approx 10 nm for both soft and hard phases) and both phases must emerge from a common metastable precursor, in

order to be suitably exchange-coupled one to another [16]. Skomski and Coey predicted that a giant energy product of 1090 kJ/m^3 (137 MGOe) for $\text{Sm}_2\text{Fe}_{17}\text{N}_3/\text{Fe}_{65}\text{Co}_{35}$ phases might be attainable in suitable nanostructured exchange-spring magnets with an oriented hard phase [17]. In comparison, the theoretical limit of the energy product for Nd-Fe-B is 516 kJ/m^3 (64 MGOe).

So far, exchange-spring magnets have not delivered properties close to the predicted ones. As these materials are typically in the form of nanocomposites with randomly oriented hard grains dispersed within soft phase matrix, controlling the microstructure and the phase composition is a very challenging process.

In nanocomposite exchange spring magnets, a lot of efforts were directed at optimizing the microstructure and obtaining a fine and uniform distribution of exchange coupled soft and hard phases with small size of the soft phase [16,17]. The usual approach is to synthesize bulk nanocomposite magnets by melt-spinning [18-21], mechanical alloying [22] and sputtering [23]. However, the requirement that both the hard and soft phases emerge from a common metastable precursor and are controlled at the nanometer scale, to ensure efficient exchange coupling, has risen significant preparation challenges. Also, most of the times, the phases do not emerge from the same metastable precursor and are not crystallographically coherent. It has to be mentioned that, usually in Nd-Fe-B / α -Fe or Nd-Fe-B / Fe_3B exchange spring magnets, the phase composition obtained after annealing differs from the optimal one due to the formation of other ternary phases that are not hard magnetic, and therefore diminish drastically the magnetic properties. One of the most important obstacles is that the granular microstructure of the exchange spring magnets obtained by rapid solidification from the melt is not reproducible for a given composition and a given set of synthesis parameters and annealing conditions.

The research community is currently looking for an alternative, rare-earth free, kind of exchange spring magnet. There are several reasons for the search of an alternative. The rare-earth elements are expensive and contaminant for the environment. In both the cases of Sm-Co based and Nd-Fe-B based magnets, the microstructure of the annealed amorphous precursor presents usually rare-earth containing phases, other than the desired 2:14:1 or 2:17 hard magnetic ones, that are not magnetic [18,20]. In addition, sometimes in the initial chemical composition, other elements are included, such as Co

for increasing the anisotropy or Ga for enhancing the Curie temperature. That only makes the microstructure more complicated with a high degree of disorder and consequently decreases of the overall magnetization. Therefore, it has been thought that a much simpler approach towards the formation of exchange coupled hard-soft nanocomposites must be undertaken. One of the chosen systems is the binary alloy FePt.

Until recently, the reports on FePt system were extremely scarce [24, 25]. In 2000, Sun et al [2] reported the successful synthesis of FePt colloidal monodisperse nanoparticles, with an average diameter of 4 nm, self-assembled into regular arrays. After annealing at 560°C these regular arrays of FePt nanocrystals were shown to exhibit high perpendicular anisotropy and coercive field. Moreover, they have been proven to support stable magnetization reversal transition (bits written) at room temperature, which was a significant advancement towards new generation of magnetic recording media with extremely high data storage densities [2]. This discovery has boosted a very wide interest in the FePt system. In a revolutionary finding, Zeng et al [26] reported an exchange-coupled magnet made by self-assembling of Fe₃O₄ and FePt colloidal nanoparticles. By subsequent annealing, a regular arrangement of FePt and Fe₃Pt nanoparticles was obtained. Such an exchange-coupled magnet was reported to exhibit an energy product of 159 kJ/m³ (19.8 MGOe) [26].

The possibility of producing magnets based on FePt, not only as nanoparticles but also in a bulk-like shape, as ribbons, thin films, ball-milled powders or bulk alloys, shapes that make the FePt-based magnets much more convenient for technological applications has been exploited since 2004. The magnetic properties of FePt binary alloys were studied either as thin films, nanoparticles or mechanically alloyed powders. There are also reports on ternary alloys FePtB or FePtNb and also FePtMB systems, where M = Zr, Nb [36-41].

Rong et al. [27] have studied the mixed Fe₃O₄-FePt nanoparticles with mass ratio x of Fe₃O₄/FePt. By annealing, the magnetite is decomposed and provides an excess of Fe which gives rise to Fe₃Pt soft magnetic phase. A mixture of Fe₃Pt and FePt is obtained for $x > 1/20$. The highest energy product $(BH)_{\max}$ of about 135 kJ/m³ (16.8 MGOe) has been obtained for $x=1/5$.

Lyubina et al. [28] have investigated the nanocomposite Fe_{100-x}Pt_x ($x=40-60$) powders. With increasing Pt content, the coercivity increases from 0.41 up to 0.95 T,

whereas the remanence decreases from 1.04 down to 0.4 T. They have also reported [29] that a high coercivity of 0.7 T was achieved in Fe₅₀Pt₅₀ powder annealed at 450°C for 48h.

Rui et al. [30] have reported on Fe clusters dispersed into FePt matrix. After annealing at 600°C for 10 min, they have obtained an energy product of about 144 kJ/m³ (18MGOe). A second annealing procedure at 500°C improved the energy product that reached 168 kJ/m³ (21MGOe).

Christodoulides et al. [31] studied the FePt nanoparticles embedded in a carbon matrix formed by annealing FePt/C multilayers precursors. They have reported that the coercivity depends on the vol metric fraction of carbon and on annealing conditions. They have shown that the coercivity is increased as the particle size increases, nevertheless the highest coercivity of 2707 kA/m is obtained upon annealing at 600°C for 20 min. for samples with intermediate carbon content.

Simizu et al. [32] have exploited the exchange coupling between disordered cubic and ordered tetragonal FePt phases. In order to prove that the large values of coercivity obtained in the binary alloys are not due to magnetic texture induced during synthesis but result from the exchange spring coupling, they have prepared bulk samples of a cubic shape of Fe_{0.6}Pt_{0.4} and measured the magnetic properties along the three principal directions of the cube. The highest energy product has been obtained along z axis in the as-quenched sample $(BH)_{\max} = 47 \text{ kJ/m}^3$ (5.8 MGOe). The annealing at 600°C produced only slightly higher coercivity values while both the remanence and the energy product are reduced. Following this result, it seems that binary alloys do not easily allow a drastic improvement of magnetic properties by annealing. Since after casting, the samples are already crystallized into a mixture of ordered and disordered FePt phases, the microstructure does not allow further structural refinements that may lead to smaller grain sizes, better grain arrangements and consequently a better exchange coupling between hard and soft phases. It looks that small amounts of additional elements need to be included in the composition in order to better control the microstructural features that may ultimately lead to improved magnetic properties.

Until now, better magnetic properties in this system have been obtained in the case of thin films. Liu et al. [33] have synthesized by rf co-sputtering Fe/Pt multilayers

with a slight excess of Fe. A first heat treatment at 500°C for 5s was followed by a second one at 450°C for 15 min. The Fe and Pt layers have completely alloyed after annealing and no evidence of a multilayer structure has been found. The best magnetic properties were found in the Fe(2.1nm)/Pt(1.5nm)₁₆ sample. In that case, the energy product calculated in the perpendicular direction was as high as 419 kJ/m³ (52.8 MGOe) while in the parallel direction it was 318kJ/m³ (39.7 MGOe).

In order to improve the magnetic and structural properties, and to better control the phase composition, additional elements were considered to be added to the initial alloy composition. It is well established that metals such as Nb, Zr, and Mo act as grain growth inhibitors while metalloids such as B, Si, P can be added in order to improve the homogeneity of the initial alloy by amorphisation.

Inomata et al. [34] compared two alloys: first one, binary Fe_{0.65}Pt_{0.35} and second one the ternary (Fe_{0.65}Pt_{0.35})₈₃B₁₇. They have observed that the same annealing of the two as-cast alloys provided a three-fold increase in the coercive field, from 135.3 kA/m in binary alloy to 445.8 kA/m for the ternary one. This effect is mainly related to three factors which contribute to such a dramatic three-fold increase in the coercivity: a) by adding boron, excess of Fe will form borides, probably Fe₂B and there will be less than 65 at% Fe available for the formation of FePt phases, Pt relative content will increase and therefore is more probable to form the *L*₁₀ phase, than in the binary Fe_{0.65}Pt_{0.35} alloy: b) a much more refined grain microstructure that will be obtained after annealing an amorphous precursor, since addition of boron ensures amorphization in the as-cast state and c) the co-existence of hard magnetic tetragonal FePt exchange-coupled to disordered cubic FePt and also Fe₂B soft magnetic phases.

Zhang et al. [35] have studied the influence of surface velocity of the wheel on the magnetic properties and on the formation of nanocomposite structure in Fe₅₂Pt₃₀B₁₈. They have shown that between 20-37 m/s wheel velocity, the alloy is directly cast with a nanocrystalline structure where hard magnetic FePt and soft magnetic Fe₂B coexists. When the wheel velocity was between 40-50 m/s, the alloy was partially amorphous with small crystals of soft magnetic cubic FePt already formed. Nevertheless, the best hard magnetic properties were obtained for the alloy produced at V_S= 50 m/s wheel velocity and annealed at 773K for 900s. In this case, (BH)_{max}= 108 kJ/m³, B_r= 0.77T and H_c=718

kA/m. Same authors [36,37] obtained directly in the as-spun state of the ribbons good hard magnetic properties. In $\text{Fe}_{52}\text{Pt}_{30}\text{B}_{18}$ alloy, the results were: $B_r=0.7\text{T}$, $H_c=783\text{kA/m}$, and $(\text{BH})_{\text{max}}=88 \text{ kJ/m}^3$. Nevertheless, the magnetic properties were substantially improved after annealing, for alloys with significantly lower Pt content. For $\text{Fe}_{56.25}\text{Pt}_{18.75}\text{B}_{25}$ ribbons annealed at 785K for 900s, the best combination of magnetic properties was: $B_r=0.96\text{T}$, $(M_r/M_s)=0.83$, $H_c=340\text{kA/m}$ and $(\text{BH})_{\text{max}}=102.2 \text{ kJ/m}^3$. Inoue et al. [38] have studied the effect of the substitution of Fe with Co, in the initial composition of a FePtB alloy. It is widely known that Co addition induces supplementary uniaxial magnetocrystalline anisotropy, therefore the authors have attempted to increase the coercivity by adding Co. In the case of $\text{Fe}_{56.25-x}\text{Co}_x\text{Pt}_{18.75}\text{B}_{25}$ ($x=0-20$) alloys annealed at 785K for 900s, the obtained values were:

- for 0 at % Co, $B_r=0.96\text{T}$, $M_r/M_s=0.83$, $H_c=340\text{kA/m}$ and $(\text{BH})_{\text{max}}=102.2\text{kJ/m}^3$
- for 20 at % Co, $B_r=0.68\text{T}$, $M_r/M_s=0.80$, $H_c=426\text{kA/m}$ and $(\text{BH})_{\text{max}}=66.7\text{kJ/m}^3$

It can be seen that, while the coercivity has indeed increased, on the contrary, the effect of 20 at% Co addition was to decrease both the energy product and the remanence.

Zhang et al. [39] have studied the influence of B addition on the magnetic properties resulted after annealing. They investigated the melt spun $\text{Fe}_{80-x}\text{Pt}_x\text{B}_{20}$ ($x = 20,22,24$) alloys. The ribbons were annealed at 798K for 900s and obtained: $B_r= 0.93-1.05 \text{ T}$, $M_r/M_s=0.79-0.82$, $H_c=375-487\text{kA/m}$ and $(\text{BH})_{\text{max}}=118-127\text{kJ/m}^3$. A steady increase of the magnetic properties is thus obtained upon increasing the initial B content. In addition to the behavior described above for results of Inomata et al [34] results, this trend for the magnetic properties is mostly the effect of a better homogeneity of the alloy in the as-cast state, due to the glass forming ability of the B. After annealing, the microstructure is more refined with smaller grain sizes if the initial state of the alloy is amorphous with a large degree of homogeneity.

Transition refractory metals have also been considered as potential addition in the FePt systems, in order to improve the microstructure obtained after annealing and hence the magnetic properties. Bruck et. al. [40] investigated Fe-Pt alloys with small amounts of refractory metals. They have studied the effect of the atomic disorder–order transformation on remanence enhancement and coercivity by isothermal annealing at temperatures well below the transformation point. They have shown that the disorder–order transformation occurs gradually during annealing. The addition of small amounts of

refractory metals to the initial composition is useful for limiting the growth of crystallites during annealing. At the optimum annealing conditions, they have obtained the following magnetic properties:

- Fe-Pt-Nb_{0.5}, Br=0.98 T and $(BH)_{\max}=125\text{kJ/m}^3$ (15.6 MGOe)
- Fe-Pt-Zr_{0.5}, Br=0.95 T and $(BH)_{\max}=88\text{kJ/m}^3$ (11 MGOe)
- Fe-Pt-Ti_{0.5}, Br=0.93 T and $(BH)_{\max}=102\text{kJ/m}^3$ (12.7 MGOe)

As it can be seen, the best magnetic properties are obtained if the transitional refractory metal is Nb. It has to be mentioned that, usually, upon annealing nanocrystalline alloys, Nb atoms are located in the grain boundaries and/or interfacial regions. Therefore, a larger amount of Nb (up to 2 at%) would be more effective for the grain structure since it will help to create larger amount of interfacial regions and hence a better arrangement of the small hard and soft nanograins. In addition, Nb was the refractory metal chosen for the Finemet [41] alloy as being the most effective in obtaining a microstructure of refined grains that ensures optimal soft magnetic properties.

Recently, there have been reports on the preparation and characterization of quaternary alloys Fe-Pt-M-B. Makino et al [42-45] studied the $(\text{Fe}_{0.55}\text{Pt}_{0.45})\text{-M-B}$ alloy formed by rapid quenching, where M=Zr, Nb and Ti. In [42] they show that the as-cast $(\text{Fe}_{0.55}\text{Pt}_{0.45})_{78}\text{Zr}_4\text{B}_{18}$ alloy exhibits the highest coercivity $H_c=649\text{kA/m}$. After annealing at 623K for 18ks, H_c reached 1000kA/m. The compositional range for the formation of $\text{L}_{10}\text{-FePt}$ phase, in the case of $(\text{Fe}_{0.55}\text{Pt}_{0.45})\text{-Nb-B}$ alloys, is considerably larger than that of $(\text{Fe}_{0.55}\text{Pt}_{0.45})\text{-Zr-B}$ alloys, i.e. for the ranges 2-8 at% of Nb and 15-24 at% of B, H_c is higher than 300kA/m. For $(\text{Fe}_{0.55}\text{Pt}_{0.45})\text{-Ti-B}$ alloys, H_c higher than 200kA/m is obtained in the range of 2-6 at% of Ti and 3-20 at% of B. In [43] a coercivity of $H_c=684\text{kA/m}$ was obtained for $(\text{Fe}_{0.50}\text{Pt}_{0.40})_{78}\text{Zr}_4\text{B}_{18}$ in as-quenched state. H_c decreases with the increase of Zr and B content. In [44] they have obtained $H_c=588\text{kA/m}$ for $(\text{Fe}_{0.55}\text{Pt}_{0.45})_{72}\text{Nb}_8\text{B}_{18}$ and 357kA/m for $(\text{Fe}_{0.55}\text{Pt}_{0.45})_{83}\text{Ti}_2\text{B}_{15}$. In [45] for the ternary $(\text{Fe}_{0.55}\text{Pt}_{0.45})_{85}\text{B}_{15}$ alloy after annealing at 923K for 18ks they have reported a coercivity value of $H_c=357\text{kA/m}$.

Bitoh et al. [46] have studied the quaternary Fe-Pt-Zr-B alloy with equiatomic Fe/Pt ratio. For the $(\text{Fe}_{0.50}\text{Pt}_{0.50})_{78}\text{Zr}_4\text{B}_{18}$ alloy they obtained the best magnetic properties, i.e. a coercivity value of $H_c=688\text{ kA/m}$. Nevertheless, no structural characterization was made in that report, in order to explain the origin of the increased coercivity, and no exchange spring mechanisms between the constituent phases have been proved.

The idea behind this thesis, an idea that we launched and developed in 2004, was to cast an alloy, based on FePt, and to be able to obtain such a microstructure where the highly ordered f.c.t. FePt should be immersed into a soft magnetic matrix that crystallizes from the same metastable precursor as the hard phase. Such an alloy, with appropriate grain sizes refined down to the exchange correlation length, would have hard magnetic grains exchange-coupled through the soft matrix. It shall provide high values of magnetic parameters of interest, such as high coercivity, high magnetocrystalline anisotropy and enhanced energy product. If succeeded, these alloys would constitute without doubt one of the future classes of nanocomposite exchange spring magnets with high performance as permanent magnetic materials.

The state of the art shows that to improve and control the magnetic properties of these exchange- spring magnetic intermetallic alloys, we must be able to control their microstructure at the nanometric scale, i.e. size, distribution and volume/mass fraction of grains, and their alternate arrangement within the microstructure which will ensure an effective exchange coupling between them, that ultimately leads to optimized energy products for these magnets.

The theoretical works that predict these magnetic properties emphasize the importance of volumic/mass fractions of the two phases hard/soft and therefore the need for fine and quantitative microstructural analysis of these systems. Until now, very few quantitative studies are reported in the literature, but we are convinced that deep, complete and detailed knowledge of the microstructure is essential to understand the relationship between the microstructure and the magnetic properties investigated and hoped for.

In this work, we adopt the method of partial devitrification of a precursor obtained by melt spinning to form nanocrystalline alloys consisting of hard magnetic grains Fe-Pt ($L1_0$) dispersed in a magnetic soft matrix based on (Fe(PtNb)-B) alloy. Going much further than the above-described state-of-the-art in this field, the microstructural analysis is carried out with a combination of X-rays and electron diffractions, Transmission Electron Microscopy and local probe technique as ^{57}Fe Mössbauer Spectrometry. As each possible phase contains iron, this latter technique allows us to accurately determine the nature of each phase by identifying the hyperfine parameters and to weigh the fraction of each phase. Formation and evolution with temperature of the phases that emerge from the

FePtNbB precursor during annealing we monitored using differential scanning calorimetry and X-ray diffraction of synchrotron radiation, which is a unique tool, never used before for this kind of materials. The microstructure will be correlated with the magnetic properties, that are obtained, analyzed and described in detail using vibrating sample and SQUID magnetometry. Energy products, comparable to the values reported so far, are obtained as it will be later shown and the exchange spring behavior in the alloys will be proven. In this way, the present work hopefully will bring a definite advancement in the field of FePt-based intermetallic alloys and will produce a breakthrough in the search for a future class of exchange spring nanocomposite magnets.

Chapter 2: Synthesis and characterization of as-cast Fe-Pt-Nb-B ribbons.

2.1. The Fe-Pt-Nb-B alloys

2.1.1. FePt binary phase diagram

The choice of the chemical compositions of the investigated alloys results from the analysis of the phase diagram of the binary FePt alloy which is illustrated in Figure 2.1 [46].

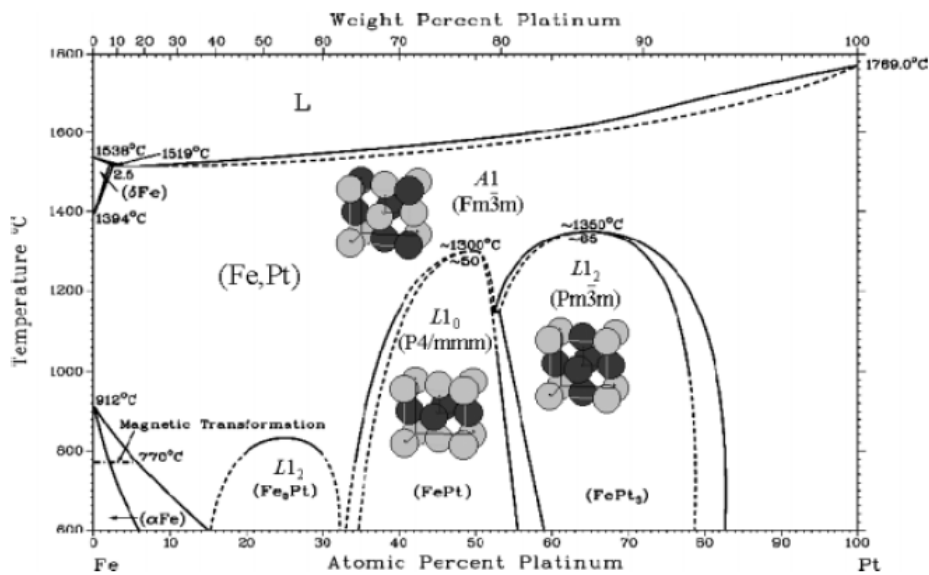


Figure 2.1: The phase diagram Fe-Pt binary alloy, taken from [46].

At high temperature, the binary Fe-Pt phase diagram shows solid solubility on the whole compositional range. The crystal structure on the entire range of compositions is a disordered face-centered-cubic (fcc) symmetry, where Fe and Pt atoms are randomly distributed. This structure is named *A1* (or γ_0) and belongs to the *Fm $\bar{3}$ m* space group. The disordered fcc *A1* phase is stable for temperatures ranged from 1350°C up to 1500°C.

A structural transformation occurs at lower temperature. For temperatures below 1350°C, the fcc phase undergoes a disorder – order transformation. This gives rise to 3 stable structural symmetries, depending upon the composition of Fe_{1-x}Pt_x alloys. For low and high Pt concentrations ($0.15 < x < 0.32$ and $0.5 < x < 0.8$), ordered cubic structures identified as the Fe₃Pt and FePt₃ are formed. These phases have Cu₃Au and CuAu₃- type

structures respectively, with face-centered-cubic symmetries, known as $L1_2$ and belonging to the $Pm\bar{3}m$ space group.

In the vicinity of the equiatomic composition ($0.35 < x < 0.57$), the disorder-order phase transformation gives rise to the ordered FePt phase. This phase, denoted as γ_1 phase, is of a CuAuI-type structure, with lattice parameters $a = 3.838 \text{ \AA}$ and $c = 3.715 \text{ \AA}$. Since CuAuI structure has a primitive tetragonal Bravais lattice (P), γ_1 phase that emerges from the disordered fcc $A1$ phase, has a face-centered-tetragonal (fct) phase structure and belongs to the $P4/mmm$ space group. In metallurgical nomenclature, it is known as the $L1_0$ phase. Hereafter, we will refer to these phases by their metallurgical nomenclature.

The unit cell of the $L1_0$ phase consists of planes of atoms with either only Fe or only Pt atoms (see inset of Figure 2.1). During ordering, the Fe and Pt atoms, that were initially randomly disposed within the crystallographic sites of the fcc unit cell, will move into planes, inducing thus a slight constriction in the c-axis direction. Ordering occurs along the directions of planes and the tetragonal ordered regions are formed in such a way that the c-axis becomes parallel to one of the $\langle 100 \rangle$ axes of the fcc phase. This originates the high uniaxial magnetocrystalline anisotropy of the ordered $L1_0$ phase. The lattice of the $L1_0$ phase is often described in the literature as a superlattice. There are basically two definitions of the term “superlattice” [47]:

- (1) a crystal structure that repeats over a relatively long distance, as in multilayer structures.
- (2) a structure, derived from a parent structure, in which some atoms are slightly deviated from their positions, such that the symmetry is lowered.

In our case, hereafter, we will use the term “superlattice” for the $L1_0$ phase as explained by the second definition.

It is worth noticing that in the FePt phase diagram there is a compositional interval centered around 35 at.% of Pt where both $L1_2$ and $L1_0$ phases are possibly stable at low temperatures. It has to be mentioned that at room temperature $FePt_3$ is paramagnetic while Fe_3Pt is ferromagnetic with large spontaneous magnetization. $L1_0$ FePt is ferromagnetic with a large magnetic anisotropy, as discussed in previous chapter.

If an alloy with Pt content close to 35 at.% is rapidly solidified by quenching down to ambient temperature, as in the melt-spinning technique, it might be possible to

obtain a two-phase material where $L1_0$ and $A1$ or $L1_2$ phases co-exist. Such coexistence of these two phases is of interest for the purpose of the present work.

2.1.2. Choice of chemical compositions

The chemical compositions of the initial alloys were carefully chosen in order to produce first a structurally disordered precursor and then a primary crystallization producing hard magnetic phase, $L1_0$ FePt, dispersed into residual soft magnetic phase, $A1$ and/or $L1_2$.

Several studies on the development of such microstructures have been already reported in literature. Inoue et al [38] obtained co-existence of $A1$ and $L1_0$ phases together with borides, in a Fe(Co)PtB alloy with Fe(Co):Pt ratio of 3:1, after annealing at 785K. Simizu et al. [32] have prepared bulk FePt alloy with Fe:Pt ratio of 3:2 and showed that both $A1$ and $L1_0$ phases crystallize together, directly from the melt and further annealing decrease the energy product. In the binary alloy, it is expected [32] that the hard phase may be formed in a wide range of stoichiometry, between 40 and 60 at.% Fe. But in the case of FePt nanoparticles [2, 4] it is shown that ideal stoichiometry for obtaining the hard phase is $Fe_{55-x}Pt_{45+x}$ where $x = 0 - 4$. In our samples, for calculation of the compositions we have chosen an initial relative stoichiometry of the FePt hard phase as being $Fe_{55}Pt_{45}$. Of course, the real stoichiometry in the obtained $L1_0$ phase would be quite different due to various factors, including: atomic segregation, multiple phase formation, and so on.

The chemical compositions have been chosen in order to fulfil some specific criteria, such as:

- a) Fe:Pt relative proportion in the range where $L1_0$ phase may be formed according to the phase diagram, as illustrated in Figure 2.1.
- b) low Pt content (more cost effective);
- c) a certain hard phase – soft phase relative abundance ratio that would lead upon annealing to a microstructure with small exchange coupled grains;
- d) a Boron content that would allow the formation of disordered as-cast state;
- e) addition of Niobium that has the role of limiting the grain growth during annealing treatments, in analogy with the well-known Finemet soft magnetic nanocrystalline alloy [48];

If we want to make an exchange-coupled magnet with good performance, such as energy product (about 70 kJ/m^3) and coercivity (about 800 kA/m), then the relative abundance ratio between hard and soft phases must have certain values. For example, in the earlier works on exchange spring magnets by Kneller and Hawig [16] and by Skomski and Coey [17], the hard phase relative abundance was between 30 and 40 atomic mass%. Nevertheless, Coehoorn et al. [18] have found good properties – $(BH)_{\text{max}} = 95 \text{ kJ/m}^3$ – for only 15% of hard phase. By calculation, this leads to an initial composition of the alloy with Fe excess and low Pt content. Actual compositions are depicted in Table I.

It has been documented in 20 years of extensive research that in the Fe-Cu-Nb-Si-B nanocrystalline alloy, a microstructure of Fe(Si) nanograins embedded in an amorphous-like matrix is responsible for the excellent soft magnetic properties [49-53]. This is due to the small size of the nanograins (typically 15-25 nm) and the anisotropy is averaged out giving thus the extremely soft character of the material. In this alloy it has been demonstrated that Cu atoms act as nucleation centers for the Fe(Si) grains facilitating thus the nucleation at early stages of annealing, boron is the glass-forming element that ensures the synthesis of a truly amorphous precursor in the as-cast state and Nb is added in order to limit the growth of the grains. Indeed, it has been proved that atoms of refractory elements such as Nb or Zr migrate during annealing via diffusion processes and are localized in the grain boundaries or in the interfacial regions [51-53]. They limit further growth of Fe(Si) grains by impeding the diffusion of other metal (Fe) or metalloid (Si) elements into the already formed grains.

By analogy to this system, we had added to the composition B and Nb atoms in order to facilitate the formation of a refined microstructure with small nanograins with enhanced exchange coupling between them. A coarsened microstructure with larger nanograins does lower the magnetization and therefore the energy product in the hard-soft magnetic alloy will be diminished.

Two different approaches to calculate of the initial composition were undertaken. The first approach concerns the calculation based on the necessity to have, in the annealed (nanocrystalline) state, a certain amount of hard $L1_0$ phase and a certain amount

of two other soft magnetic phases, in our case, Fe_3Pt and Fe_2B . Due to the presence of boron, upon annealing it is to be expected that more than one soft magnetic phase will be formed. Following this approach, we have calculated the compositions for the first batch, made of three different alloys.

First alloy was conceived to have, after appropriate annealing, a phase composition where 30% atomic mass amount of $L1_0$ hard phase with the $\text{Fe}_{55}\text{Pt}_{45}$ stoichiometry will coexist with 70% amount of soft phases. From this amount, 35% would be of the $L1_2$ Fe_3Pt and 35% of the boride Fe_2B phases. Such an alloy must have the initial composition (in atomic percentages) $\text{Fe}_{68}\text{Pt}_{21}\text{Nb}_2\text{B}_9$. If the 70% of soft phase consist of only Fe_2B then the initial composition will be $\text{Fe}_{68}\text{Pt}_{13}\text{Nb}_2\text{B}_{17}$. The third alloy from the first batch had to correspond to 40% FePt $L1_0$ hard phase and 60% soft phases from which 30% Fe_3Pt and 30% Fe_2B . This has led to an alloy composition of $\text{Fe}_{65}\text{Pt}_{25}\text{Nb}_2\text{B}_8$.

Thus, following this approach, we calculated the first three different compositions of the primary alloy as $\text{Fe}_{68}\text{Pt}_{21}\text{Nb}_2\text{B}_9$ (denoted *1a*), $\text{Fe}_{68}\text{Pt}_{13}\text{Nb}_2\text{B}_{17}$ (denoted *1b*) and $\text{Fe}_{65}\text{Pt}_{25}\text{Nb}_2\text{B}_8$ (denoted *2a*). This set of samples will be denoted hereafter Fe-rich batch.

The second approach was based on the Fe:Pt phase diagram. In the diagram (see Figure 2.1), there is a compositional region around x (Pt content) = 35 at% where $A1$ disordered phase borders both $L1_2$ Fe_3Pt and $L1_0$ FePt phases. Therefore by rapid solidification from the melt of an alloy of such relative proportion would eventually allow the formation of all 3 phases, one hard, the other two soft magnetic phases. Based on this approach we have synthesized two different alloys with only slight difference of 2 at % boron in the initial composition. The first one was prepared as to correspond to the formula $(\text{Fe}_{0.65}\text{Pt}_{0.35})_{80}\text{Nb}_2\text{B}_{18}$ while the other one was $(\text{Fe}_{0.65}\text{Pt}_{0.35})_{78}\text{Nb}_2\text{B}_{20}$. The calculated composition for these two alloys is $\text{Fe}_{52}\text{Pt}_{28}\text{Nb}_2\text{B}_{18}$ (denoted FePt – 1) and $\text{Fe}_{51}\text{Pt}_{27}\text{Nb}_2\text{B}_{20}$ (denoted FePt – 2). This set of samples will be denoted hereafter Pt-rich batch. The compositions of all the alloys synthesized are listed in Table I.

Table I: The initial composition of the as-cast alloys and their denomination

No.	Chemical composition (in at.%)	Sample denomination
1	Fe ₆₈ Pt ₂₁ Nb ₂ B ₉	1a
2	Fe ₆₈ Pt ₁₃ Nb ₂ B ₁₇	1b
3	Fe ₆₅ Pt ₂₅ Nb ₂ B ₈	2a
4	Fe ₅₂ Pt ₂₈ Nb ₂ B ₁₈	FePt -1
5	Fe ₅₁ Pt ₂₇ Nb ₂ B ₂₀	FePt -2

2.2. Synthesis of the Fe-Pt-Nb-B ribbons

2.2.1. Choice of the synthesis method

Available synthesis methods

A variety of methods of synthesis are suitable for synthesis of metallic alloys. Besides the melt spinning technique, or rapid solidification from the melt, we mention and briefly describe mechanical alloying and thin film deposition.

A) Mechanical alloying or mechano-synthesis is the process of alloying powder metals by grinding them against hard metal spheres in ball mills. During the mechanical alloying process, the powder particles are periodically trapped between colliding balls and are plastically deformed. The ball collisions cause fracturing and cold welding of the grains, forming interfaces at the atomic scale. Further milling lead to an increase of the volumetric fraction of interfaces, alloying the metal components and the grain sizes decrease down to nanometric scale (usually tens of nm).

B) Thin-film deposition is the name generically given to any technique for depositing a thin film of material onto a substrate or onto previously deposited layers. Using the deposition techniques, one can prepare either thin crystalline or amorphous films the thickness of which can be controlled within a few hundreds of nanometers, or multilayers composed of nanometer thick crystalline monolayers using molecular beam epitaxy. One can distinguish two main categories in function of the nature of the precursor: chemical and physical deposition.

C) Chemical deposition techniques use fluid precursors that undergo chemical changes at a solid surface thus leaving a solid layer onto this surface. Depending on the nature of the precursor, the chemical deposition is divided into chemical solution deposition (CSD) where the precursor is a solution of metal salts, and chemical vapor deposition (CVD) where the precursor is a gas-phase metal halide or hydride, or organometallic gas in the case of molecular chemical vapor deposition (MOCVD). Plasma enhanced CVD uses an ionized vapor, or plasma, as a precursor. PECVD relies on electromagnetic means (electric current, microwave excitation), rather than a chemical reaction.

D) Physical deposition is based upon mechanical or thermodynamic concept to produce a thin film of solid. The material to be deposited is placed in an entropic environment, so that particles of material escape its surface by evaporation, sputtering or ablation. Facing this source is a cooler surface which absorbs energy from these particles as they arrive, allowing them to form a solid layer. The whole system is kept in a vacuum deposition chamber allowing the particles to travel as freely as possible. Most common techniques that rely on physical deposition include: thermal evaporation, electron beam evaporation, magnetron and radio-frequency sputtering, pulsed laser deposition, cathodic arc deposition, reactive sputtering and molecular beam epitaxy.

The melt spinning technique

In this work, a melt-spinning technique based on rapid solidification process (typically the cooling rates achievable are about 10^6 K/min) is used to elaborate the precursor as an amorphous metallic ribbons. Indeed, the extremely fast cooling of the molten metal allows quenching the alloy into an amorphous-like state. Even if the obtained alloy is not fully amorphous, by using this method it is possible to produce metastable phases at room temperature which could be transformed under annealing.

It is important to obtain an amorphous-like precursor in the as-cast state. From an amorphous-like precursor, we can control both the formation of the necessary hard and soft magnetic phases and the topology of the microstructure. An alternance of suitably disposed hard and soft regions or hard nanocrystalline grains dispersed within a soft magnetic matrix may be obtained and the sizes of the magnetic entities conveniently

controlled by a subsequent annealing treatment of the amorphous precursor. For this purpose one has to optimize heating rate, temperature and time of annealing.

From this point of view, the rapid solidification of the melt is the most suitable technique that would ensure the amorphization of the melted alloy in the as-cast state. As the melt is expelled through the nozzle onto the rotating wheel, the degree of amorphization, for a given composition and a given amount of glass forming element (boron), can be controlled by the speed of the wheel. It has been shown that at lower velocities of the wheel, the alloy may be obtained in nanocrystalline state but higher wheel velocity favors an amorphous state. Therefore, by using the melt-spinning technique, we dispose of a supplemental experimental parameter (wheel velocity) through which we can control and ensure the amorphization of the alloy.

In addition to these arguments, compared to other available synthesis technique, some other reasons drove us to this choice:

1. It is a much cheaper experimental technique compared to the thin film deposition method
2. It allows a better control of the stoichiometry of the final product compared with both mechanical alloying and thin film deposition. In the case of mechanical alloying, due to the material losses onto the balls and the walls of vials, the stoichiometry of the final product may be different from the initial composition. In the case of thin film deposition, the difference in the evaporation / sputtering rate of each constituent metal, it is difficult to produce alloys at a strictly controlled stoichiometry. While suitable for a binary alloy, in our case, where we have to mix 3 metals and 1 metalloid, the differences in the evaporation rate are large and exact stoichiometry of 4 different elements with different evaporation rates will be hard to control. Upon our knowledge, there are no reports in the literature, of FePtNbB synthesized as thin films. On the contrary, in the melt spinning technique, as the whole amount of metal precursor is melted and the whole melt is purged onto the wheel and forms ribbons, there are almost no material losses during synthesis.
3. It does not require metal precursors, unlike the thin film deposition, precursors that bring chemical impurities into the final composition of the alloy.
4. It does not require ultra high vacuum chambers for the synthesis.

5. Unlike the mechanical alloying, where the large number of interfaces and highly reactive surface of the nanograins usually make the alloy extremely sensitive to oxidation and aging processes after synthesis, in the melt spun ribbons there is practically no oxidation after casting them onto the copper wheel. The only possibility of oxidation might occur during the annealing treatments, but can be avoided using controlled atmosphere and / or low vacuum annealing facilities. We have also observed no aging effects at all, since we have repeated on some samples structural and magnetic measurements after 12 months and the results were identical.
6. It allows the synthesis of more homogeneous and much larger quantities of alloy than in the other cases. It is well established that this technique is highly suitable for technological and industrial applications.
7. As explained earlier, it allows solidification and stabilization at room temperature of certain phases of interest from the phase diagram that are reportedly stable only in the molten state.
8. As mentioned above, it allows amorphization of the alloy by tuning the velocity of the wheel. The amorphous precursor is then submitted to partial devitrification (annealing) treatments that are meant to ensure the formation of a certain phase structure in the sample, with controlled number of nucleation sites and controlled size of the nanocrystals formed during annealing. This would ultimately lead to a microstructure where hard magnetic grains are embedded in soft magnetic matrix and exchange coupled to each other through soft magnetic regions.

For these reasons we choose to synthesize FePtNbB alloys by rapid solidification from the melt or melt spinning technique; indeed this procedure has been successfully used for the last 40 years to prepare amorphous, metastable and nanocrystalline intermetallic alloys starting from their molten state.

2.2.2. The principle of method of the rapid solidification from the melt

As a principle, in melt spinning, a jet of molten metal is propelled against the moving surface of a cold, rotating copper wheel. The wheel is cooled internally, usually by water or liquid nitrogen, and rotated at a high velocity, usually between 1500 and 4000

rot/min. The thin stream of liquid metal is then dripped onto the wheel and cooled, thus causing rapid solidification or quenching. As a result, a solid and homogeneous film of metallic alloy is spun off as a continuous ribbon at a speed that can exceed 1 km/min. This technique has been used to develop materials that require extremely high cooling rates in order to form metallic glasses and alloys of immiscible metals. The cooling rates achievable by melt-spinning are on the order of 10^4 – 10^7 K/s.

A schematic view of the melt-spinning process is shown in Figure 2.2. On top of the copper wheel there is a quartz tube with a nozzle at the bottom. The constituent metals are melted in small ingots in an induction furnace and then inserted in the quartz tube. They are then melted again in the quartz tube by a radio frequency heating coil and the obtained melt is purged onto the wheel by an overpressure of Ar.

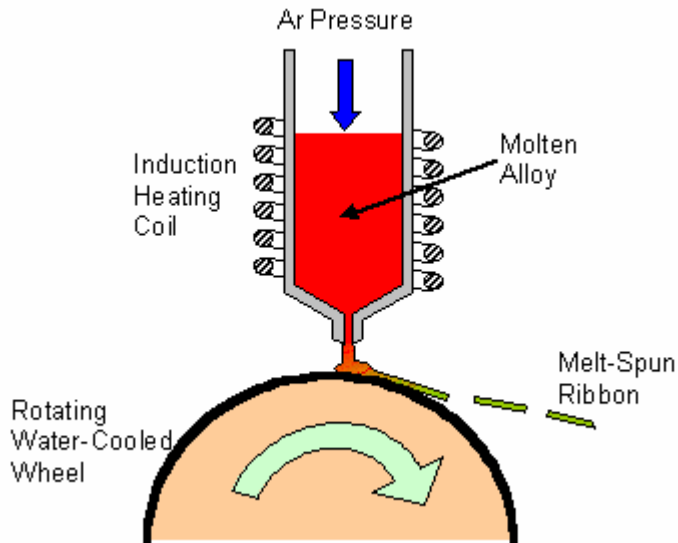


Figure 2.2: Schematic diagram of the melt spinning process (taken from ww.magnets.bham.ac.uk)



Figure 2.3: Image of the wheel chamber of the melt spinner



Figure 2.4: Image of the as-obtained melt spun ribbons

2.2.3. Experimental procedure of synthesis

The ribbons were synthesized starting with elemental powders and flakes of high purity. They were melted together in an induction furnace with controlled melting temperature. The primary alloy was 3 times re-melted to prevent element segregation and to improve its chemical homogeneity. A total amount of 5 g has been used for each

sample. The rapid solidification of the melt is performed on a Buhler Melt Spinner SC with protective Ar atmosphere at the National Institute for Materials Physics, Bucharest.

The obtained melt was then purged onto the surface of a Cu wheel (Figure 2.3). The wheel has 40 cm in diameter and rotates during the synthesis with 2000 rot/min. The melt is flown away from the quartz tube through a circular nozzle of 0.5 mm using Ar pressure of 40 kPa. The size of the nozzle dictates the width of the obtained ribbons. Since the total mass of the experiment was only 5 g, it was necessary to use such a small nozzle. The melt solidifies with a cooling rate of about 10^6 K/min. Away from the wheel, continuous and homogeneous ribbons are obtained. They are about 30 microns thick, 2-3 mm wide and several decimeters long. As an illustrative example, the image of ribbons obtained on our melt-spinner is presented in Figure 2.4.

2.3. Structural characterization of as-cast ribbons

2.3.1. Experimental techniques for characterization

The as-cast state of the ribbons, as a precursor for the desired microstructure formed of exchange coupled hard and soft magnetic nanograins, is of crucial importance since it determines unequivocally the phase structure of the alloy after appropriate annealing. Therefore, the complete characterization of the as-cast ribbons as well as the determination of real composition and optimal annealing parameters, related to the formation of the desired phase structure with nanometric sized hard and soft regions, has to be performed. Moreover, these results have to be correlated with the observed magnetic behavior. The experimental techniques used for the characterization of the as-cast and annealed samples are: I) Energy Dispersive X-ray spectroscopy (EDX), II) X-ray diffraction (XRD), III) Transmission electron microscopy (TEM), IV) Mössbauer spectrometry (MS), V) Vibrating sample magnetometry (VSM) and VI) SQUID magnetometry.

I) Energy Dispersive Spectroscopy (EDX)

Energy dispersive X-ray spectroscopy (EDS, EDX or EDXRF) is an analytical technique used for the elemental analysis or chemical characterization of a sample. EDX relies on the investigation of a sample through interactions between electromagnetic radiation and matter, analyzing X-rays emitted by the matter in response to the interaction with charged particles. Its characterization capabilities are due to the fact that each element has a unique atomic structure allowing X-rays that are characteristic of an element's atomic structure to be identified uniquely from other elements. To stimulate the emission of characteristic X-rays from a specimen, a high-energy beam of charged particles such as electrons or protons, or a beam of X-rays, hits the sample. This incident beam may excite an electron in an inner shell, ejecting it from the shell while creating an electron hole where the electron was. An electron from an outer, higher-energy shell then fills the hole, and the difference in energy between the higher-energy shell and the lower energy shell may be released in the form of an X-ray. The number and energy of the X-ray quanta emitted from a specimen can be measured by an energy dispersive spectrometer. As the energy of the X-rays is characteristic of the difference in energy between the two shells, and of the atomic structure of the element from which they were emitted, this allows the elemental composition of the specimen to be estimated.

II) X-ray diffraction (XRD)

X-ray diffraction is a method of determining the arrangement of atoms within a crystal, in which a beam of X-rays strikes a crystal and scatters into many different directions. Both the positions and the intensities of peaks obtained from the diffracted radiation (Bragg peaks) allow the mean lattice parameters of the unit cell and the distance between atomic planes to be estimated. The diffraction pattern represents basically the intensity of the radiation scattered by a sample over a wide range of angular positions. If at a certain angle, the X-rays are scattered by a family of parallel atomic planes, then a Bragg peak will be found in the X-ray diffractogram, peak obtained from the interference of the scattered radiation from these parallel atomic planes. The angle of scattering of the X-ray beam by the specimen is related to the atomic interplanar distance d by the Bragg law:

$$n\lambda = 2d \cdot \sin \theta$$

where λ is the wavelength of the X-ray beam, d is the interatomic distance or the spacing between the atomic planes in a family of planes, θ is the angle between the incident beam and the scattering atomic planes and n is an integer determined by the order of the interference of the scattered rays.

In polycrystalline materials the atomic planes are randomly oriented and the diffractograms are plotted as the diffracted intensity in function of the scattering angle 2θ . A typical diffractogram of a polycrystalline sample show occurrence of sharp Bragg peaks. Each Bragg peak unambiguously determines the reflection from a certain family of atomic planes in the crystal via the Bragg law. From the identification of all the d spacings, one can obtain thorough information about the nature and symmetry of the crystalline phases occurring in the sample. X-ray diffraction is a powerful and widely used technique that allows characterization of solid materials, to determine the crystalline phases occurring in the sample, their symmetry and their relative abundance in the sample. Besides that, due to their shape, ribbons are well adapted for X-ray experiments.

III) Transmission electron microscopy (TEM)

The transmission electron microscopy is an imaging technique that is based on the interaction between a thin sample and an accelerated electron beam. As the associated wavelength of the electrons is small enough and the acceleration voltages currently reach between 100 and 1000 kV, a collimated electron beam can resolve the topography of the surface of a thin sample with a resolution of the order of 1 nm. Together with the X-ray diffraction represents a powerful tool for structural investigation of materials. The electron path is condensed, projected and collimated in a similar way with the optic light in a usual microscope but using magnetic lenses instead of optical lenses. The working mode of an electron microscope can be in bright field contrast (BFI) and dark field contrast (DFI). In BFI, only the non-diffracted electron beam is used for constructing the image while in DFI only the beam diffracted by the sample is used for obtaining the image. Complementary information about the investigated area is brought by the electron

diffraction pattern (EDP) that gives structural information in analogy with the XRD measurements but on the local area imaged by the beam.

IV) Mössbauer spectroscopy (MS)

The Mössbauer effect lies on the nuclear gamma resonance phenomenon. If a radioactive nucleus (named source) suffers a nuclear transition from an excited state E_e to the ground state E_g it emits a γ photon that can be absorbed by a similar nucleus (named absorber) in order to excite from the ground state to the excited state (reverse nuclear transition). In that case, the γ photon will be absorbed by the absorber nucleus. In a case of free atoms, as in a gas during the emission of the γ photon the nuclei suffer a recoil effect and lose part of its energy. That photon is not able anymore to produce the excitation of the absorber nucleus, therefore the nuclear resonant absorption cannot take place. The recoil of both nuclei limits drastically the overlap of absorption and emission line, preventing any nuclear resonance. In 1958, Rudolf Mössbauer has shown that the probability of recoilless resonant absorption of γ photons is non-zero for the nuclei in solids, since they belong to atoms rigidly bonded in solid structures and the recoil is not possible being dissipated by lattice vibrations (phonons). A fraction f of the nuclei in solids (probability of the Mössbauer effect or Lamb-Mössbauer factor) can make the nuclear transition from E_g to E_e . Therefore, by definition, the Mössbauer effect is the recoilless nuclear resonant emission and absorption of γ radiation in solids. The application of this spectroscopy technique is limited to some isotopes: the most relevant one is the ^{57}Fe or its parent isotope ^{57}Co because it remains easy to use at room temperature and Fe is found in many systems in physics, chemistry, metallurgy, corrosion, biology, earth science, archeology, etc. The ^{57}Co source emits γ photons with an energy of 14.4 keV that excites the Fe nuclei in the samples.

The ^{57}Fe Mössbauer spectroscopy gives important information about the local chemical environment of nuclei, electronic and magnetic properties, valence and oxidation states of the Fe in all Fe-containing materials. It also gives unique information about the phase symmetry of each Fe species, present in the sample, by using the set of hyperfine parameters that unequivocally define each unequivalent Fe site in the material. The parameters that can be derived from a Mössbauer spectrum [54] may be classified as:

a) *dynamic parameters* (depend of the movement of the nuclei source and absorber in the solid); b) *energetic parameters* (depend on the interaction of electric charge Z_e , of the electric quadrupole moment Q and of the dipolar magnetic moment of the nucleus, with the electric and magnetic fields created by the electronic or molecular environment of the nucleus); c) *combined parameters* (depend on both the dynamic of nucleus and the electromagnetic interactions). Of interest for our studies are the following hyperfine parameters: a) ***the isomer shift*** (the electric monopole interaction between the electrons of an atom with the nucleus that depends on the size of the nucleus and the electronic charge density); b) ***the quadrupolar splitting*** (the electric quadrupolar interaction between the quadrupolar moment and the electric field gradient created by the external charges of the nucleus); c) ***the hyperfine field*** (measures the magnetic Zeeman splitting of the nuclear levels under the influence of the local magnetic field created by the s electrons at the nucleus). If a sample is magnetically ordered then its Mössbauer spectrum will consist of a sextet (six absorption lines) corresponding to the Zeeman splitted levels of the nucleus excited state. More generally, each unequivalent Fe site has a unique set of hyperfine parameters and by carefully fitting the Mössbauer spectra one can obtain a wide range of information regarding the phase composition of a sample, the nature, abundance and symmetry of these phases, the valence state of Fe as well as magnetic properties such as the direction and magnitude of the magnetic moment.

Experimental setup

The Mössbauer source used for the measurements is a monochromatic ^{57}Co source diffused into a Rh matrix. The Mössbauer spectra were recorded in a transmission geometry using a constant acceleration spectrometer while the sample made of 3 cm^2 ribbons was placed either at room temperature, or in a bath cryostat or a cryofurnace for low and high temperature measurements, respectively. The spectra were fitted by means of MOSFIT, a home-made program [55], based on the superposition of lorentzian quadrupolar doublets and magnetic sextets. The thickness of the ribbons ($25\mu\text{m}$) prevents the occurrence of thickness effects which originate a distortion of the hiperfine structure. Except the hyperfine field which is expressed in Tesla, all the other hyperfine parameters, isomer shift, quadrupolar splitting and linewidth of the absorption lines are expressed in mm/s.

V) Vibrating sample magnetometry

If a sample of any material is placed in a uniform magnetic field, created between the poles of an electromagnet, a dipole moment will be induced. If the sample vibrates with sinusoidal motion, a sinusoidal electrical signal can be induced in suitably placed pick-up coils. The signal has the same frequency of vibration and its amplitude will be proportional to the magnetic moment, amplitude, and relative position with respect to the pick-up coils system. The sample is fixed to a small sample holder located at the end of a sample rod mounted in an electromechanical transducer. The transducer is driven by a power amplifier which itself is driven by an oscillator. So, the sample vibrates along the Z axis perpendicular to the magnetizing field. The latter induced a signal in the pick-up coil system that is amplified. It results a DC signal that is proportional to the magnetic moment of the sample being studied. By using a vibrating sample magnetometer one can measure the DC magnetic moment as a function of temperature, magnetic field, angle and time. Some of the most common measurements done are: hysteresis loops, susceptibility or saturation magnetization as a function of temperature (thermomagnetic analysis), magnetization curves as a function of applied field (M(H)), angle (anisotropy), and magnetization as a function of time.

VI) Superconducting quantum interference device (SQUID) magnetometry

Another method to measure magnetization based on the change of flux through a pick-up coil, more sensitive but more time consuming, is with a Superconducting Quantum Interference Device (SQUID). A SQUID is made with superconducting loop with one or two Josephson junctions. The flux threading the superconductor circuit is constant, therefore, when the sample is suddenly extracted from inside the loop, a flux change will occur and the current will flow through the superconductor wire to compensate for the flux change. The device responds to very small changes in flux, of the order of 10^{-15} T m² therefore the SQUID is mostly used when small amounts of sample are available with small magnetic moments, since its sensitivity reaches 10^{-11} J/T. The measurement is time-consuming because it requires extraction of the sample at every point of measurement. It is also necessary to change the field in the superconducting magnet from one measuring point to another in the hysteresis loop.

2.3.2. Elemental characterization of as-cast state by energy dispersive X-ray spectroscopy (EDX)

The chemical composition, structure and magnetic properties of as-cast state of the *1a*, *2a* and *1b* samples have been thoroughly investigated by means of EDX, XRD, MS and VSM.

We have checked by energy dispersion X-ray spectroscopy (EDX) the true chemical composition of all the as-cast samples, in order to observe the stoichiometry of the alloys and to check the differences between the nominal composition and the measured one. The values obtained for each element as well as the overall composition, as revealed by EDX are depicted in Table II. The emission lines were visible for Fe and Pt in all cases, while the Nb was identified only in the case of *1b* sample and FePt – 1 sample from the second batch. As boron is a light element, it could not be identified by EDX and it was considered as having the nominal content. As it can be seen in the EDX image from Figure 2.5 the M line of Pt and L line of Nb are overlapped. Due to the very low content of Nb as compared with the Pt content, it was not possible to estimate the correct amount of Nb. Therefore, we considered that Nb has the nominal content.

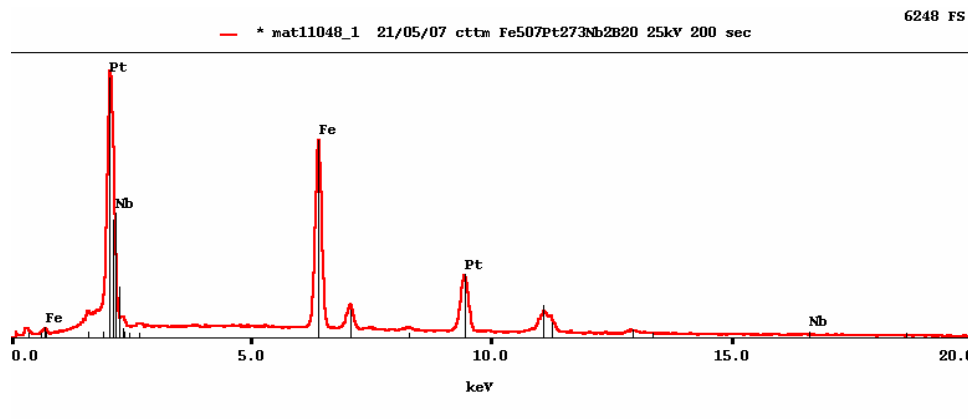


Figure 2.5. EDX diagram of *1a* sample

As it can be observed, a remarkable agreement (less than 1%) between the nominal composition and the real composition has been found, for Fe and Pt. Since the relative Fe:Pt content is crucial for the desired magnetic properties if an exchange coupled nanocomposite magnet is to be prepared, a good control of the stoichiometry is required. In the case of the melt spun ribbons, these EDX results show that errors as low as 1% for the stoichiometry are reached. This indicates that the melt spinning method is

indeed the most suitable method to synthesize this type of alloys with good control of stoichiometry.

Table II: The atomic percentage of each element of the as-cast alloys and their EDX measured composition. Estimated errors for the EDX measured compositions is in all cases ± 1 at.%

Sample	Nominal composition (at.%)	Fe (at.%)	Pt (at.%)	Nb (at.%)	Measured composition (at.%)
1a	Fe ₆₈ Pt ₂₁ Nb ₂ B ₉	76.0	24.0		Fe _{67.6} Pt _{21.4} Nb ₂ B ₉
1b	Fe ₆₈ Pt ₁₃ Nb ₂ B ₁₇	83.4	16.4	0.2	Fe _{67.5} Pt _{13.5} Nb ₂ B ₁₇
2a	Fe ₆₅ Pt ₂₅ Nb ₂ B ₈	71.5	28.5		Fe _{64.4} Pt _{25.6} Nb ₂ B ₈
FePt -1	Fe ₅₂ Pt ₂₈ Nb ₂ B ₁₈	64.2	34.6	1.2	Fe _{51.4} Pt _{28.6} Nb ₂ B ₁₈
FePt -2	Fe ₅₁ Pt ₂₇ Nb ₂ B ₂₀	65.0	35.0		Fe _{50.7} Pt _{27.3} Nb ₂ B ₂₀

2.3.3. X-ray diffraction (XRD)

The X-ray diffraction measurements were done at LPEC, Universite du Maine, Le Mans. Another set of X-ray diffraction measurements was made using synchrotron radiation at DESY-HASYLAB Hamburg. These measurements will be detailed in Chapter 2.5

2.3.3.1. Fitting methods

All the diagrams were fitted with the following programs:

a) *Material analysis using diffraction MAUD software*

The MAUD program is a least-squares refinement technique which combines the Rietveld method and a Fourier transform analysis, well adapted for broadened Bragg peaks [56]. This program allows thus to derive unit cell parameters, average crystallite size and microstrains. It is also suitable for quantitative phase and microstructure analysis. MAUD has been used for the quantitative analysis of the X-ray diagrams of as-cast and annealed samples.

b) *DATLAB software*

This powder diffraction software developed for polycrystalline multiple phase materials [57] allows deconvolution of complex overlapped Bragg peaks, calculation of position and linewidth of each individual Bragg reflection as well as the determination of lattice parameters. DATLAB has been used for the X-ray diagrams issued from the

synchrotron study (Chapter 2.5) and also for the peak analysis and calculation of lattice parameters in the as-cast and annealed samples.

c) Line profile

The Bragg peaks of the diagrams have been fitted to pseudo-Voigt line profile. The Voigt profile is a spectral line that is broadened by two types of mechanisms. The first one is strain related and would produce a Gaussian profile, and the other is related to the size of the grains and would produce a Lorentzian profile. All normalized line profiles can be considered to be probability distributions. The Gaussian profile is equivalent to a Gauss or normal distribution and a Lorentzian profile is equivalent to a Lorentz or Cauchy distribution. The Voigt profile is then a convolution of a Lorentz profile and a Gauss profile:

$$V(x, \sigma, \gamma) = \int_{-\infty}^{\infty} G(x', \sigma) \cdot L(x - x', \gamma) dx'$$

where x is the angular distance from line center, $G(x; \sigma)$ is the centered Gaussian profile:

$$G(x, \sigma) = \frac{e^{-x^2/2\sigma^2}}{\sigma\sqrt{2\pi}}$$

and $L(x, \gamma)$ is the centered Lorentzian profile:

$$L(x, \gamma) = \frac{\gamma}{\pi(x^2 + \gamma^2)}$$

The full width at half maximum (FWHM) of the Voigt profile can be found from the widths of the associated Gaussian and Lorentzian widths. The FWHM of the Gaussian profile is:

$$w_G = 2\sigma\sqrt{2\ln 2}$$

The FWHM of the Lorentzian profile is just $w_L = 2\gamma$. The full expression of the Voigt profile is given below:

$$y = y_0 + A_0 \frac{2 \ln 2}{\pi^2} \frac{w_L}{w_G} \int_{-\infty}^{\infty} \frac{e^{-t^2}}{\left(\sqrt{\ln 2} \frac{w_L}{w_G}\right)^2 + \left(\sqrt{4 \ln 2} \frac{x - x_C}{w_G} - t\right)^2} dt$$

A simplified pseudo-Voigt profile reads: $pV(x) = (1-\eta)G(x) + \eta L(x)$ where η is the mixing parameter. This parameter, that has values between 0 and 1, is an expression of the Bragg peak asymmetry and represents a quantitative estimation of the Lorentz relative proportion in the Voigt profile. When $\eta \rightarrow 0$, $w \rightarrow w_G$ and the peak is mostly a Lorentzian profile. When $\eta \rightarrow 1$, $w \rightarrow w_L$ and the peak is mostly a Gaussian profile.

d) Integral breadth calculation method

By using the lattice parameters, linewidths and mixing parameters of the assumed pseudo-Voigt profile of the Bragg lines, obtained for each Bragg reflection, we were able to calculate the average crystallographic domain size associated to the average diameter of the grains. The method we used is based on the integral breadth algorithm. The program calculates domain size and microstrain from input integral breadths of at least two physically broadened, due to the crystallite size, diffraction line profiles.

The integral breadth β is defined as the peak area divided by the maximum height of the peak. It is equivalent to the FWHM only for the symmetric Bragg peaks. In polycrystalline solids the lattice strains are not negligible and due to the method of synthesis, there are mechanical stresses induced in the plane of ribbons. Therefore, the Bragg peaks are rarely symmetric, especially in the case of nanocrystalline materials where the peaks are physically broadened. From this point of view it is a more accurate approach to use integral breadth instead of FWHM. Beyond the classic, so-called simplified, integral-breadth methods summarized in [58], the program calculates the root-mean-square strain (RMSS) and both surface- and volume-weighted domain sizes according to the 'double-Voigt' method [59,60], which is equivalent to the Warren-Averbach approach [61].

In contrast to the well-known Scherrer's method that takes into account, for estimation of the crystallite size, only the linewidth of the Bragg peak, the Warren-Averbach approach takes into account both the linewidth and the shape of the peak. It is based on the Fourier deconvolution of the measured Bragg peaks and furnishes at the same time the surface-weighted and volume-weighted domain sizes and root-mean-square lattice microstrain. In multiple phased ribbons, due to the preparation method, there is a gradient of solidification rate on the whole width of the ribbons, the stresses are expected to be induced by this gradient and consequently the lattice microstrains between

the atomic planes should be significant. Therefore, for estimation of the crystallite sizes, the integral breadth method is expected to give more reliable results than the Scherrer formula. It is to be mentioned that some reports [62, 63], have shown that in nanocrystalline materials, Scherrer formula gives systematically larger grain sizes than the Warren-Averbach method.

In the fitting method, the total integral breadth reads: $\beta = (1 - \eta)\beta_G + \eta\beta_L$ and the integral breadths of the Lorentz and the Gauss parts of the Voigt profile are separated into the size and distortion parts following the formulas [59]:

$$\beta_L = \beta_{sL} + \beta_{dL} \frac{s^2}{s_0^2}, \quad \beta_G^2 = \beta_{sG}^2 + \beta_{dG}^2 \frac{s^2}{s_0^2},$$

where $s=2\sin(\theta)/\lambda$ is the variable in the reciprocal space and s_0 is the peak center. Here, s_0^2 is taken for the first peak.

If the input data are given by pseudo-Voigt or Pearson-VII functions the FWHM and η parameters are transformed to β_L and β_G of the corresponding Voigt function according to the approximations given in [64].

In this fitting method, the size integral breadth gives the mean grain size assimilated to the surface and volume weighted crystallographic domain size D , while the distortion integral breadth gives the root-mean-square strain $\langle \varepsilon^2 \rangle$.

The size and strain are then calculated using the following formulas:

$$\langle D \rangle_s = \frac{1}{2\beta_{sL}}; \quad \langle D \rangle_v = \frac{\exp(k^2)}{\beta_{sG}} \operatorname{erfc}(k);$$

where: $k = \beta_{sL}/(\pi^{1/2}\beta_{sG})$ is the characteristic integral-breadth ratio of the Voigt function and

erfc is the complementary error function, defined as: $\operatorname{erfc}(k) = 2/\sqrt{\pi} \int_k^\infty \exp(-t^2) dt$

$$\langle \varepsilon^2(L) \rangle = \frac{1}{s_0^2} \left(\frac{\beta_{dG}^2}{2\pi} + \frac{\beta_{dL}}{\pi^2} \frac{1}{L} \right).$$

where $\langle \varepsilon^2 \rangle$ is the strain, L is the column length (distance between two cells in a real space) orthogonal to diffracting planes.

The RMMS is assimilated to the lattice microstrain which is defined as the amount (change in size or volume) by which a crystal lattice deforms under stress or force. The microstrain is given as a ratio of the deformation to the initial dimension of the lattice, being a non-dimensional parameter.

2.3.3.2. Experimental XRD Results

- Fe-rich batch

The structure of the samples was determined by performing XRD studies with the powder diffraction method in a Bragg-Brentano θ - 2θ geometry using a Philips X'Pert diffractometer, at LPEC, Universite du Maine. The Cu K_{α} radiation wavelength of 1.54 Å was used for all powder diffraction experiments. The X-ray beam was incident to the ribbon plane. Figure 2.6 shows the X-ray spectra of *1a*, *1b* and *2a* as-cast samples. It can be observed that the spectra of *1a* and *2a* samples exhibit sharp Bragg peaks, indicating the high degree of crystallinity in these samples. On the contrary, the as-cast *1b* peaks exhibit large linewidths which indicate the lack of long range ordering, typical for low crystallinity as in nanocrystalline grains.

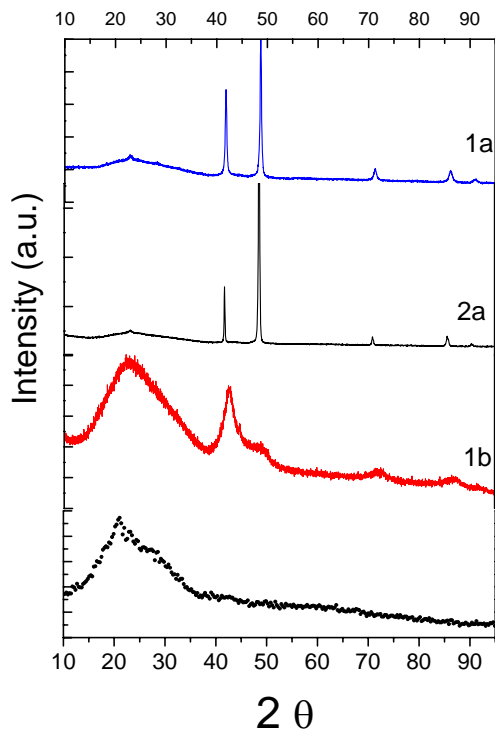


Figure 2.6: a) Raw X-ray diffractograms for *1a*, *1b* and *2a* as-cast ribbons. Dotted diagram corresponds to the glass holder and resin used for fixing the samples.

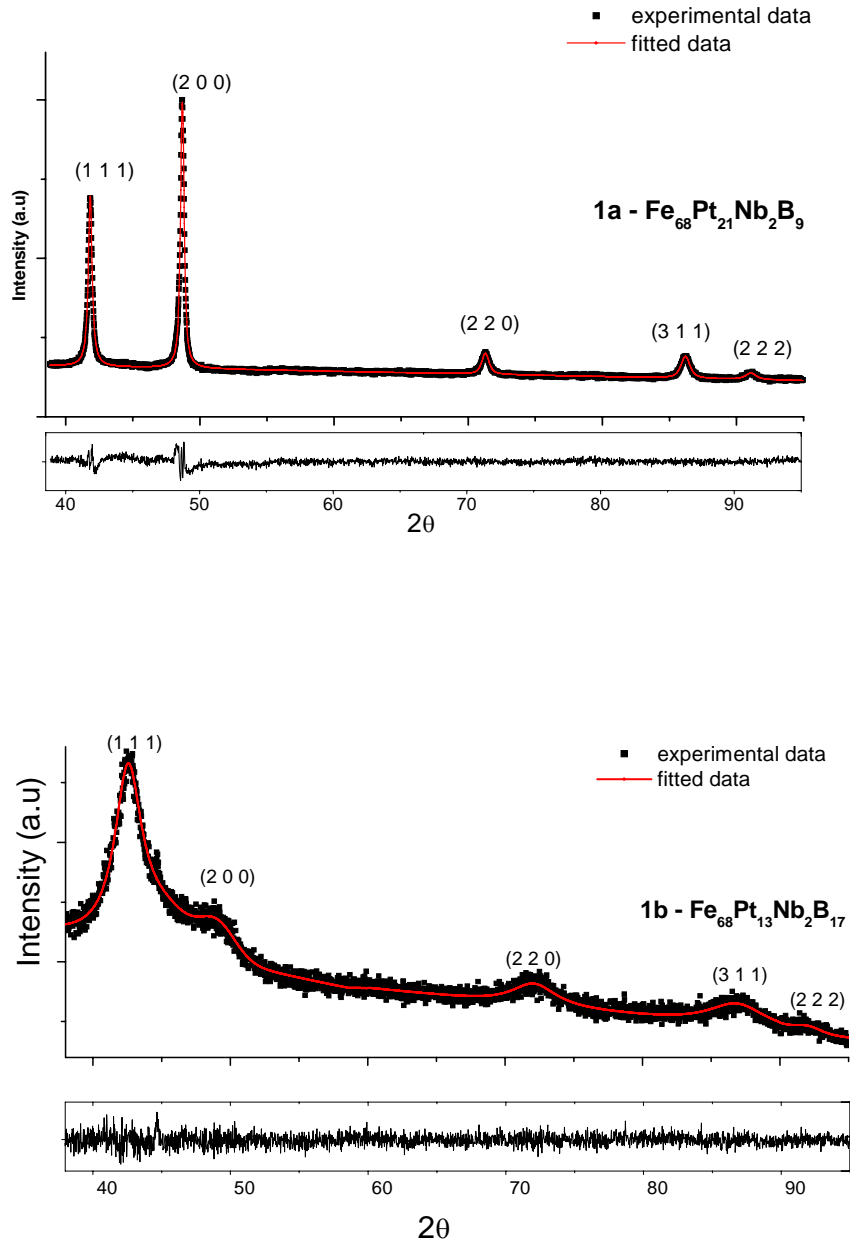


Figure 2.7: X-ray diffractograms of *1a* and *1b* sample fitted with the DATLAB software. The indexed lines belong to f.c.c. Al FePt. Bottom graph is the difference between fitted and experimental data.

Table III. Lattice parameters and grain size for all the as-cast samples

As cast samples	Al fcc FePt	Grain size (nm)
	a (Å)	
<i>1a</i> - $\text{Fe}_{68}\text{Pt}_{21}\text{Nb}_2\text{B}_9$	3.756 ± 0.007	38 ± 4
<i>2a</i> - $\text{Fe}_{65}\text{Pt}_{25}\text{Nb}_2\text{B}_8$	3.779 ± 0.009	60 ± 5
<i>1b</i> - $\text{Fe}_{68}\text{Pt}_{13}\text{Nb}_2\text{B}_{17}$	3.684 ± 0.023	3 ± 1
<i>FePt-1</i> $\text{Fe}_{52}\text{Pt}_{28}\text{Nb}_2\text{B}_{18}$	3.805 ± 0.004	11 ± 3
<i>FePt-2</i> $\text{Fe}_{51}\text{Pt}_{27}\text{Nb}_2\text{B}_{20}$	3.796 ± 0.005	7 ± 2

All the diffraction Bragg lines for the *1a* and *2a* samples have been indexed as belonging to a system of Bragg reflections that account for the disordered face-centered-cubic *A1* phase, with space group *Fm3m*. The indexation was done in agreement with the JCPDS powder diffraction file (PDF) 29-0718 that accounts for the FePt phase with *Fm3m* space group and cubic symmetry. The fitting has been performed with DATLAB software. The results of the fitting as well as the indexation of the Bragg peaks for *1a* and *1b* samples are illustrated in Figure 2.7. The agreement between the experimental and the fitted diagram is remarkable in both cases, as it can be observed in this figure. This confirms that the use of the mentioned fitting methods gives reliable results, as proven by the correctness of the fit.

It is quite difficult to distinguish between the main diffraction lines of ordered tetragonal *L1₀* (JCPDS powder diffraction file 43-1359, space group *P4/mmm*) and disordered cubic *A1* FePt. The most important Bragg reflections for *A1* and *L1₀* occur almost in the same angular positions on the diagram. It is the case of the Bragg reflections belonging to the family of planes (1 1 1), (2 0 0), (2 2 0) and (3 1 1). In the literature [40-46] the tetragonal phase is usually identified by the occurrence of the so-called “superlattice” Bragg peaks corresponding to (0 0 1) and (1 1 0) reflections of the face-centered-tetragonal lattice that can only be found in the *L1₀* phase. These two superlattice peaks occur, for the wavelength we have used (Cu $K\alpha$), at about 24° and 32° respectively. As it can be seen in Figures 2.6 and 2.7, these peaks do not occur in the diffractogram. Therefore, we have concluded that the peaks observed belong to the f.c.c. *A1* phase, as it has been found in a large number of other reports [35-37, 42, 65-67]. The very broad line of reduced intensity that appears in all the X-ray diagrams between 15 and 40° (in 2θ) is the signature of the sample holder and the epoxy resin that was used for measurements.

In *1a* sample the lattice parameter of the FePt f.c.c. *A1* phase was found to be $a = 3.756 \pm 0.007$ Å. Because of the difference between the theoretical lattice parameter ($a = 3.816$ Å) and the obtained one, we can assume that the disordered *A1* phase contains also Nb and B atoms that accommodate randomly Fe and Pt sites in the fcc phase. Therefore, it is plausible to assume that the fcc phase we have indexed in the *1a* as-cast XRD diagram is in fact a FePt based disordered solid solution.

We have calculated, based on the integral breadth approach, the crystallite size for all the Bragg peaks indexed in the fcc *A1* system. We find that the average crystallite size for the *1a* sample is 38 ± 4 nm. The error is the one given by the fit program. It has to be mentioned that the linewidths were not corrected for instrumental broadening and the errors in estimation could be larger as the average crystallite size might also be larger due to instrumental broadening. As witnessed by the sharp Bragg lines, the as-cast state of the *1a* sample is mainly nanocrystalline with well-formed crystallites. All the calculated lattice parameters and average grain sizes are given in Table III.

For the *2a* sample, the X-ray spectrum looks quite similar. No diffraction lines of unalloyed α -Fe are visible. The sharp Bragg peaks are assigned to the cubic *A1* FePt phase, as in the case of *1a* sample. In this case, the average crystallite size is determined to be 60 ± 5 nm, higher than the one obtained for *1a* sample. This indicates a better crystallization of the as-cast *2a* sample compared to the *1a* sample. It is worth noticing that in both cases, the most intense diffraction line is the one corresponding to (2 0 0) planes, in contrast with the bulk case where the most intense Bragg line corresponds to the (1 1 1) reflection. This indicates the high probability of strong in-plane crystal anisotropy.

Sample *1b* shows quite different structural characteristics. The spectrum for *1b* exhibits very broad lines. The broad contribution centered at about 25° could be attributed to both some topological disorder and to the signal given by the resin used to fix the sample on the sample holder (as in the case of *1a* and *2a* sample). The observed Bragg lines are in almost the same positions as in the case of *1a* and *2a* samples, but much more broadened. They are also attributed to the fcc *A1* phase, but extremely disordered. The mean grain size is found to be 3 ± 1 nm. The structure of this sample is a solid solution of disordered fcc *A1* symmetry. It is probable that, this solid solution could be a precursor for the formation of FePt phases after appropriate crystallization treatment. Consequently, in the *1b* sample, it is more likely to produce by subsequent annealing a microstructure formed by hard and soft nanocrystalline grains, with controlled sizes.

- Pt-rich batch

The XRD patterns of the FePt – 1 and FePt – 2 as-cast samples, plotted in Figure 2.8, differ from that of the Fe-rich batch of samples. The spectra exhibit Bragg reflections that correspond to the *A1* fcc FePt phase, as it is indexed on the Figure, but the lines are larger than in the case of *1a* and *2a* samples and narrower than in the case of *1b* sample. This fcc symmetry belongs to a disordered FePt solid solution with same Bragg reflections as in the case of Fe-rich batch of as-cast samples. Contrary to the *1a* and *2a* samples, in the *FePt – 1* and *FePt – 2* as-cast samples the (1 1 1) peak is the most intense, as in the case of bulk *A1* FePt phase, meaning that in these samples the crystal anisotropy is much more reduced. The very broad line observed in the spectrum between 15° and 35° (in 2θ) is similar as the one from the Fe-batch as-cast XRD diagrams being attributed to the resin used for fixing the sample on the sample holder during the XRD measurements.

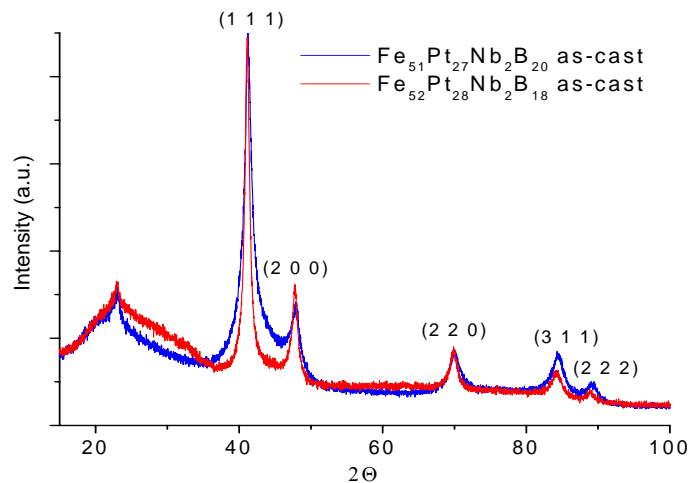


Figure 2.8: XRD diagrams for FePt – 1 and FePt – 2 as-cast samples. Bragg lines indexed on the spectra belong to the fcc *A1* FePt-rich solid solution

The XRD patterns are intently depicted to superpose to each other to better observe the difference between them. The most clear difference comes from the linewidth of (1 1 1) and (2 0 0) reflections. The pattern of the sample with 20 at% boron has larger Bragg peaks than the one with 18 at% boron. It is well established that the larger the linewidth of the Bragg peaks in intermetallic alloys, the higher the degree of amorphization, as the linewidth is inversely proportional with the crystallites sizes. This proves the boron effect that is indeed to ensure better amorphization. The XRD patterns

have been fitted and analyzed using the DATLAB software, described earlier. The calculated lattice parameters for the FePt – 1 and FePt – 2 as-cast samples, obtained from the fitting results, are depicted in Table III. The grain sizes, calculated with the integral breadth method, confirm what can be easily observed on the graph. The average grain size for FePt – 1 as-cast sample is 11 ± 3 nm while for FePt – 2 as-cast sample the grain size is 7 ± 2 nm. As expected, the calculated average grain size is smaller in the sample with better amorphization, corresponding with the larger linewidth observed in the main Bragg reflections in the XRD patterns. In the Pt-rich batch, the as-cast state is thus proven to be an fcc disordered A1 FePt solid solution, as is the case of the *1b* sample but with larger grain sizes. It is to expect that upon annealing of these samples the microstructure will evolve towards the formation of the tetragonal $L1_0$ phase.

2.3.4. As-cast state characterization by Mössbauer spectroscopy

-Fe-rich batch

The Mössbauer spectrometry was done on the *1a*, *2a* and *1b* samples, to complete the structural characterization of the as-cast state. We have performed ^{57}Fe Mössbauer spectrometry in transmission geometry using a ^{57}Co source in a Rh matrix. Figures 2.9, 2.10 and 2.11 present the Mössbauer spectra of the as-cast *1b*, *1a* and *2a* samples, respectively, recorded at 300K and 77K.

The 300K and 77K spectra of *1b* sample (Figure 2.9) exhibit broad magnetic sextets, typical of distributed Fe environments encountered in Fe-rich amorphous ribbons. The shape of the spectra confirms the XRD results where an amorphous-like solid solution has been identified. Following these results, the spectra were fitted with a discrete hyperfine field distribution. The fitting procedure has been done using the Mosfit software [55]. The distribution contains 15 components with increasing hyperfine field values from 0 to 40 T. The average hyperfine fields obtained after fitting were 23.1 T at 300 K and 26.5 T at 77 K. These values are in agreement with other values of average hyperfine fields obtained on amorphous Fe-rich intermetallic ribbons [61]. The central lines of the broad, sextet, presents an asymmetry, more pronounced in the 77K spectrum. This asymmetry has to be taken into account by involving a correlation between the

distribution of hyperfine field and the distribution of isomer shift. This correlation is explained by the different coordination of Fe sites, typical for a chemically disordered Fe environment, as in amorphous-like systems.

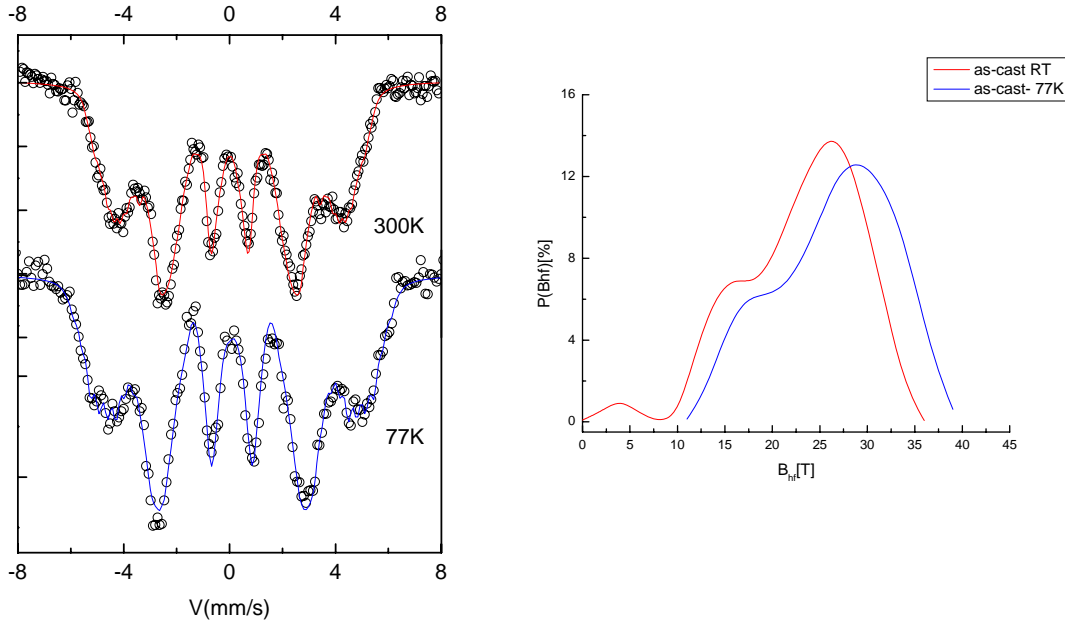


Figure 2.9: 300K and 77K Mössbauer spectra of as-cast *1b* sample together with their hyperfine field distributions.

The hyperfine field (HF) distributions plotted in the right part of Figure 2.9 show a bimodal-type large gaussian profile distribution, that is characteristic for disordered Fe environment encountered in amorphous-like alloys, with two main environments for Fe. From the numerical fitting with two Gaussian profiles, we have obtained for the low field mode an average HF of 16 T and 18 T for 300K and 77K respectively and for the high field mode average HF of 26 T and 29 T for 300K and 77K respectively. The relative proportion of the high-field to low-field relative contributions to the HF distributions is about 3:1. From the HF values we can presume that the low field mode corresponds to an disordered precursor that would give rise upon annealing to a boride (possibly Fe_2B) phase while the high field mode would give rise to fcc FePt phase.

The 300K Mössbauer spectrum of *1a* sample, presented in Figure 2.10, presents a convolution of several magnetic sextets with narrow lines, characteristic for multiple magnetic phased crystalline samples and also a strong paramagnetic component. This is a feature consistent with the topological order that has been observed in the XRD diagrams

of this sample. The model used for the fitting of the magnetic part of the spectrum consists of two HF distributions, one at high field to account for the magnetic part and the other one at low field to account for the paramagnetic component. The high field distribution had a correlation of the isomer shift with HF to better fit the asymmetric intermediate lines. The relative intensity is the free parameter during the fit. The HF distribution is given also in Figure 2.10. The average HF found for the high field mode was 24 T and its relative abundance was 79%. The relative abundance of the paramagnetic compound was found to be 29%.

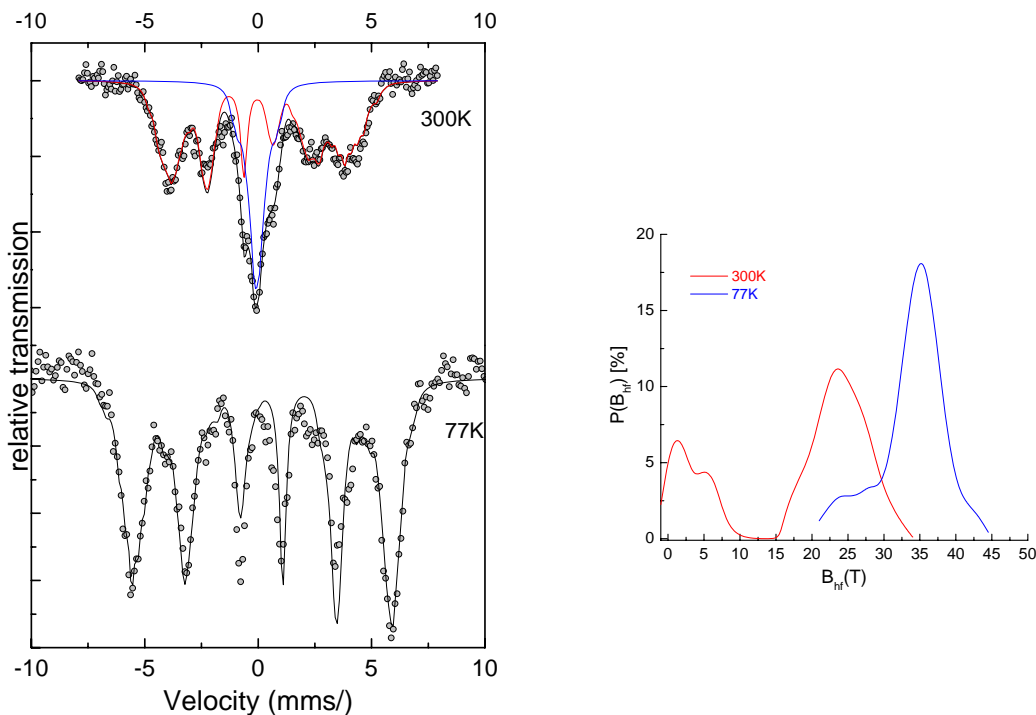


Figure 2.10: 300K and 77K Mössbauer spectra of as-cast *1a* sample.

The spectrum at 77 K reveals no more paramagnetic component. At low temperatures, this paramagnetic component has vanished. There are two possible explanations for the origin of this paramagnetic component. First is the presence of a fraction of grains that are superparamagnetic (SPM) at room temperature and become magnetically blocked at temperatures between 300 and 77K. This possibility can be ruled out for the following reason. The average grain size, as calculated from XRD data, is almost 40 nm; such large grain size rule out the possibility to have an important fraction

of grains (30%) small enough to be SPM. Second explanation concerns a possible magnetic disorder-order transition at low temperatures. It must be recalled that XRD results show the occurrence of only one crystal phase, the A1 fcc FePt phase. Therefore, it is not possible that the paramagnetic component could belong to another crystal phase, not seen in XRD diagram, since the relative intensity is so large. On the other hand, in a number of previous reports [28-29,46] it has been shown that A1 phase is magnetically and topologically disordered at room temperature. Therefore, we can assume that this paramagnetic component represents in fact the fraction of A1 fcc phase that is magnetically disordered. This fraction becomes magnetically ordered at 77 K. The model used for fitting of the 77K spectrum is again a HF distribution but with larger hyperfine fields, as expected due to the decrease of temperature. Due to the increased magnetic ordering at 77K compared to 300K the HF distribution is narrower, as seen in Figure 2.10. The results of fitting are presented in Table IV. IS and 2ε values are again consistent with a phase with cubic symmetry.

Table IV: Average hyperfine parameters obtained after fitting of the spectra from Figures 2.9 – 2.11:

300K:

	IS (mm/s)	$\Gamma/2$ (mm/s)	2ε (mm/s)	B_{hf} (T)	%
1A	0.16	0.18	0	24.0	71
	0.08	0.18	0	2.9	29
1B	0.14	0.17	-0.02	23.1	100
2A	0.15	0.18	0	27.4	100

77K:

	IS (mm/s)	$\Gamma/2$ (mm/s)	2ε (mms/)	B_{hf} (T)	%
1A	0.35	0.18	0.04	34	100
1B	0.24	0.17	-0.02	26.5	100
2A	0.37	0.18	0.02	33.5	100

The estimated errors are: ± 0.02 mm/s for IS and $QS/2\varepsilon$, ± 0.1 T for B_{hf} and ± 1 for the relative proportion

Taking into account the XRD results, where only fcc *A1* phase has been identified, we may safely presume that the magnetic HF distribution can be attributed to the FePt *A1* disordered phase with Nb and B atoms randomly accommodating the crystallographic sites of Fe and Pt or situated in the grain boundaries between crystalline FePt grains. All the values of the hyperfine parameters obtained from fitting of the Mössbauer spectra are listed in Table IV.

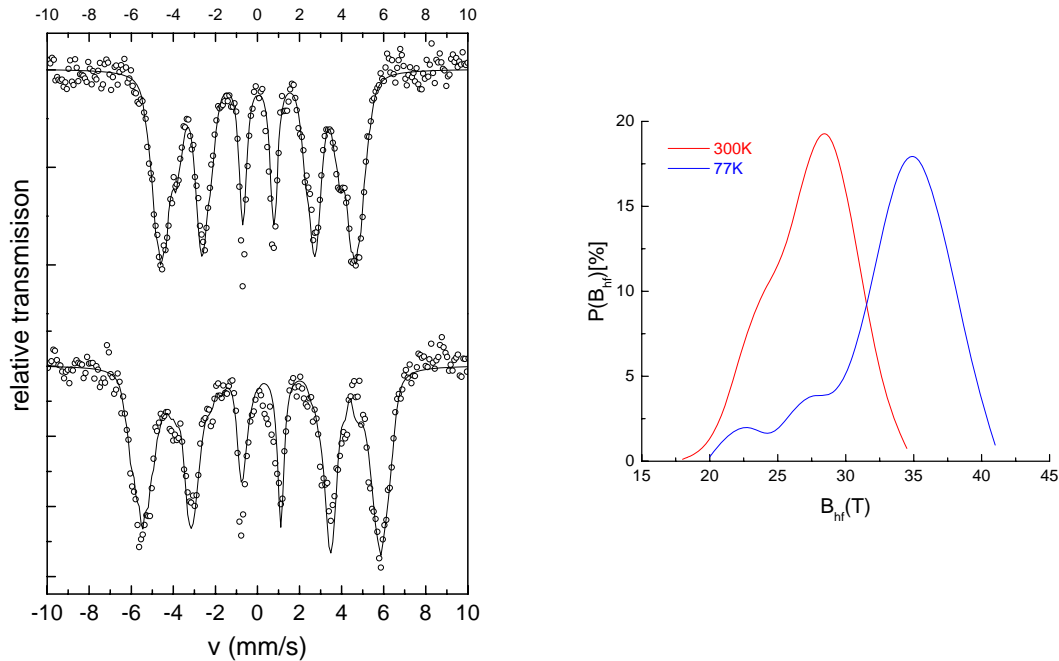


Figure 2.11: 300K and 77K Mössbauer spectra of as-cast 2a sample.

The 300K and 77K Mössbauer spectra of *2a* sample are presented in Figure 2.11. It must be observed that at 300 K there is no paramagnetic component and the spectrum is fitted with HF distribution as in the case of *1a* sample. The HF average parameters are highly similar with the magnetic part from the *1a* case. At 77K the spectrum is very similar to the *1a* sample and the model of fitting was the same. The results, as it can be seen from Table IV, are very similar. The hyperfine parameters are slightly higher, compared to the values obtained at 300K, that is an expected event due to the increased degree of magnetic ordering that appears upon decreasing temperature.

The presence of the paramagnetic component in *1a* sample, i.e. the fraction of fcc *A1* phase that is magnetically disordered at room temperature can be also understood if we examine the XRD results. It can be seen that, in the case of *1a* sample the average

grain size is about 40 nm while for the case of *2a* sample, the average grain size is about 60 nm. Due to the better crystallinity in the *2a* sample, the grains are larger and there is no magnetic disorder in the fcc A1 phase. For this reason the paramagnetic component, that reaches a relative intensity of 29% in the *1a* sample at 300 K, lacks completely in the spectrum of *2a* sample.

The origin and evolution of this paramagnetic component will be studied in the following section where an XRD and Mössbauer investigation on *1b* annealed samples will be carried out.

All the Mössbauer results confirm the XRD data on the as-cast *1a*, *1b* and *2a* samples. It has been shown also by Mössbauer spectroscopy that *1a* and *2a* as-cast samples are crystallized and, besides the already discussed paramagnetic component in *1a*, they present distributed sextets with hyperfine fields comparable with those of Fe-rich nanocrystalline alloys. *1b* sample is proven to be highly disordered as shown by the typical broad pattern of the Mössbauer spectra, observed at 77K and 300K. The fact that the as-cast state of the *1a* and *2a* samples is already crystalline indicates that not so good hard magnetic properties should be expected in these samples. These properties are discussed in the next Chapter.

- Pt-rich batch

The 300K Mössbauer spectra of the two as-cast samples from the Pt-rich batch, FePt – 1 and FePt – 2 samples, are illustrated in Figure 2.12. Both spectra exhibit broad magnetic sextets as observed for distributed chemical environments of Fe nucleus, accounting for the short-range-order encountered in Fe-rich amorphous-like ribbons. They are similar to the spectrum for the *1b* sample. The spectra were fitted with a discrete hyperfine field distribution. As in the case of *1b* sample, the distribution contains 15 components with increasing hyperfine field values from 0 to 40 T.

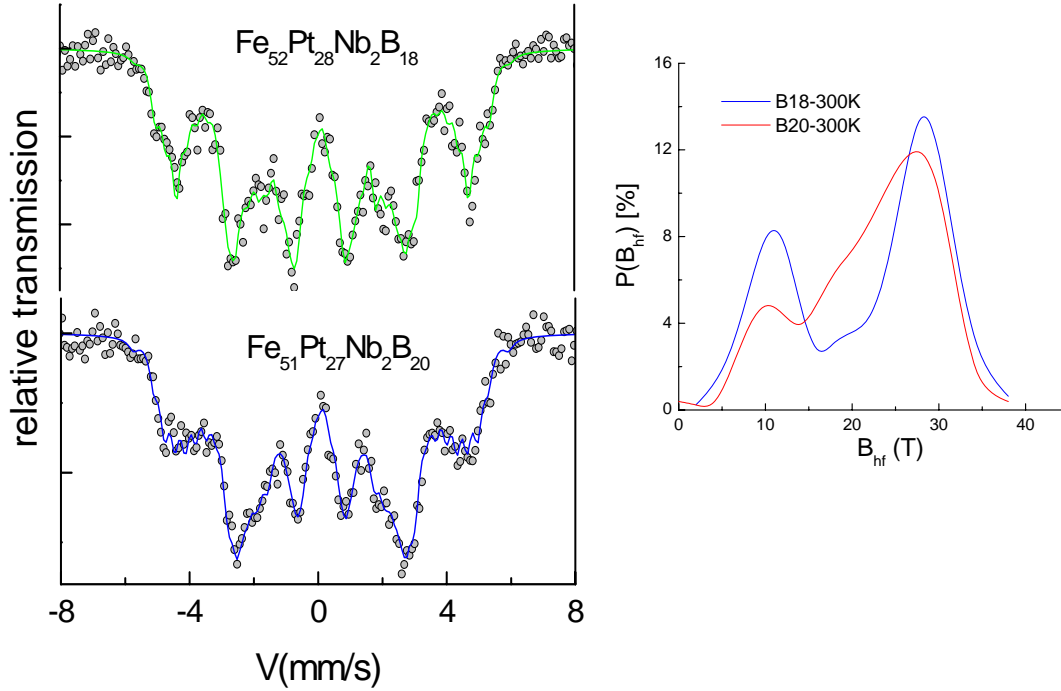


Figure 2.12: 300K Mössbauer spectra of as-cast FePt – 1 (top) and FePt – 2 (bottom) samples together with their hyperfine field distribution

From the observation of the most external broad Mössbauer lines (lines 1 and 6), it appears that these are larger and less intense in the case of FePt – 2 sample than those of FePt – 1 sample. Also in the XRD spectra, a larger line was observed for the (1 1 1) and (2 0 0) Bragg reflections, a result that is now confirmed by Mössbauer spectroscopy and show more topological disorder, better amorphization for the sample containing 20 at% boron. This can be further confirmed if we observe the resulted hyperfine field distributions. The average hyperfine field obtained after fitting is 21.8 T for FePt – 1 and 22.2 for FePt – 2 samples. These values are both lower than the case of *Ib* sample but in agreement with the Fe content which is lower than in the case of *Ib* sample.

In both cases we observe a bimodal hyperfine field distribution which accounts for two types of Fe disordered environments, one mostly magnetic and the other one with reduced hyperfine field. The two high field and low field modes have average hyperfine fields of about 27 T and 10 T, respectively. In the case of FePt – 1, the two modes of the distribution are well separated and the intensity of the high field part is more intense, while in the case of FePt – 2 sample, the low and high field distribution modes are not so well separated, the results confirming thus the observation we made on the width of the

broad lines in the two cases. It follows that the as-cast state of FePt – 2 sample is more homogeneous due to the increased boron content. From the value of the average hyperfine fields we can conclude that the low field part of the distribution corresponds to a FeB – rich phase, while the high field part, with hyperfine field values similar to those obtained in the *1a* and *2a* samples, corresponds to the FePt – rich cubic phase. These two types of environment, one FeB-rich the other one FePt-rich, are only observed in the Mössbauer spectra. It is to be mentioned that the XRD diagram showed only the Bragg lines corresponding to the FePt A1 cubic phase. Since the X-ray absorption factor for FeB is small compared to the one for FePt it is not surprising that the disordered FeB-rich precursor could not be observed in the XRD diagram. Following the argument from the as-cast *1b* sample we can say that in Pt-rich batch of as-cast samples there is a topological order which results in the formation of nanocrystalline fcc A1 lattice coupled with a chemical disorder which results in the amorphous-like feature of the Mössbauer spectra. Even if the atoms are forming a lattice with fcc A1 symmetry, the environment of Fe is distributed, therefore we may assume that the fcc A1 FePt solid solution in these cases is highly disordered and represents a suitable precursor for formation of hard and soft magnetic phases, upon annealing. Nevertheless, from the hyperfine field distributions we have been able to identify the two high field and low field parts that correspond to FeB-rich and FePt-rich environments for Fe nuclei respectively. These observations will be confirmed by the Mössbauer analysis of the annealed FePt-1 and FePt – 2 samples, in the next Chapter.

2.3.5. Magnetic characterization of the as-cast state by Vibrating sample magnetometry (VSM)

For a full characterization of the as-cast state, we have performed magnetic characterization by means of 300K hysteresis loops recorded with a VSM under applied magnetic field of up to 1.5 Tesla and also with a SQUID under applied field of up to 3 T. The field was applied parallel to the ribbon plane. In the case of as-cast FePt – 1 and FePt – 2 samples, the loops were recorded also at 5 K and in applied field perpendicular to the ribbon plane. VSM magnetic measurements have been done at Universite de Rennes and at Trinity College Dublin while SQUID measurements at the Institute for Experimental Physics, Kosice.

- *Fe-rich batch*

The hysteresis loops for the three as-cast samples are presented in Figure 2.13.

The loop for the *1b* sample exhibits characteristics that are typical for a soft magnetic alloy with high saturation polarization (around 1.2 T), very low coercivity and no remanence. The saturation is reached at low values of applied field (0.5 T). These features are consistent with good soft magnetic character of the sample.

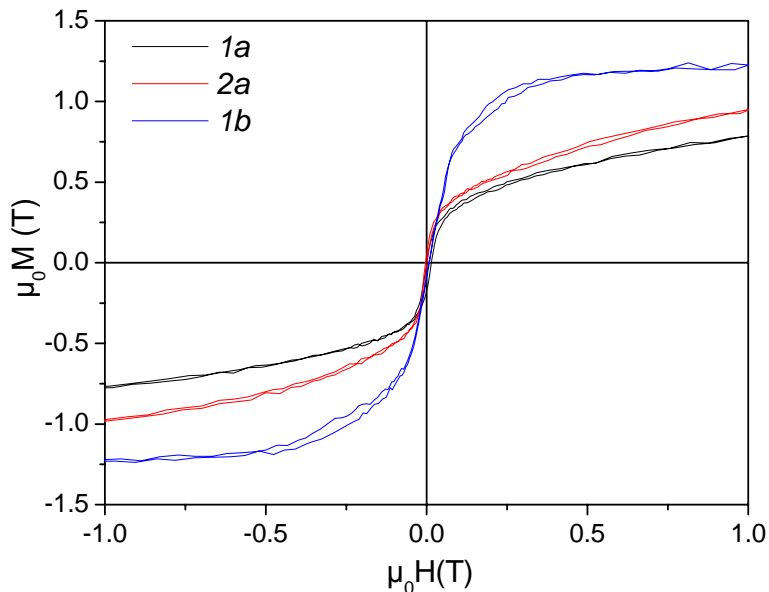


Figure 2.13: 300K hysteresis loops for the as-cast *1a*, *2a* and *1b* samples.

The *1a* and *2a* samples exhibit sensibly lower magnetization values than the *1b* sample, as it can be seen from Table V. The magnetization approaches the saturation

slower than in the case of *Ib*. The lowest magnetization from the 3 samples is reached for the *Ia* samples. This is in agreement with Mössbauer results where a paramagnetic component of 29% relative abundance has been fitted in the Mössbauer spectrum at 300 K.

Table V. Magnetic parameters: coercive field H_c , remanent magnetization M_r and saturation (or maximum) magnetization M_s , as revealed from the hysteresis loops for the as-cast samples

As cast samples	$\mu_0 H_c$ (mT)	$\mu_0 M_r$ (mT)	$\mu_0 M_s^*$ (T)
<i>Ia</i> - $Fe_{68}Pt_{21}Nb_2B_9$	6.8	0	0.77
<i>2a</i> - $Fe_{65}Pt_{25}Nb_2B_8$	2.1	3.6	0.93
<i>Ib</i> - $Fe_{68}Pt_{13}Nb_2B_{17}$	0.5	0	1.24
<i>FePt - 1</i> $Fe_{52}Pt_{28}Nb_2B_{18}$: 300K	12	16	1.20
<i>FePt - 1</i> $Fe_{52}Pt_{28}Nb_2B_{18}$: 5K	5	28	1.36
<i>FePt - 2</i> $Fe_{51}Pt_{27}Nb_2B_{20}$: 300K	0.29	68	1.27
<i>FePt - 2</i> $Fe_{51}Pt_{27}Nb_2B_{20}$: 5K	0.16	11	1.47

* For Fe-rich batch the maximum magnetization, for Pt-rich batch the saturation magnetization

- Pt-rich batch

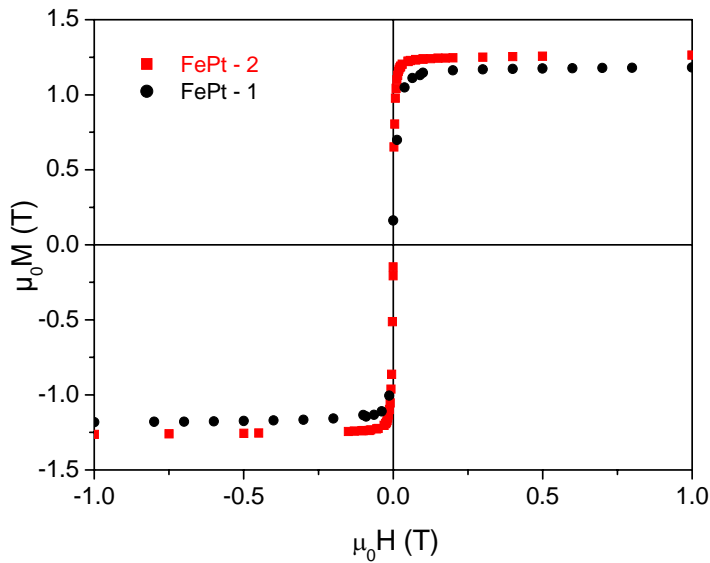


Figure 2.14: 5K and 300K hysteresis loops in parallel field for FePt – 1 sample.

The 5K and 300K hysteresis loops for the as-cast FePt – 1 and FePt – 2 samples, recorded with SQUID in an applied field of up to 4 T, are shown in Figures 2.14 and 2.15.

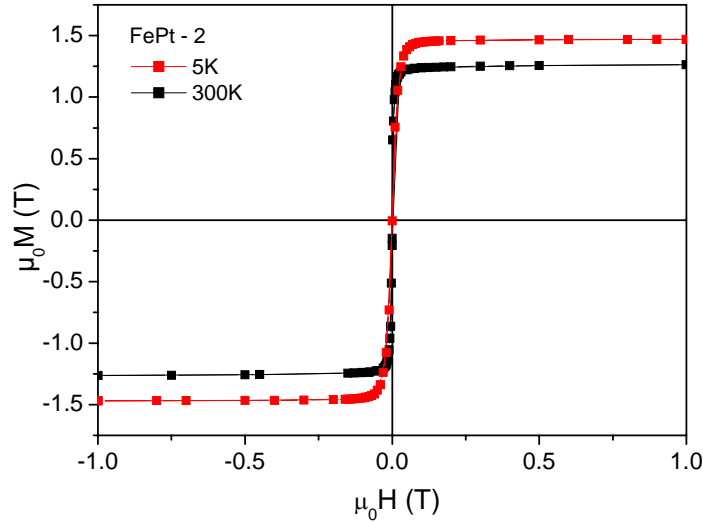


Figure 2.15: 5K and 300K hysteresis loops in parallel field for FePt – 2 sample.

All the hysteresis loops recorded for the two Pt-rich samples are typical for amorphous soft magnetic materials. In parallel applied field, the magnetization saturates almost immediately after applying the magnetic field, and the saturation magnetization reaches high values, comparable with Fe-rich soft amorphous magnets [68]. The loops show very low coercivity and remanence, and are similar at 300K and at 5K. At low temperature, as expected due to the lack of thermal fluctuations, the magnetization values are higher. The saturation magnetization, remanence and coercivity values are plotted in Table V.

The saturation magnetization values are slightly larger in the FePt – 2 sample than in their FePt – 1 counterparts. Also the coercivity and remanence are even more reduced in the case of FePt – 2 sample. This is due to the higher disorder in the as-cast state and consequently more soft magnetic character in the sample with more boron content. The as-cast FePt – 1 and FePt – 2 samples with a soft magnetic disordered fcc precursor already formed in the as-cast state, together with the *Ib* samples from the Fe-rich batch of samples, look like promising candidates for developing, by annealing a microstructure of hard and soft magnetic phases that may exhibit exchange-spring behavior.

In the following we will study the formation and evolution of crystalline phases in the as-cast samples by means of thermal analysis.

2.4. Thermal analysis

The nature and the stability with temperature of the nanocrystalline phases that occur in the as-cast samples are of relevant importance for the complete characterization. These phases evolve with temperature and this evolution can be studied by the differential scanning calorimetry (DSC).

DSC is a thermoanalytical technique in which the difference between the amounts of heat required to increase the temperature of a sample compared to that of a reference is measured as a function of temperature. Both the sample and reference are maintained at nearly the same temperature throughout the experiment.

The basic principle underlying this technique is that, when the sample undergoes a physical transformation such as phase transitions, more (or less) heat will need to flow through it than the reference to maintain both at the same temperature. Whether more or less heat must flow to the sample depends on whether the process is exothermic or endothermic. For example, as a solid sample melts to a liquid it will require more heat flowing to the sample to increase its temperature at the same rate as the reference.

This is due to the absorption of heat by the sample as it undergoes the endothermic phase transition from solid to liquid. Likewise, as the sample undergoes exothermic processes (such as crystallization) less heat is required to raise the sample temperature. By observing the difference in heat flow between the sample and reference, differential scanning calorimetry is suitable to measure the amount of heat absorbed or released during such transitions.

Disorder-order phase transitions such as amorphous-to-crystalline transformation in bulk alloys are observed as exothermic events. DSC may also be used to observe more subtle phase changes, such as glass transitions.

- Fe-rich batch

The thermal analysis was performed on all the as-cast ribbons from the Fe-rich batch using a Netzsch DSC 4 facility in high vacuum (10^{-3} Torr). The measurements were performed at the Rostock University, Germany. Several samples of ribbons with masses

around 50 mg were weighted for each experiment. These samples were linearly heated up to 1000°C with heating rates varied between 5 and 50 K/min in order to observe all the structural effects and phase transformations that may occur in the Fe-Pt-Nb-B alloys.

Figures 2.16 to 2.18, respectively, depict the DSC scans of the *1a*, *2a* and *1b* samples taken with various heating rates from 10 to 20K/min. Between 200°C and 500°C the scans for *1a* and *2a* samples (Figures 2.16 and 2.17) show quite linear increase of the heat exchange flow. Small kinks in the heat flow and also some exothermic effects are observed between 550°C and 800°C. These small events are mostly related to the interphase atomic diffusion. Also, during annealing, the thermal stresses induced in ribbons during the rapid solidification synthesis techniques are relaxed. This process is accompanied by small amounts of heat exchanged with the reference and is responsible for the small exothermic effects observed in the *1a* and *2a* scans.

When the ribbon structure undergoes disorder-order phase transitions such as crystallization from amorphous state, significant well-defined exothermic phenomena with high activation energy do occur. No such significant exothermic peaks are observed in *1a* and *2a* samples. This is in agreement with the XRD and Mössbauer results, where we have observed that the as-cast state is mainly crystallized, therefore no significant exothermic effect eventually related to the crystallization can occur in the *1a* and *2a* samples.

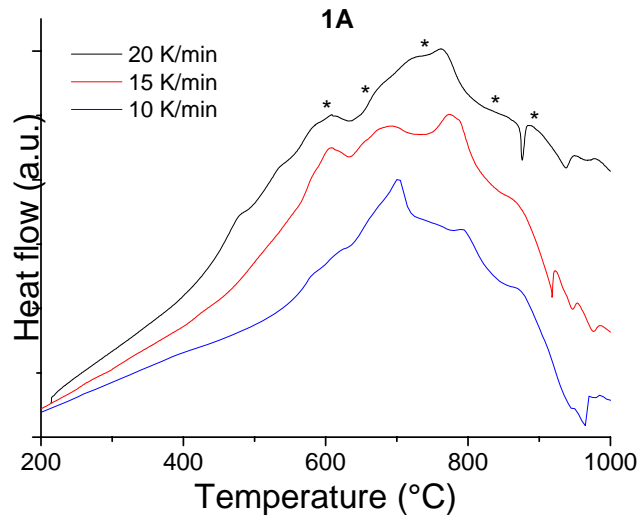


Figure 2.16: DSC scans for *1a* as-cast sample recorded at heating rates between 10 and 20 K/min.

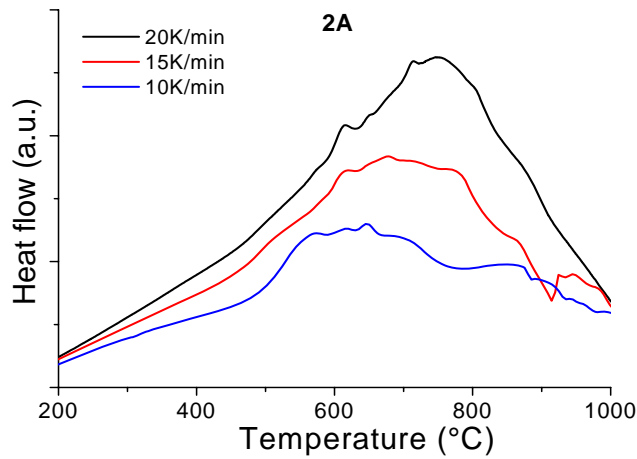


Figure 2.17: DSC scans for *2a* as-cast sample recorded at heating rates between 10 and 20 K/min

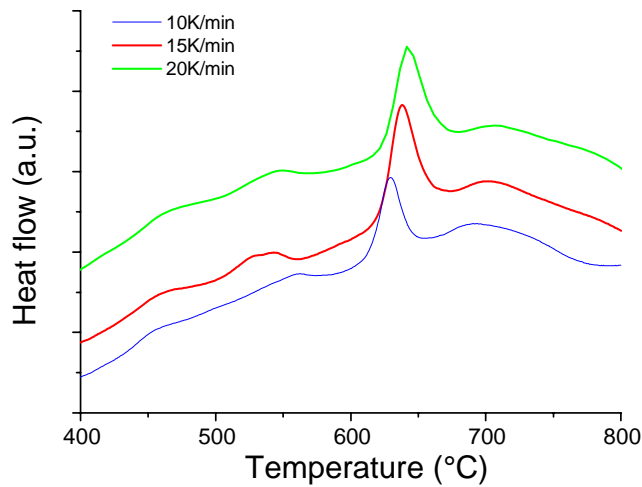


Figure 2.18: DSC scans for *1b* as-cast sample recorded at heating rates between 10 and 20 K/min

Figure 2.18 exhibits the DSC scans for the *1b* sample recorded at selected heating rates: 10, 15 and 20 K/min, respectively. For the clarity we have chosen to depict the DSC curves for only three heating rates. Contrary to the case of *1a* and *2a* samples, the *1b* sample presents a well-defined exothermic peak at a temperature of around 620°C. The DSC curves exhibit a similar peak for all the heating rates, between 5 K/min and 50 k/min. This kind of exothermic peak is characteristic for amorphous ribbons that undergo crystallization processes during annealing. This peak, which for the heating rate of 10K/min is situated at around 620°C, is related to the further crystallization process of the disordered microstructure of the as-cast state.

It has to be mentioned that the disorder-order FePt phase transformation that results in the formation of tetragonal $L1_0$ FePt occurs at about 560°C [2,4,26] (depending upon the Fe:Pt relative atomic ratio).

In the FePtNbB alloys, due to the presence of B and Nb, it may be presumed that this transformation could occur above this temperature. In the case of *1b* sample, even if this $A1 - L1_0$ structural phase transformation would occur, it will not be observed in the DSC due to the overlapping with the main exothermic peak associated with the crystallization processes. In addition, the situation is more complicated due to the high boron content. In Fe-Pt-B alloys with off-stoichiometric Fe/Pt composition ratio [69], it has been shown that during annealing, Pt exhibits strong affinity to Fe and forms the tetragonal phase. Then, the excess of Fe interacts with B and forms borides such as Fe_3B or Fe_2B .

The evolution of this exothermic peak has been investigated by taking several DSC scans of the as-cast *1b* sample with different heating rates, ranging from 5 to 50 K/min. Figure 2.19 shows the heating rate dependence of the crystallization temperature (T_{cryst}). We have observed already that T_{cryst} is shifted towards higher values as the heating rate is increased.

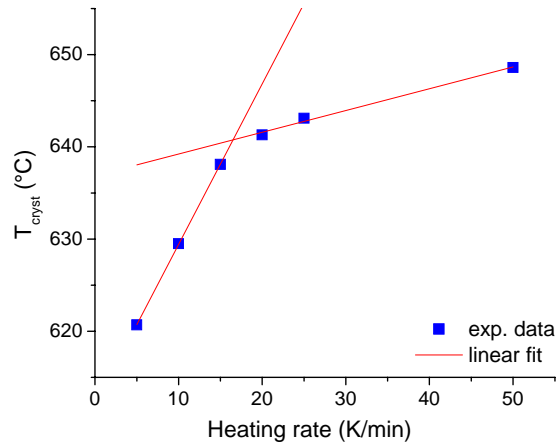


Figure 2.19: The crystallization temperature (T_{cryst}) vs. heating rate for as-cast amorphous $Fe_{68}Pt_{13}Nb_2B_{17}$ (sample *1b*)

As the heating rate is increased, T_{cryst} increases abruptly, up to a heating rate of 15K/min and, from 20K/min, the increase is much slower. It is probable that, at high

enough heating rates, the crystallization is no more dependent on the heating rate. The data may be fitted with two linear dependences, as it can be seen on Figure 2.19 (red curves). The abrupt increase of the T_{cryst} up to 15K/min is well fitted with a line with slope $a = 1.74$ while the slower increase from 20K/min up to 50K/min is well described with a line with slope $a = 0.23$. This two-slope linear behavior has been encountered in crystallization kinetics studies of Finemet-type ribbons [70]. Le Breton et al. [70] have found that the crystallized fraction follows a two linear dependence, with an abrupt increase followed by a slower increase with the heating rate. They have interpreted the first regime as corresponding to a middle crystallization stage governed by a 3D nucleation and growth process and the second regime as corresponding to the final crystallization stage where both nucleation and growth processes are strongly reduced.

The evolution of the T_{cryst} with the heating rate offers important information about the set of annealing parameters that have to be used in the following for treating the amorphous-like alloys in order to obtain a microstructure made of hard and soft magnetic nanograins suitably dispersed within the alloy. Analysis of figures 2.18 and 2.19 shows that the same crystallized fraction may be obtained for two sets of heating rate / annealing temperature. For example: the set of 10 K/min – 629°C provides in principle the same crystallized fraction as 15 K/min – 638°C. Nevertheless, as it has been documented in various reports on crystallization of amorphous alloys, smaller heating rates and lower annealing temperatures would provide a much more refined grain structure, with lower grain sizes, at the same crystallized fraction than heating at higher annealing rates.

The attribution of the observed exothermic peak to a certain transformation, crystallization and/or disorder-order phase transition, may be facilitated if one calculates the activation energy of the processes that produce this exothermic peak. By definition, the activation energy is the energy that needs to be overcome so that the transformation can occur and is different for endo or exothermic processes. Its determination can be done by using the so-called Kissinger plot analysis [71]. The activation energy needed for the crystallization process is received by the sample during annealing. On the other hand, if the exothermic process is due to another transformation such as the disorder-order fcc-to-fct $A1 - L1_0$ structural phase transition, the activation energy is expected to be much

lower, because both the initial (fcc) and the final (fct) states of this transformation are more ordered therefore of lower energy than the amorphous-like as-cast state.

The activation energy E_a of a certain transformation signaled as an exothermic peak in the DSC curve can be determined from the equation:

$$\ln\left(\frac{T_M^2}{\beta}\right) = \frac{E_a}{k_B T_M}$$

where k_B is Boltzmann constant, T_M is the temperature of the transformation peak, β - heating rate and E_a - activation energy.

For the determination of the activation energy it is mandatory to estimate T_M for the same sample at minimum three different heating rates. If one depicts $\ln(T_M^2/\beta)$ versus $1/T_M$ (Figure 2.20) the slope of this dependence will be E_a/k_B . In this way we can determine the activation energy. The activation energy has been determined by linear fitting of the dependence and the calculations yield $E_a = 5.01$ eV or 493 kJ/mol.

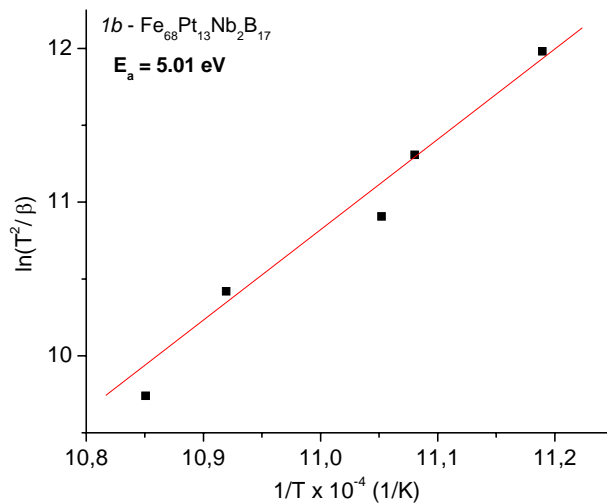


Figure 2.20: $\ln(T^2/\beta)$ vs. $1/T$ plot. The points are experimental values while the red line is the linear fitting.

Lyubina et al. [72] have reported that on nanocrystalline FePt powders the activation energy of the $A1 - L1_0$ transformation is between 1.04 eV and 1.45 eV. In FePt thin films, [73] the activation energy of the $A1 - L1_0$ transformation is slightly higher, being 1.7 eV. This value is clearly lower than what we found in the *1b* sample. On the other hand, in a number of articles [71,74-78] the crystallization processes of Fe-rich amorphous-like alloys were studied and the activation energy of crystallization was found to be in a wide range between 3.67 eV (362 kJ/mol) for Fe-B-Zr-Cu [75] and 7.61 eV

(750 kJ/mol) for Fe-Nb-B [78] depending upon actual composition of alloys. The value we find is clearly within this range. We infer that this peak corresponds to the further crystallization and grain growth of the fcc disordered nanocrystals already formed in the as-cast state. This is confirmed by the Mössbauer analysis of annealed *Ib* samples that is presented in detail in section 3.1. We have observed that while the *Ib* sample annealed at 500°C (before the exothermic peak) for 20 minutes shows an important relative fraction of amorphous-like environment of Fe sites, the *Ib* sample annealed at 700°C (after the exothermic peak) for 20 minutes shows only crystalline behavior. Therefore, the exothermic peak observed in the DSC curves corresponds to the crystallization processes as we have previously explained in the text.

- Pt-rich batch

The calorimetry measurements on the Pt-rich batch of samples have been done using the DSC 204 F1 Phoenix NETZSCH differential calorimeter at the National Institute for Materials Physics, Bucharest. Contrary to the DSC curves from the Fe-rich batch, in this case the maximum temperature was only 650°C. Therefore, eventual phase transformation occurring above this temperature could not be monitored. The calorimetry scans of the FePt – 1 and FePt – 2 samples were taken at a constant heating rate of 5 K/min. The DSC scans are presented in Figure 2.21.

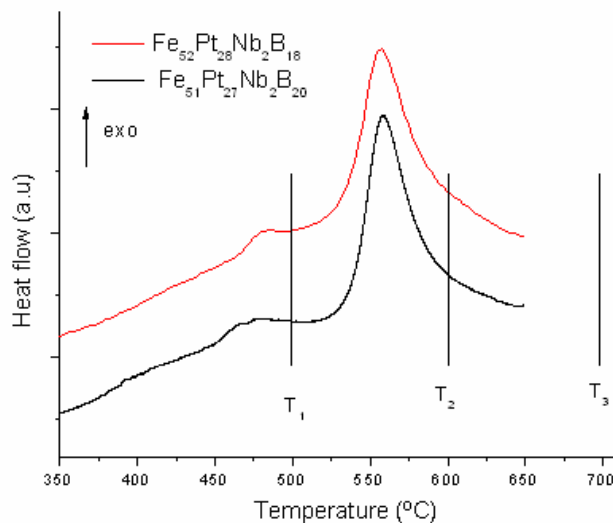


Figure 2.21: DSC scans taken for the FePt – 1 and FePt – 2 samples at 5K/min heating rate. The vertical bars at T₁, T₂ and T₃ temperatures represent the annealing temperatures (see Chapter 3).

As expected, judging from the results obtained so far on the two Pt-rich samples, the DSC curves are highly similar to each other. As both XRD and Mössbauer spectra

were quite similar it was expected that also DSC would show similar features. We have seen earlier that in spite of the presence of well-defined $A1$ Bragg lines, the Mössbauer spectra of the two samples show features typical for amorphous-like metallic alloys and we have assumed that the phase present in the as-cast state, in both samples is a disordered amorphous-like solid solution of $A1$ fcc symmetry with atoms arranged in a cubic lattice but highly disordered Fe chemical environment. This assumption is now confirmed by the DSC curves, where a well-formed, large and highly intense exothermic peak is observed, similar to the case of the $1b$ sample, and the disordered as-cast state has been proven for both Pt-rich samples. This peak may correspond, as described earlier, to the crystallization processes and to the $A1 - L1_0$ structural phase transformation. The maximum of the main exothermic peak is situated at 559°C for the FePt – 2 sample and at 557°C for the FePt – 1 sample respectively. As it can be seen, only 2°C separates the two main exothermic peaks. This is explained by the fact that also the initial compositions are highly similar, FePt – 2 sample having 2 at% boron more than the FePt – 1 sample. Below the crystallization exothermic peak, some pre-peaks are also visible at around 465°C and 477°C for the FePt – 2 and 479°C for the FePt – 1 sample respectively. This kind of pre-peaks of an exothermic nature have been found in other DSC studies of crystallization of amorphous metallic ribbons and have been interpreted as being due to the relaxation of the stresses induced in the ribbons during preparation [79]. The most promising feature revealed by the DSC scans in the case of the Pt-rich samples is the fact that the temperatures of exothermic peak are lowered with about 83 K comparing to the amorphous-like $1b$ sample. This means that eventually the desired hard-soft microstructure may be achieved at lower annealing temperatures and thus smaller grain sizes may be obtained which is also an important factor for an exchange spring behavior.

Densitometry measurements

We have estimated also the density of the as-cast ribbons. These measurements have not been performed up to now, being reported here for the first time for such alloys, but these values are needed for the calculations of magnetic parameters such as specific magnetization and magnetic moment.

The method we have used is the gas pycnometer. These measurements were made at Laboratoire des Oxydes et Fluorures (LdOF), Université du Maine, Le Mans. Gas

pycnometer is used to determine the true volume and true density of powders and bulk solids. The true volume of a solid is calculated from the measured drop in pressure when a known amount of gas is allowed to expand into a chamber containing the sample. Helium is the preferred gas, because it exhibits ideal gas behavior. It has the unique ability to fill the smallest pores on the surface of solid samples therefore it provides the best measurement of its volume [80]. As our ribbons have a certain degree of rugosity, the use of He gas is the best choice since it fills completely the irregularities on the ribbons surfaces. The true density is obtained by dividing the mass of the sample by the volume of the sample obtained. The simplest type of gas pycnometer essentially consists of two chambers, first one with a removable gas-tight lid to hold the sample and a second chamber of fixed, known internal volume - referred to as the reference volume or added volume. The facility is dotted with a pressure-measuring device - usually a transducer - connected to the first chamber. 3 valves are mounted: one valve for gas admission into the first chamber, a second one into the pathway connecting the two chambers, and a vent valve from the second chamber for gas evacuation. Several determinations are taken and an average of the obtained volume is performed in order to minimize the errors. All the values obtained for the density of our ribbons are plotted in Table VI. These values were used in order to calculate the magnetic polarization $J = \mu_0 M$ from the values of magnetic moments obtained during measurements.

Table VI: The density obtained for the as-cast alloys and their denomination

Chemical composition (at.%)	Sample denomination	Density (g/cm³)
Fe ₆₈ Pt ₂₁ Nb ₂ B ₉	1a	11.54 ± 0.27
Fe ₆₈ Pt ₁₃ Nb ₂ B ₁₇	1b	10.77 ± 0.24
Fe ₆₅ Pt ₂₅ Nb ₂ B ₈	2a	12.26 ± 0.32
Fe ₅₂ Pt ₂₈ Nb ₂ B ₁₈	FePt -1	11.61 ± 0.31
Fe ₅₁ Pt ₂₇ Nb ₂ B ₂₀	FePt -2	12.02 ± 0.28

It can be seen that all the density values are in a narrow interval of only 1.5 g/cm³. This proves the reliability of the chosen synthesis method in producing highly homogeneous melt spun ribbons.

In conclusion, the structural and magnetic characterizations of both batches of Fe-Pt-Nb-B samples have been thoroughly performed. From the Fe-rich batch, the *1a* and *2a* samples have been shown to be already crystalline in the as-cast state. The microstructure

is not susceptible to evolve in the sense of refining the grain sizes, since in the as-cast state, their grain sizes are above 30 nm already. The hard magnetic $L1_0$ phase in these two samples would be difficult to obtain by simple annealing. The *1a* sample also has a significant paramagnetic fraction at 300K, as documented by the central component observed in the Mössbauer spectra, related to disordered fcc A1 FePt phase. In the *1b* sample, as it was pointed out previously, the as-cast state is disordered, and it may serve as a precursor for formation of both hard and soft magnetic phase upon annealing. The Pt-rich batch of samples FePt – 1 and FePt – 2 is also promising due to the fact that they are documented to be also disordered in the as-cast state, their temperature of crystallization is lower than the one for 1b sample. In these samples, it looks more likely to produce, by appropriate annealing, a microstructure formed by exchange coupled hard and soft nanocrystalline grains, with controlled sizes, as needed for an exchange spring magnet.

Table VII summarizes the properties of the as-cast state for the samples investigated:

Table VII: Structural and magnetic state of the as-cast samples and their measured chemical composition

Samples	Nominal composition (at%)	Structural state and mean grain size	Magnetic state at 300K	Chemical true composition (at%)
1a	Fe ₆₈ Pt ₂₁ Nb ₂ B ₉	A1 FePt fcc crystalline 38 nm	Soft magnetic	Fe _{67.6} Pt _{21.4} Nb ₂ B ₈
2a	Fe ₆₈ Pt ₁₃ Nb ₂ B ₁₇	A1 FePt fcc crystalline 60 nm	Soft magnetic	Fe _{67.5} Pt _{13.5} Nb ₂ B ₁₇
1b	Fe ₆₅ Pt ₂₅ Nb ₂ B ₈	Disordered A1 fcc 3 nm	Soft magnetic	Fe _{64.4} Pt _{25.6} Nb ₂ B ₈
FePt – 1	Fe ₅₂ Pt ₂₈ Nb ₂ B ₁₈	Disordered A1 fcc 11 nm	Soft magnetic	Fe _{51.4} Pt _{28.6} Nb ₂ B ₁₈
FePt – 2	Fe ₅₁ Pt ₂₇ Nb ₂ B ₂₀	Disordered A1 fcc 7 nm	Soft magnetic	Fe _{50.7} Pt _{27.3} Nb ₂ B ₂₀

2.5 Formation and evolution of nanocrystalline magnetic phases in Fe-Pt-Nb-B: *in situ* temperature-dependent synchrotron XRD study

In order to determine the structural properties and their temperature dependence of the ribbons, the ideal way would be to take “pictures” of the structure at given temperatures by using *in situ* synchrotron X-ray diffraction for which the data recording is quite instantaneous compared to that observed by other techniques.

In the following, it is described the formation and evolution of nanostructured phases by means of energy-dispersive *in situ* X ray diffraction using the synchrotron radiation at DESY HASYLAB Hamburg. F2.1 MAX80 at Hasylab is a dedicated beamline with high-temperature / high-pressure energy-dispersive X-ray diffractometer using a multi-anvil type X-ray (MAX) system.

The synchrotron radiation is an electromagnetic radiation generated by the acceleration of charged particles through magnetic fields. This may be achieved naturally by fast electrons moving through magnetic fields in space, or artificially by accelerating electrons into storage rings in a synchrotron. Electrons are accelerated to high velocities in several stages to achieve a final energy that is typically in the GeV range. The electrons are stored in an ultra-high-vacuum ring on a closed loop and thus circle the ring a vast number of times. The electrons are forced to travel in the closed loop and are deflected from their trajectory by strong magnetic fields. Due to the deflection (change of direction) the electrons emit high brilliance and high-intensity electromagnetic radiation with wide energy spectrum at GeV frequencies. This radiation has been named synchrotron radiation.

2.5.1. Characteristics of synchrotron radiation and schematics of synchrotron X-ray diffraction experiments

Synchrotron radiation has a number of unique properties:

- High brightness: synchrotron radiation is extremely intense (10^5 times higher than conventional X-ray tubes) and highly collimated,
- High brilliance: 3rd generation sources typically have a brilliance larger than 10^{18} photons/s/mm²,
- Highly collimated, i.e. small angular divergence of the beam,

- Wide energy spectrum: synchrotron radiation is emitted with a wide range of energies, allowing beams of any energy to be produced,
- Highly polarized
- Emitted in very short pulses, typically less than a nano-second.

On the experimental bench at the beamline, it is mounted the MAX80 (MultiAnvil Type X-Ray System) as it can be seen in Figure 2.22. This is a multi-anvil pressure apparatus with six tungsten carbide anvils compressing a cubic sample volume of the order of 0.5 cm^3 . Pressure is generated by a 250-tons hydraulic ram and measured by adding an internal pressure marker with known P-V-T data to the sample. The maximum temperature of approx. 2000K is produced by an internal graphite heater and controlled by thermocouples. The attainable pressure is mainly determined by the edge length of the anvil planes. With this ram, pressures of approximately 7GPa for an anvil with 6 mm edge length and approx. 12 GPa for an anvil with 4 mm edge length, are obtained. The high-pressure cell is a cube made of mixture of boron and epoxy resin containing the cylindrical sample. The sample volume can be loaded according to the demand of the experiment. Usually, samples of volume between 20 mm^3 and 50 mm^3 can be loaded into the cube.

The set-up for energy-dispersive X-ray diffraction is as follows. The synchrotron beam is guided between the tungsten anvils through the sample. A Ge-solid state detector analyses the diffracted beam at a fixed angle. The maximum available 2-theta range is 30° . The MAX80 can be adjusted in 3 directions: vertical, rotation and horizontal movement, perpendicular to the synchrotron beam with 10 microns accuracy. The diffractometer is linked with the high-pressure apparatus and has 5 degrees of movement:

- rotation around the vertical axis of the sample,
- horizontal translation perpendicular to the beam,
- vertical translation,
- 2-theta and,
- rotation of the detector.

The primary beam size and the diffracted beam size are controlled by stepped-motor driven crossed-slit systems.

The primary beam is provided by a gold-coated toroidal focusing mirror placed in front of a double crystal monochromator. The intensity of primary beam is monitored by a gas ionisation chamber and reaches 10^9 photons/s in focused beam mode.

An angle-dispersive powder diffraction system was installed at the MAX80 beamline additionally to the existing energy-dispersive system, in order to reach better resolution and to allow structure refinements under *in situ* conditions. For generating monochromatic X-ray, a double crystal, fixed offset monochromator was built. The monochromator is capable of generating wavelengths in the range of 0.3 up to 10Å.

The scattered synchrotron radiation is detected using a high purity Ge solid state detector placed in front of a NaI scintillation counter. The energy range covered by the detector is between 2 and 80 keV.

For the temperature-dependent XRD experiment, we have prepared cube samples, as is described in Figure 2.23. The sample is mounted inside of a boron cube holder of 0.8 cm. Inside the cube are mounted concentrically graphite (for heat transport) and boron nitride (BN) cylinders. BN powder is also mounted together with the sample, for purpose of insulation.

Energy calibration is done using pure NaCl powder mounted inside the cube. Heating and temperature control are achieved by a PtRh thermocouple placed also inside the cube. The sample was heated in steps of 25°C (heating rate 5K/min) between 20°C and 1000°C and quenched down to RT in higher steps. Diffraction patterns are recorded using a radiation wavelength $\lambda = 1.2 \text{ \AA}$.

The exposure time was 2 minutes for each diagram and after recording the diagrams, the temperature was immediately raised to the next step. Then the temperature is raised again in steps of 25°C and XRD diagrams are taken in a dynamic way. The short time annealing does not allow complete crystallization of the sample. For this reason, the process is called “dynamic annealing”.

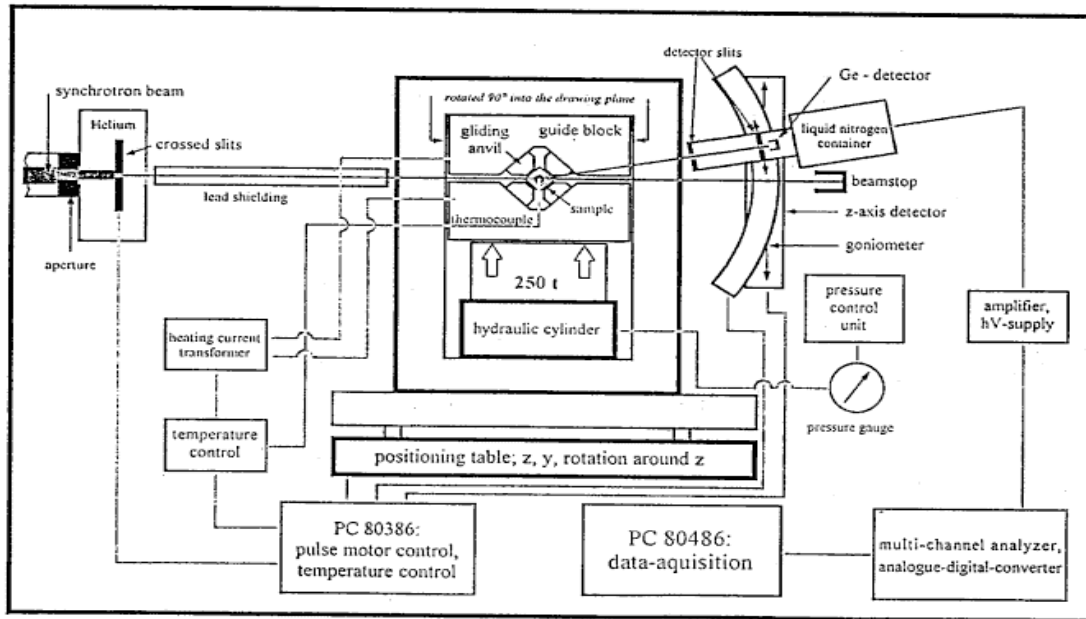


Figure 2.22: Schematics of the energy-dispersive synchrotron X-ray diffraction experiment with multi-anvil system for high-pressure / high-temperature measurements

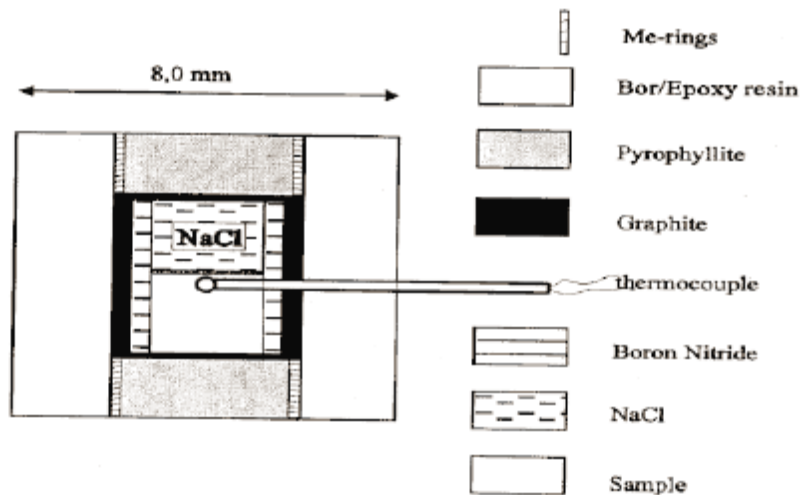


Figure 2.23: Sample holder mounting for the X-ray diffraction experiment described in Figure 2.22

2.5.2. Temperature- and pressure-driven phase evolution in Fe-Pt-Nb-B

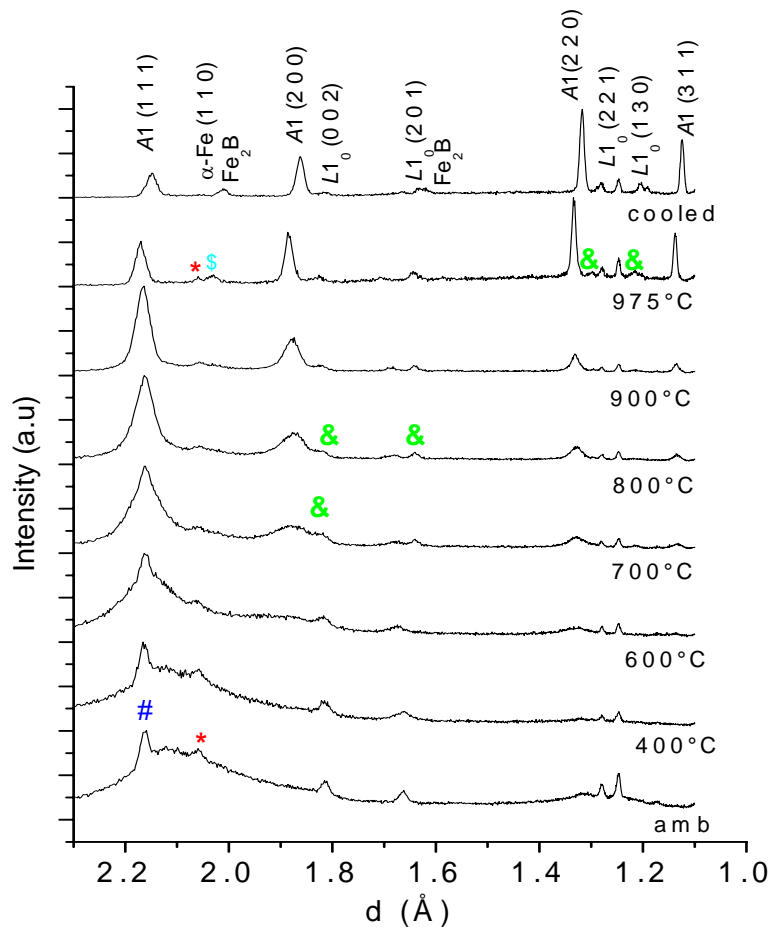


Figure 2.24: X-ray diffraction spectra taken at selected temperatures for the $\text{Fe}_{68}\text{Pt}_{13}\text{Nb}_2\text{B}_{17}$ alloy (*Ib* sample). # - A1 FePt, * - α -Fe, & - L1_0 FePt, \$ - Fe_2B

The energy-dispersive XRD spectra for $\text{Fe}_{68}\text{Pt}_{13}\text{Nb}_2\text{B}_{17}$ alloy at selected temperatures are plotted in Figure 2.24 as a function of the reticular distances d . We have measured the ambient temperature XRD spectrum of NaCl and its main Bragg peak serves as energy calibration and the reticular distances at which Bragg lines are observed in the spectra may be accurately derived.

At ambient temperature the sample is structurally disordered, as we have seen also in the as-cast XRD results, with a very broad line centered at around 2.1 Å. Some small peaks on top of this broad line, indexed as belonging to bcc α -Fe and A1 FePt incipient formation of very small crystals are observed. Other peaks observed in the sample at

ambient temperature and not indexed in Figure 2.24 are due to the other materials used to make the boron cube and fill the cylindrical hole, as mentioned in Figure 2.23.

When the temperature increases, the sample begins to crystallize and the width of the broad Bragg line decreases gradually.

Between 400°C - 600°C, together with the main Bragg reflections of α -Fe and *A1* FePt, some peaks of lesser intensity that may be attributed to the *L1₀* phase, such as (0 0 2), (2 0 1), (2 2 1) and (1 3 0) become visible. Nevertheless, these lines are not the most intense and the main superlattice peaks of *L1₀* phase, those belonging to the (0 0 1) and (1 1 0) reflections, are not observable.

From 400°C to 600°C, a gradual reduction of the bcc α -Fe main Bragg peak compared to the fcc *A1* FePt one occurs. This is accompanied by a continuous narrowing with temperature of the observed Bragg lines due to the gradual crystallization process.

From 600°C we observe a strong decrease of α -Fe and an increase of *A1* FePt relative proportion. We have also indexed some superlattice peaks that are specific only of tetragonal *L1₀* FePt phase (shown on the Figure by symbol &) but nevertheless, the main phase remains the fcc *A1* FePt phase.

Between 900°C - 975°C the peak intensities of tetragonal *L1₀* FePt phase diminish down to the limit of observation. Due to the increased disorder induced by the large thermal energy, the small amount of tetragonal *L1₀* phase formed at around 600°C undergoes reverse order-disorder phase transformation occurs and at 975°C the disordered cubic *A1* FePt phase predominates. This is in agreement with the DSC scans where an endothermic event is observed at around 900°C. Also, from 800°C the lines of tetragonal Fe₂B, with small intensity are indexed in the spectrum while α -Fe has disappeared completely.

Another interesting phenomenon occurring between 900°C and 975°C is the reduction of the most important *A1* FePt Bragg peak, the (1 1 1) and strong increase of (2 0 0), (2 2 0) and (3 1 1) *A1* FePt peaks. This may be attributed to a uniaxial lattice reorientation or expansion, driven by the extremely high temperatures. This latter phase transformation is irreversible as shown by the XRD spectrum taken after cooling the sample down to ambient temperature, spectrum which preserves almost the same features

as the 975°C one. Unindexed Bragg reflections are due to the method of loading the sample into the boron cube with other elements, as described above.

To summarize the effects of the dynamic annealing on the formation and stability of nanocrystalline magnetic phases that crystallize from the initial amorphous as-cast ribbons, there are several stages in the crystallization processes and microstructure evolution as follows:

- a) 400°C – 600°C: Amorphous + α -Fe + *A1* FePt (very small crystals) → Amorphous' + α -Fe + *A1* FePt + *L1₀* FePt in very small amount
- b) 600°C – 900°C: Strong decrease of α -Fe, increase of *A1* proportion and formation of tetragonal Fe₂B
- c) 900°C – 975°C: Vanishing of the *L1₀* FePt, uniaxial lattice expansion of *A1* FePt, strong decrease of α -Fe

We have fitted the XRD spectra with the Datlab software, described earlier. The line used for fitting was pseudo-Voigt profile. Peak position, linewidth, peak intensity and the mixing parameter are all free parameters during fitting and the program allows simultaneous fitting of all parameters for several peaks, without the need of constraints. It is possible to de-convolute complex Bragg reflections and highly reliable peak positions and intensities as well as FWHM values are obtained.

An example of deconvolution of very complex, broad Bragg lines is presented in the Figure 2.25. It represents the fitting of the broad Bragg line situated in the angular interval between 1.9 and 2.3 in units of reticular distance *d* or between 30 and 55 in energy units (keV) for the *1b* sample, spectrum recorded at 575°C. At this temperature the sample is still disordered. In this example, we have used two broad lines to fit respectively α -Fe (1 1 0) and *A1* FePt (1 1 1) Bragg reflections and four narrow pseudo-Voigt profiles to fit other lines observed in the spectrum. These other lines correspond to the boron nitride and graphite from the cube holder of the sample (see Fig. 2.23). As it can be seen, the experimental points are accurately fitted. In Figure 2.25, in black are the experimental points and the red line represents the fitting. From the fitting we have obtained the peak positions, their intensities and their linewidths, in order to correctly index each of the recorded spectra.

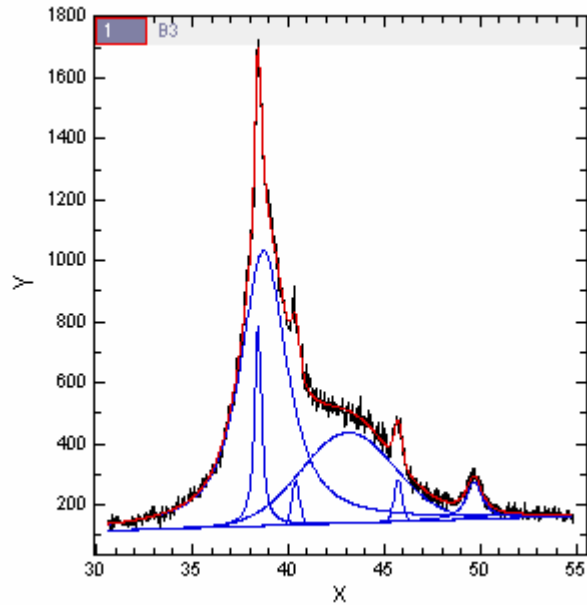


Figure 2.25: An example of deconvolution of a broad and complex Bragg line of the amorphous 1b sample recorded at 575°C. Black: experimental curve, red: the fitting with Datlab.

The gradual crystallization process observed *in situ* during the dynamic annealing may be observed also in Figure 2.26 which plots the full width at half maximum (FWHM) of the main Bragg peaks of α -Fe and FePt phases obtained from the spectra fitting as a function of the temperature at which each spectrum has been recorded.

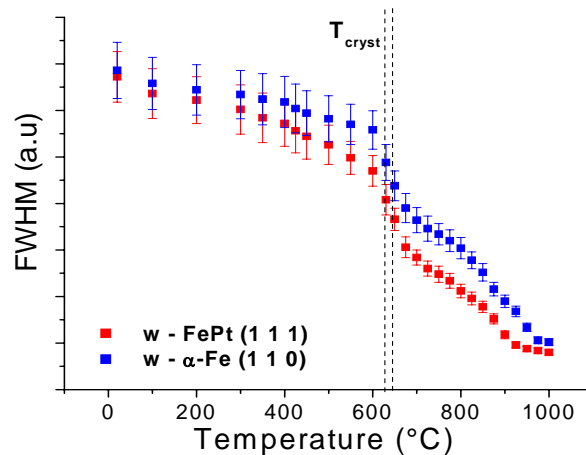


Figure 2.26: Evolution with the temperature of the Full-width-at-half-maximum (FWHM) for the mean Bragg reflections of the α -Fe and FePt crystalline phases. The error bars for the estimation of FWHM from the fit are provided. Errors for temperature estimation are about 10% between 0 and 150°C, and decrease down to 5% for higher temperatures, due to different heaters employed

It is established that the FWHM is inversely proportional with the average grain size. Therefore, it represents an indication about the variation of the size of the grains of both phases with the temperature of dynamic annealing. Both linewidths decrease smoothly with the temperature from the ambient temperature until 975°C.

The decrease is slow until about 630°C, meaning that a gradual crystallization process occurs in the sample. At 630°C, a sharp decrease of both α -Fe and FePt linewidth appears. This value is close to the exothermic peaks related to crystallization processes, observed in DSC. On Figure 2.26, the two vertical bars represents T_{cryst} as deduced from the DSC curves recorded at 10 and 20 K/min. Above this value, the grains continuously grow (the linewidth decreases constantly) until 975°C where the sample is completely crystallized and consequently the linewidth becomes narrow, as is the case for bulk samples.

In the following, we quantitatively describe the evolution with temperature of the relative amount of Fe compared to the relative amount of FePt phases. For this, we plot in Figure 2.27 the ratio between the relative intensity of the main Bragg peaks of α -Fe and of A1 FePt phase as obtained from the fitting, as a function of temperature. At ambient temperature, these relative abundances are almost equal, the ratio being almost equal to 1.

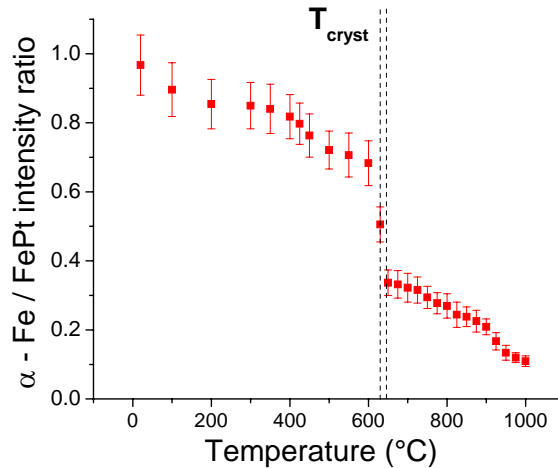


Figure 2.27: Relative intensities ratio between mean Bragg peaks of α -Fe and FePt phases vs. temperature. The error bars are provided. The two vertical bars represents T_{cryst} as deduced from the DSC curves recorded at 10 and 20 K/min

With increasing the temperature, we observe a gradual decrease of α -Fe comparing to the FePt up to 620°C. At this temperature there is a sudden drop of the α -

Fe/FePt ratio (near the DSC exothermic peak). This sharp decrease is similar with the one observed in Figure 2.26. It seems that the crystallization of the sample is followed by an increase of the relative amount of FePt nanograins in the detriment of the α -Fe content.

Above 620°C, α -Fe relative intensity continues to decrease and at 975°C its relative amount is only 12% of the FePt relative amount. In the temperature range covered by the exothermic peak observed in the DSC scans, between 600°C and 670°C, some of the FePt grains may be formed directly into their tetragonal ordered state. Also, some of the excess Fe contributes to the growth of FePt nanograins, thus leading to the observed drastic decrease of the relative content of α -Fe. The formation of α -Fe was not observed upon classic annealing. This apparent discrepancy is explained by the fact that the beam in the synchrotron XRD is extremely narrow and may obtain local information from areas with possible inhomogeneities in the composition.

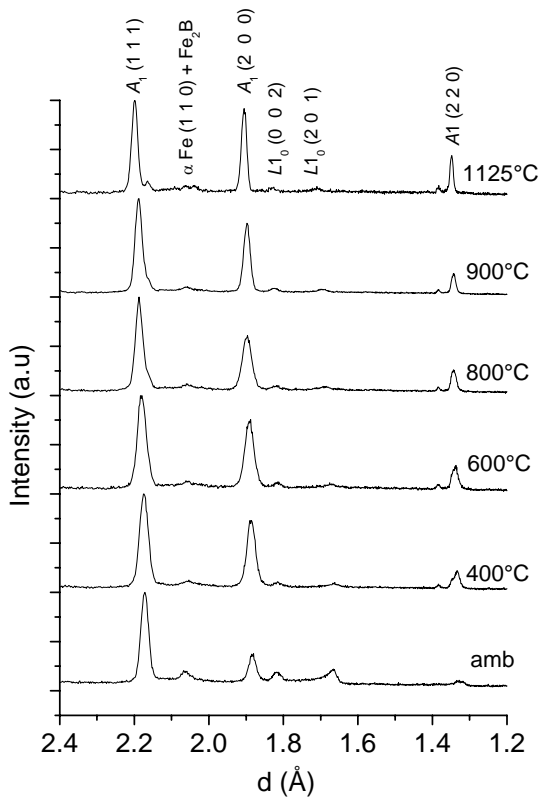


Figure 2.28: Selected XRD spectra recorded at various temperatures in $\text{Fe}_{65}\text{Pt}_{25}\text{Nb}_2\text{B}_8$ (2a) sample

In the following synchrotron XRD study we were interested to see if by annealing or by applying a small pressure, we are capable to induce disorder-order $A1$ to $L1_0$ phase transformation in the already crystalline samples.

For this purpose, we have performed a similar synchrotron XRD experiment as in the case of $1b$ sample, this time with the $2a$ sample. We recorded XRD spectra for 2 minutes exposure at temperatures between ambient and 1125°C in 25°C steps, in order to observe the evolution with temperature of the crystal structure of the sample.

Selected XRD spectra recorded at various temperatures are presented in Figure 2.28.

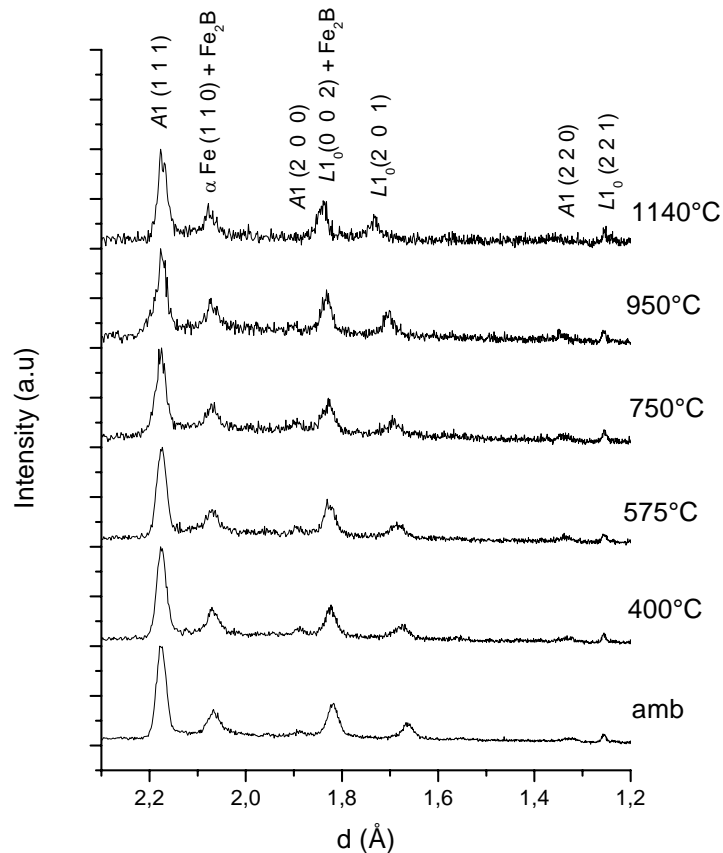


Figure 2.29: Selected XRD spectra recorded at various temperatures with an applied pressure of 1.4 GPa in $\text{Fe}_{65}\text{Pt}_{25}\text{Nb}_2\text{B}_8$ ($2a$) sample

We have then performed a similar experiment with applying a pressure of 1.4 GPa onto the hydraulic ram that encompasses the tungsten carbide anvils that held the cube sample. We recorded XRD spectra from ambient temperature up to 1140°C . A selection

from the obtained XRD spectra at various temperatures is presented in Figure 2.29. The indexation of Bragg reflections allows the identification of the crystalline phases occurring in the sample. A similar fitting procedure, as the one described for the *Ib* sample spectra was used also in these experiments.

In figure 2.28, at 20°C, a mixture of fcc *A1* and fct *L1₀* FePt phases is observed, together with small amounts of bcc α -Fe. To distinguish between *A1* and *L1₀* FePt phases is extremely difficult due to strong overlapping of main Bragg reflections. Nevertheless two superlattice Bragg peaks, that are specific only to the tetragonal phase, such as *L1₀* (0 0 2) and *L1₀* (2 0 1) peaks could be unambiguously observed and indexed. As in the case of the *Ib* sample synchrotron XRD study, the main superlattice peaks of the *L1₀* FePt, the (0 0 1) and (1 1 0) peaks are missing. The presence of some peaks belonging to the *L1₀* tetragonal phase may be explained by the fact that the diffraction of synchrotron radiation is highly local in that case. As the narrow synchrotron beam may hit inhomogeneities and locally small crystals of *L1₀* phase may be formed, facilitated by the high energy of the incident synchrotron beam. The lattice parameters for the FePt phases at 20°C are:

- $a = 3.7868 \pm 0.0041 \text{ \AA}$ and $c = 3.6467 \pm 0.0056 \text{ \AA}$ for *L1₀* phase
- $a = 3.7673 \pm 0.0019 \text{ \AA}$ for *A1* phase

These values are slightly different from the ones of the bulk counterparts, this being explained by the boron addition in the alloy. The atoms may randomly accommodate, due to the rapid solidification process, the Fe and Pt sites in the cubic and tetragonal FePt phases, modifying the lattice parameters.

With increasing temperature, the inhomogeneities from preparation tend to disappear and, consequently, the two small lines belonging to the superlattice Bragg peaks of *L1₀* phase diminish. They are though still observed in the spectra up to the highest temperature investigated (1125°C) but in very small proportion. Anyway, the main phase is the cubic *A1* phase for the whole temperature range investigated. The synchrotron XRD results differ from the room temperature powder X-ray diffraction results, already presented. As explained earlier, the synchrotron beam only hit a micron-sized region of the sample, whilst in the classic XRD experiments, the Bragg reflections are recorded from an investigated area of more than 1 cm². This explains the fact that in

the classic XRD diagram, the $L1_0$ phase is not visible. Also, the Mössbauer spectroscopy did not reveal the presence of the $L1_0$ phase.

Starting with around 800°C also iron boride Fe_2B phase is formed, in very small percentage, probably by segregation of the boron atoms from the interfacial regions between FePt grains. This phase has been observed to also occur at around 800°C in the *Ib* sample temperature-dependent synchrotron study.

The phase evolution with temperature is quite different if we apply pressure (1.4 GPa) to the sample (Figure 2.29). One observes at 20°C the drastic decrease of $A1$ (2 0 0) and $A1$ (2 2 0) reflections, compared to Figure 2.22, and increase of the superlattice $L1_0$ (0 0 2), $L1_0$ (2 0 1) and also $L1_0$ (2 2 1) Bragg reflections. The vanishing of the (2 0 0) and (2 2 0) lines of the cubic $A1$ phase provides evidence of a uniaxial cubic lattice expansion due to applied pressure. The main superlattice peaks of the $L1_0$ FePt, (0 0 1) and (1 1 0), that give the specificity of the $L1_0$ phase are still missing.

The Bragg reflections of the $L1_0$ phase are observed at the same relative intensity for the whole temperature range investigated. This proves that the volume fraction of tetragonal $L1_0$ FePt is larger compared to the case of Figure 2.29 where we did not apply pressure. Here, the hard magnetic $L1_0$ tetragonal phase co-exists with soft magnetic phases (cubic $A1$ FePt, α -Fe and Fe_2B) on a wide range of temperatures. This is particularly important for the use of such exchange coupled nanocomposite magnets in extreme conditions (such as high temperature and so on).

It seems that the disorder-order FePt $A1$ - $L1_0$ phase transformation can be partially stimulated by the applied pressure. It is found that at 1140°C the relative proportion of the tetragonal FePt, as obtained from numerical fitting of the XRD spectrum, is about 11% while the cumulated volumetric fraction of the soft phases is about 89%. Nevertheless, the very small amount of $L1_0$ makes this sample not suitable for magnetic applications.

But these results were not confirmed by magnetic measurements, where no coercivity was found for any annealing treatment in the *2a* sample. The discrepancies between synchrotron and classic XRD experiments explain in some extent the differences observed in the interpretation of the spectra.

In the synchrotron study, the X-ray beam is extremely narrow and highly intense: when hitting a micron-size area of the sample it is capable to observe small features such

as incipient $L1_0$ crystallites locally formed. Due to its high energy the beam may actually be capable to produce local heating and to promote thus by itself the disorder-order phase transformation on very small areas of the sample.

In the classic XRD experiment, the beam is several orders of magnitude less bright and less intense, and it provides information from a much wider area of the sample, therefore, the structural information is averaged over a much larger sample volume and only the main crystal phases may be observed.

By applying pressure we have nevertheless showed the possibility of preserving the coexistence of hard and soft magnetic phases, until very high temperatures. As an example, in the case of *1b* sample, starting with 900°C due to the reversed phase transformation any trace of $L1_0$ has already disappeared.

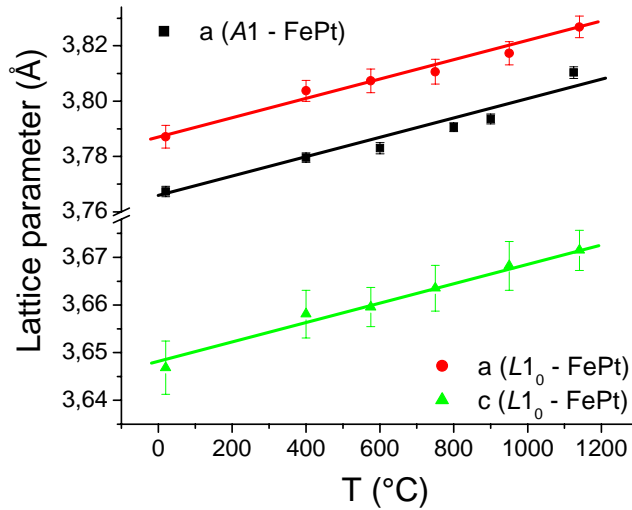


Figure 2.30: The evolution with temperature of the lattice parameters for the cubic $A1$ and tetragonal $L1_0$ phases in $\text{Fe}_{65}\text{Pt}_{25}\text{Nb}_2\text{B}_8$ ($2a$) sample. The error bars are provided.

The evolution with temperature of the lattice parameters for the $A1$ and $L1_0$ phases is plotted in Figure 2.24. The parameters were obtained by least-square fitting of the Bragg reflections angular position, expressed in reticular distances d . The lattice parameters of the tetragonal phase as well as of the cubic phase follow the same evolution. The parameters of both phases increase continuously and linearly with increasing the temperature. This result is an expected one, being due to the expansion of the unit cell volume due to continuous annealing. The estimated errors are very small for the lattice parameter of the $A1$ cubic phase and much larger for the case of the lattice

parameters of the tetragonal $L1_0$ phase. This is due to the fact that only less intense $L1_0$ Bragg peaks are unambiguously indexed in the spectra, therefore, the errors are higher than in the case of the cubic lattice.

We have observed that the disorder-order FePt phase transformation may be partially stimulated by the application of a small pressure on the sample. Such a feature results in the coexistence of hard magnetic FePt phase with soft magnetic ones, over a large temperature range, in an alloy with low Pt content, and this is particularly important for the stability of such magnets in high temperature technological applications. Following the dynamic annealing, with or without applying pressure, the microstructure is stable at room temperature, as we have observed that the XRD spectra taken upon cooling down the samples from the highest temperature achieved during the experiments preserves the same features as the highest temperature spectra.

Chapter 3.

Structural characterization of annealed Fe-Pt-Nb-B ribbons.

3.1. Isothermal annealing and phase structure of Fe-rich ribbons

By isothermal annealing of the as-cast alloys we expect to obtain a microstructure made of nanocrystalline grains of refined sizes and later to obtain, by various characterization techniques, information regarding the nature and crystal symmetry of the multiple phases formed, in various stages of crystallization, and the magnetic behaviour of these samples, in view of the scope of the present work.

A first step towards the study of the microstructure obtained by annealing was done with the *in situ* temperature-dependent synchrotron XRD experiments, largely described in the previous Chapter. Nevertheless, as the study was done in dynamic annealing, the microstructure obtained was not yet completely formed. For temperatures well above the T_{cryst} in the *Ib* sample, the metastable precursor was not completely crystallized as witnessed by the large linewidth of Bragg peaks. This is the reason for which we need to perform static annealing on these samples.

The static annealing would allow the microstructure to form and to stabilize. By careful investigation of the crystallization products of these annealed samples, both the structural and magnetic properties may be obtained. These properties, correlated with results of thermal analysis, may provide valuable information on how to obtain co-existence of hard and soft phases with exchange coupled grains of a reasonably low size, a necessary condition for creation of an exchange spring magnet.

The annealing temperatures were carefully chosen as to be correlated with the exo- and endothermic effect, observed in the thermal analysis. As we already mention, an event where heat is exchanged by the system with the exterior, is directly related with structural modifications in the sample, structural and/or magnetic phase transitions, crystallization and many others. Therefore, it is important to identify these changes, by observing the microstructure at various stages of annealing, and most important, to track the possibility of the occurrence of the $L1_0$ phase, necessary for the exchange spring magnets.

The temperatures of annealing were each chosen as to correspond to an exothermic event. We recall Figures 2.16 – 2.18 (previous chapter), the DSC curves where, the annealing temperatures – plotted as stars – were chosen as to correspond to the onset of a DSC event, and respectively to the end of it. By comparing the structural data of the samples annealed at these two temperatures, one may identify with high accuracy, to what exactly corresponds the DSC event. The annealings were performed in a furnace with controlled temperature and heating rate, under protective Ar atmosphere (10^{-1} mbar). By the detailed analysis of the exothermic peak of the *1b* sample (previous chapter), we were able to derive an optimum of the annealed conditions, and in order to obtain the microstructure with small grain sizes, we opted for a heating rate of 5K/min for all treatments. The annealing time was 30 minutes for *1a* and *2a* samples and 20 minutes for the *1b* sample.

3.1.1. Case of crystalline samples

As we have previously seen, the *1a* and *2a* as-cast alloys are completely crystallized, in a fcc A1 FePt lattice, with no occurrence of tetragonal $L1_0$ phase. Nevertheless, some small exothermic effects observed in the DSC curves has prompted us to perform annealing treatments in the vicinity of these effects in the search for eventual A1 – $L1_0$ structural phase transformation and formation of hard magnetic FePt phase. Four different annealings were performed in the range 600°C-900°C. In order to check the formation of the hard magnetic tetragonal phase, the first test was to perform the hysteresis measurements on the *1a* and *2a* annealed samples. Occurrence of coercivity in these samples would have been an indication of the eventual formation of the tetragonal phase.

Some authors [65] argued that in binary FePt alloys subjected to long time annealings at 600-800°C, the tetragonal phase, even if is formed, do not exhibit marked values of coercivity, mainly due to the non-stoichiometry of the binary FePt alloy and the high degree of disorder in the alloy.

In our samples, the coercivity increases very little upon annealing, but the values were still very low compared with that required for an exchange spring magnets. Maximum of the coercivity reached for the annealed *1a* and *2a* samples was 33 mT, an extremely small value, while the maximum magnetization was only half of the as-cast

value in both cases. This indicates without possible doubt that the tetragonal phase has not been formed after annealing in these samples. These results show that the static annealing performed on the *1a* and *2a* samples did not provide the desired formation of the hard magnetic FePt $L1_0$ phase in a proportion that would ensure good magnetic properties. The XRD results did not differ significantly from the as-cast ones and therefore they are not discussed here.

More interesting seems to be the amorphous-like samples where the microstructure and formation of hard magnetic phase may be better controlled by annealing.

3.1.2 Case of disordered sample

XRD analysis

In the case of *1b* sample the situation is rather different. As we have noticed in the structural data, due to the high boron content a metastable as-cast state for the *1b* sample has been obtained. In agreement with the DSC results (Figure 2.18) where we have seen that there are exothermic pre-peaks at about 520°C – 570°C and the main exothermic peak, associated with the crystallization occurs at 620°C -650°C depending on the heating rate, we have chosen as annealing temperatures the values: 500°C, 600°C, 700°C and 800°C and we have performed annealing treatments at these temperatures. The heating rate was established at 5 K/min and annealing time (time spent at maximum temperature) was set to 20 min. These annealings were made under high vacuum protection (10^{-4} mbar) in order to avoid oxidation.

The structure of the resulting samples was characterized by XRD, Mössbauer spectrometry and their magnetic properties by vibrating sample magnetometry and SQUID. The X-ray diagrams are plotted in Figure 3.1. The as-cast state reveals the broad Bragg peaks of the disordered $A1$ FePt-rich solid solution, as has been discussed in the previous chapter. At 500°C, the lines are narrower but no additional Bragg peaks are observed. The broad line centred at around 25° is due to the glass sample holder and the glue used to hold the ribbons during measurements, as we have argued in the previous Chapter. This broad feature is preserved at all annealing temperatures, until 800°C, where the intensity of the main Bragg peak is very high and the broad feature appears strongly

diminished due to scaling. At 500°C, the same A1 fcc broad line pattern is observed but line profiles are better formed with smaller linewidth than in the as-cast state.

At 600°C the main lines of the fcc Fe₃Pt phase are observed and the process of narrowing is furthermore continued, as expected. Starting with 600°C a small Bragg peak, attributed to the main Bragg reflection of the Fe₂B tetragonal phase is observed.

At 700°C the lines of the fcc phase are even narrower, same fcc Fe₃Pt and Fe₂B phases being indexed in the XRD diagram. The XRD diagram at 800°C is completely crystallized and the fcc Fe₃Pt and Fe₂B are the only phases visible in the diagram.

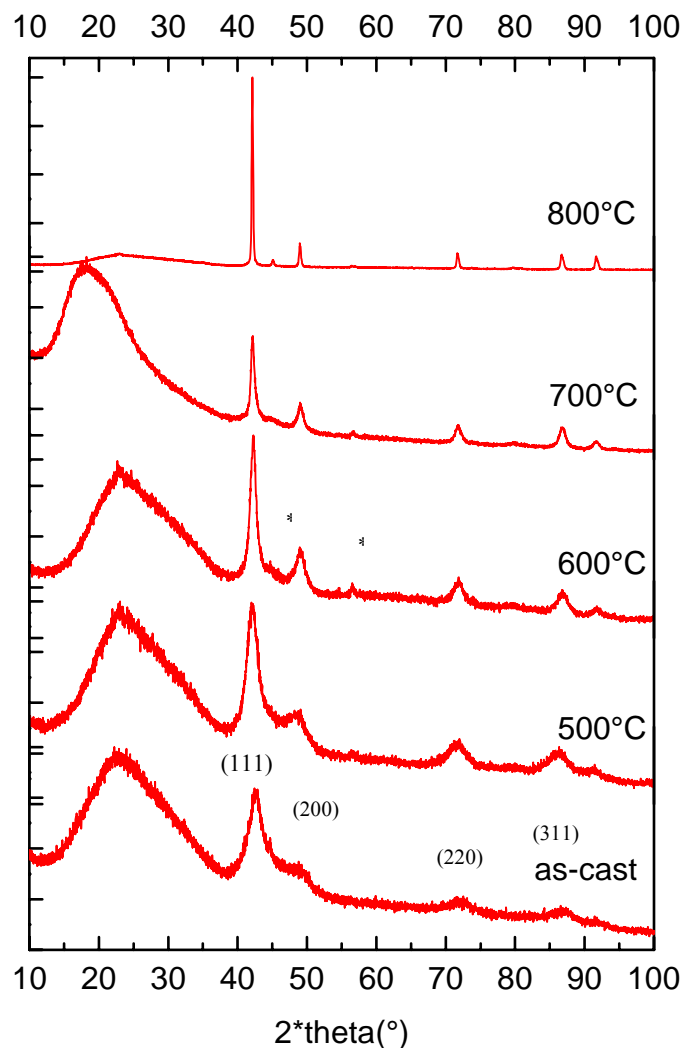


Figure 3.1: X-ray diagrams of as-cast and annealed at 20 min 1b samples. The annealing temperatures are mentioned on the graph. * - Fe₂B

Table VIII: The lattice parameters and the average grain sizes derived from the fit of the XRD spectra.

Sample	Annealing	fcc (Fe ₃ Pt)	Fe ₂ B		Grain size fcc (Fe ₃ Pt) (nm)	Grain size Fe ₂ B (nm)
		a (Å)	a (Å)	c (Å)		
Fe ₆₈ Pt ₁₃ Nb ₂ B ₁₇	As-cast	3.69			3 ± 1	
	500°C 20'	3.72			7 ± 2	
	600°C 20'	3.73			10 ± 2	
	700°C 20'	3.73	5.11	4.25	16 ± 3	15 ± 3
	800°C 20'	3.73	5.12	4.24	105 ± 7	40 ± 4

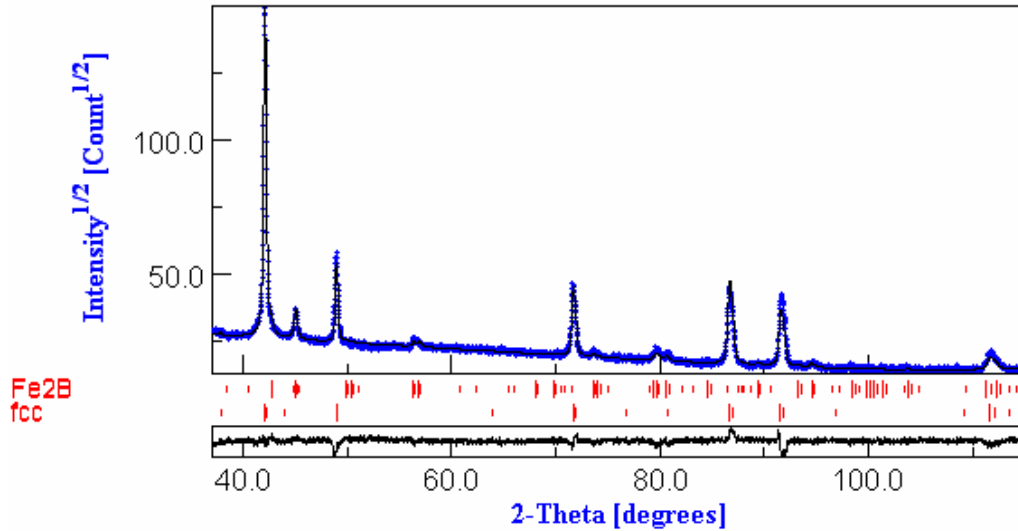


Figure 3.2: MAUD fitting of the XRD diagram of *Ib* sample annealed at 800°C for 20 min.

No superlattice peaks of the tetragonal $L1_0$ have been observed during this experiment. It has to be mentioned that the two main superlattice peaks of tetragonal $L1_0$, the (0 0 1) and (1 1 0) reflections occurs, for the Cu $K\alpha$ radiation used, at about 24° and 32° respectively, and there is a possibility that they could have been hindered by the very broad line centred at 25°. Nevertheless, other peaks belonging to the tetragonal $L1_0$ were not found in the sample.

The fitting of the XRD diagrams has been performed with both MAUD and DATLAB software and the results were consistent for both fitting programs. An example of the MAUD fitting is given in Figure 3.2. It can be seen that the diagram is best fitted with the Fe₂B and the fcc Fe₃Pt phases.

The lattice parameters of the indexed phases and the average grain sizes derived from the fit of the XRD spectra have been obtained using DATLAB software and integral breadth method, described in the previous Chapter. All the results are plotted in Table VIII.

It is to be mentioned the gradual crystallization of the sample, evidenced by the steady, continuous increase of the grain size, up to 700°C. Upon annealing at this temperature, the grain size is remarkably low. Then at 800°C the sample is fully crystallized with large grain sizes of over 100 nm.

Mössbauer analysis

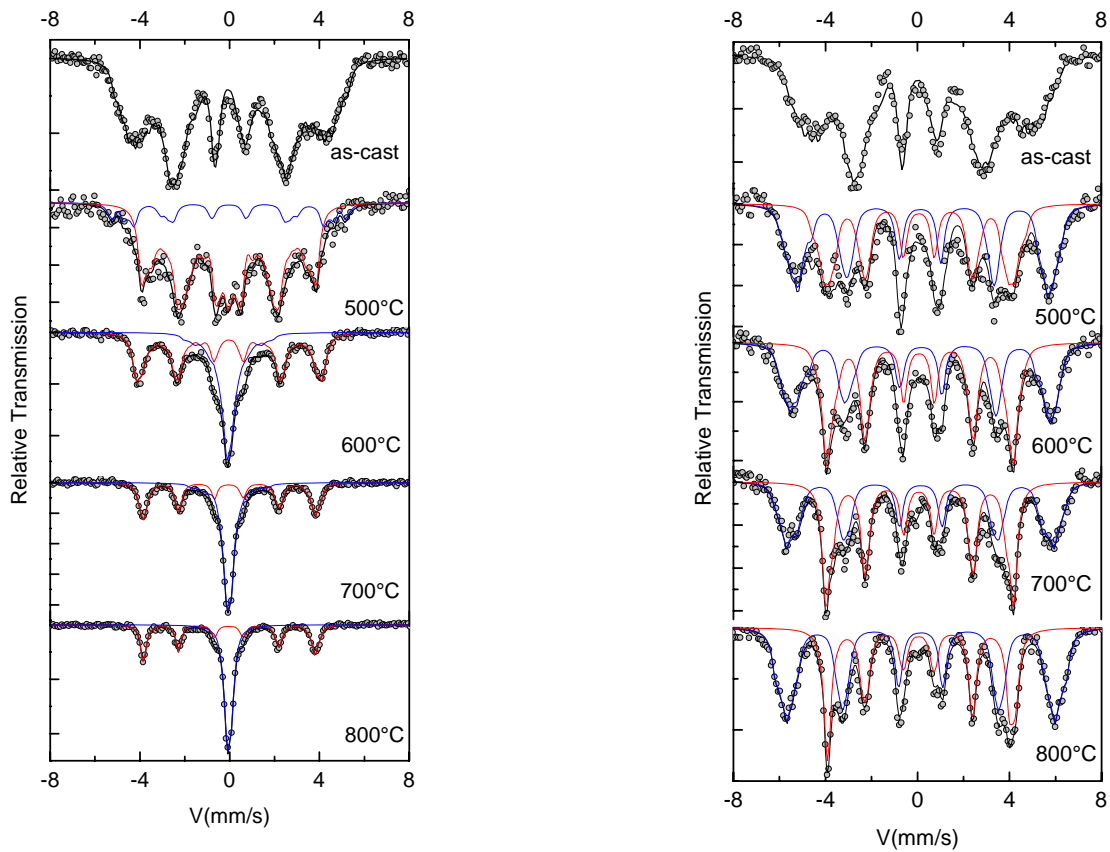


Figure 3.3: 300K and 77K Mössbauer spectra of *1b* sample annealed at 500-800°C for 20 min.

Table IX: Hyperfine parameters obtained from the fit of 300K and 77K Mössbauer spectra

Sample	300K				77K				Phase
	IS (mm/s)	2ε (mm/s)	B _{hf} (T)	%	IS (mm/s)	2ε (mm/s)	B _{hf} (T)	%	
As-cast	0.16	0	23.1	100	0.23	0.04	26.5	100	Al dis.
500°C	0.12	-0.01	28.6	16	0.22	0.07	24.9	45	Fe ₃ B
	0.10	0.1	17	84	0.32	0.1	34	47	Fcc FePt
					0.42	0	5.4	8	d.Fcc FePt
600°C	0.12	0.03	22.7	60	0.24	0.04	24.6	50	Fe ₃ B
	0.09	0	3.9	40	0.29	0.01	34.4	44	Fcc FePt
					0.25	0	4.7	6	d.Fcc FePt
700°C	0.12	0.02	23.6	48	0.23	0	24.7	52	Fe ₃ B
	0.10	0.1	1.7	52	0.29	-0.02	35.3	46	Fcc FePt
					0.10	0	0	2	d.Fcc FePt
800°C	0.12	0.03	23.5	49	0.22	0.05	24.7	41	Fe ₃ B
	0.10	0.1	0.3	51	0.29	0	36	57	Fcc FePt
					0.14	0	0	2	d.Fcc FePt

The estimated errors are: ± 0.02 mm/s for IS and QS/2ε, ± 0.1 T for B_{hf} and ± 1 for the relative proportion

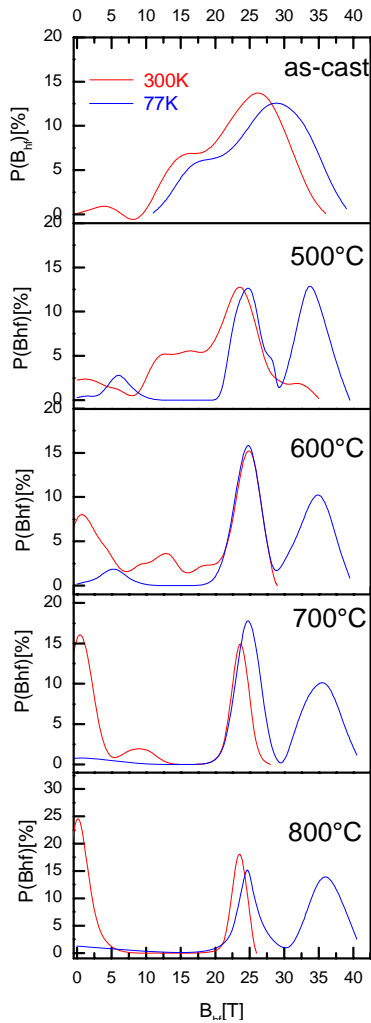


Figure 3.4: HF distributions obtained for 300K and 77K *Ib* spectra annealed at 500-800°C for 20 min.

The Mössbauer spectra of the annealed *Ib* samples are plotted in Figure 3.3. The spectra were all fitted with different HF distributions, corresponding to the different Fe environments. The fitting of the spectra has been done using the Mosfit program [55]. A similar model was used throughout the entire series of samples to ensure the reliability of the results. All the HF distributions obtained for 300K and 77K spectra are plotted in Figure 3.4.

The 300K Mössbauer spectrum of as-cast *Ib* sample, that presents a broad distributed sextet is typical for amorphous-like Fe environments. As discussed in the previous Chapter, the spectrum has been fitted with a bimodal HF distribution. These two modes were interpreted, judging from their average HF values of 16 T and 26 T respectively, as attributed to Fe environments in Fe₂B and fcc FePt.

The 500°C spectrum shows also a broad line sextet, pattern typical for distributed Fe environments but the HF distributions are narrower than in the as-cast state. A high field component of about 28 T is found (blue line in the spectrum fitting) while the broad, distributed sextet (red line) represents the low field HF distribution with an average value of 17 T. The low-field component (red line) is predominant and has a relative intensity of 84%. The HF values are consistent with those obtained for the low-field and high-field distribution modes (see section 2.3.4). The high field (blue) component is attributed to highly disordered fcc A1 FePt, while the low field component (red) is attributed to disordered Fe₂B-rich phase, with a HF lower than Fe₂B bulk phase. This phase is reportedly stable at high temperatures [82] and is characterized by two magnetic sextets with hyperfine fields of about 23.3 and 24.2 T at room temperature. All the obtained hyperfine parameters are shown in Table IX.

The spectrum for 600°C annealing shows different behavior. The lines are much narrower, that is typical of crystallized samples, with less distributed Fe environment. The low field component (red) has a much narrower HF distribution, its mean HF increases to 22.7 T, a value that is closer to that of the Fe₂B bulk phase and its relative abundance decreases to 60%. The blue component attributed to fcc FePt, that at 500°C had a HF value of 28 T, at 600°C becomes paramagnetic, as witnessed by the important singlet appearing in the spectrum. A similar behavior has been observed in the *Ia* as-cast sample (see Figure 2.10). This paramagnetic component has then been attributed to the

magnetically disordered A1 fcc FePt phase. At 600°C annealing, fcc FePt relative abundance increased to 40%.

The 700°C and 800°C spectra show features similar to the 600°C spectrum. It consists of sextets attributed to the Fe₂B and paramagnetic component, assigned to the magnetically disordered A1 fcc FePt. The HF distribution is narrower, as it can be observed in the Figure 3.4, and the individual linewidths are also narrower (see Table IX) than those of the 600°C annealing. The HF of the red component stabilizes around the value of 23.5 which corresponds to the bulk Fe₂B average HF. The blue component, magnetically disordered A1 FePt becomes predominant in the sample reaching more than 50% relative abundance. In XRD, the Bragg lines of Fe₂B are of extremely small intensity, while in Mossbauer analysis the relative proportion of Fe₂B is found to be higher. This can be explained by the high structure factor of Pt, that hinders the occurrence of Fe₂B Bragg lines.

Following the argument developed for the 77K spectrum of *1a* as-cast sample (section 2.3.4) it is expected that the magnetically disordered A1 FePt has to become magnetically ordered at low temperatures.

The spectra recorded at 77K show indeed quite different features than the 300K spectra. As the model of fitting was preserved, the as-cast spectrum, already discussed, has the same broad sextet feature, as at 300K. The low-field and high-field modes in the bimodal HF distribution exhibit larger average HF values: 18 T and 29 T, respectively (see section 2.3.4).

The 77K spectrum of 500°C annealing shows multiple sextet feature. The fitting was based on the same model. The HF distribution is again bimodal, with higher HF average values and narrower than at 300K. Here, the Fe₂B component has a relative abundance of 45% while the component assigned to A1 fcc FePt has large HF of 34 T. A paramagnetic component signalled by the very low HF in the distribution (Figure 3.4) is observed in the sample (8% relative abundance) and belongs to the fraction of A1 FePt phase that remains magnetically disordered at 77K.

At 600°C annealing, the spectrum shows similar features but with narrower lines, as was the case also in the 300K spectrum. Contrary to 300K, the 77K spectrum of the sample annealed at 600°C shows very little paramagnetic component (only 6%). The HF distribution used for fitting the spectrum shows clearly two distributed components with

average HF values of 24.6 T and 34.4 T. They were assigned as in the 500°C annealing, to the Fe₂B and magnetically ordered fcc Fe₃Pt. The paramagnetic component observed at 300K transforms into a distributed sextet with large HF. It follows that at 77K the fcc FePt phase undergoes a magnetic disorder-order transition.

At 700°C and 800°C the spectra are highly similar: the same fitting model is used and the same components are retrieved, as in the 600°C case. The HF distributions are narrower, signalling the continuous process of structural refinement as proven also by the XRD results. While at 700°C annealing, Fe₂B has a relative abundance of 52%, at 800°C the A1 fcc FePt predominates having a relative abundance of 57%. A small fraction of A1 fcc FePt remains still magnetically disordered as shown by the paramagnetic component of about 2% relative abundance, even after annealing at 800°C.

The assignation of the observed component to FePt phases has been facilitated by a complementary study of ribbons of binary FePt alloys of several compositions. We have synthesised these ribbons, studied their structures and correlated them with Mössbauer analysis. This analysis will be described in Annex A. Following this study we were able to correctly assign the observed contributions to different FePt phases.

The Mössbauer spectra confirm thus the XRD results where we have observed the formation of cubic FePt phases and Fe₂B starting with the annealing at 700°C.

To summarize the phase evolution that has been observed in the Fe₆₈Pt₁₃Nb₂B₁₇ (*Ib*) sample, as documented by the XRD and Mössbauer results, the following sequences of crystallization may be depicted:

1. 500°C-600°C: Amorphous-like fcc A1 disordered FePt-rich \longrightarrow fcc Fe₃Pt + residual FePtNbB
2. 700°C-800°C: fcc Fe₃Pt + residual FePtNbB \longrightarrow fcc Fe₃Pt + Fe₂B

These results differ slightly from the ones obtained during the dynamic annealing in the temperature-dependent X-ray diffraction of synchrotron radiation study, as the experimental conditions of annealing were different. Nevertheless, by static isothermal annealing, the *Ib* samples show magnetic hardening, depending on the annealing temperature as it is described hereafter.

VSM analysis

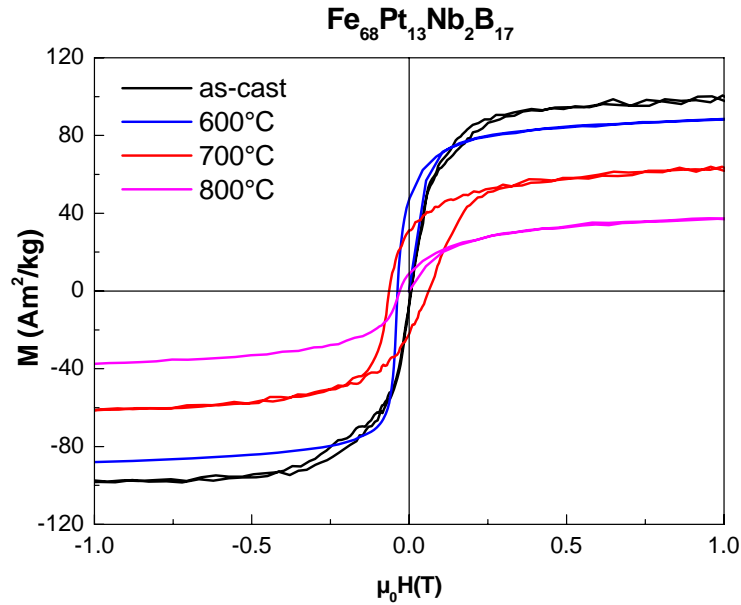


Figure 3.5 RT hysteresis loops for the as-cast and annealed Ib samples

The magnetic properties of the Ib samples annealed for 20 minutes at various temperatures were checked by the hysteresis loops, recorded at room temperature using a VSM with parallel applied field up to 1.5 T. Selected loops are presented in Figure 3.5. The curves are typical for soft magnetic materials, but as the annealing temperature increases the saturation magnetization decreases due to the continuous increase of the grain size, and the steady increase of the paramagnetic contribution, observed in the Mössbauer spectra, as the annealing temperature increases. Most interesting is that a magnetic hardening occurs in the annealed sample, with non-negligible coercive fields being noted for the annealed sample, the maximum occurring for the annealing at 700°C. In order to confirm that the coercivity has indeed a maximum at this annealing temperature, we have performed on the Ib sample, three more annealing treatments at 485°C, 615°C and 895°C. The obtained samples were measured with the VSM in the same conditions and the coercivities of all the annealed samples, plotted as a function of annealing temperature, are shown in Figure 3.6.

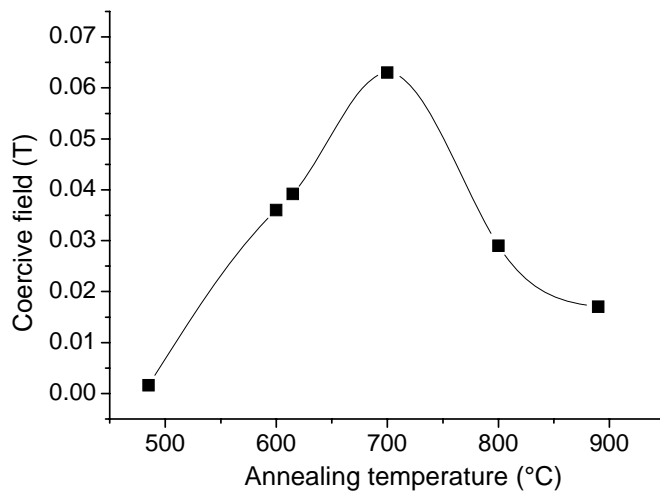


Figure 3.6 Coercive fields obtained for the annealed 1b sample, as a function of annealing temperature

It has to be noted that the maximum in the coercivity is indeed reached for the annealing at 700°C. As the metastable as-cast state is magnetically soft, after annealing the crystals nucleate and grow in a 3D model, as described in section 2.4. The nanograins formed are monodomains, for intermediate stages of annealing 500°C-600°C. At 700°C the average grain size is only 16 nm. This refined microstructure is formed of grains of two or more magnetic phases and due to various reversal mechanisms, the coercive field increases up to the maximum. After 800°C annealing the grains have increased up to 100 nm (see Table VIII) and this leads to the decrease of the coercivity as observed in Figure 3.6.

3.2. Isothermal annealing of Pt-rich alloys

3.2.1. Modifications in the chemical compositions of FePtNbB alloys: structural effects

Let us recall the compositional considerations, described in Chapter 2.

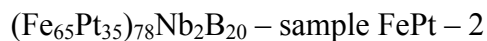
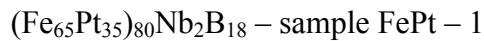
We have observed that for 25% boron content, the FePtNbB alloy has been obtained in a mostly amorphous state. Only 8-9% boron content in the sample, as the case of 1a and 2a samples, are not sufficient in order to ensure an amorphous-like as-cast state. Instead, the samples are directly obtained in a crystalline state, the phase structure is well formed and consists of mainly A1 cubic FePt phase, and further annealing treatments

do not produce further microstructure evolution. Only in special situations, such as dynamic annealing under applied pressure, a coexistence of hard and soft phases is obtained. Therefore, we tried to change the initial compositions of the ribbons with the aim to obtain competitive values of both coercivity and remanence.

Concretely, we have produced the so-called Pt-rich batch of samples, two new compositions in the same operational conditions as the Fe-rich batch of samples. The changes operated in the compositions were the following:

- a) We have settled an overall Fe:Pt ratio off-stoichiometry to 65:35. 35 at.% of Pt corresponds to the region of formation of both $L1_0$ and $A1$ FePt phases in the phase diagram. Compared to previous syntheses that have an overall Fe:Pt ratio of 68:21, 68:13 and 65:25, thus an excess of Fe, we have increased the Pt content, in order to favour the presence of FePt hard phase and to impeach the formation of iron borides.
- b) We have settled the boron content at intermediate values between 9 and 25%. The boron content must be high enough as to ensure an amorphous-like as-cast state. Therefore, we decided to use 18-20% boron in the initial composition.

The new synthesized ribbons, as mentioned in the previous Chapter had the initial compositions:



3.2.2 Choice of the annealing conditions

We have previously seen both in XRD and in Mössbauer spectra that the two Pt-rich as-cast samples exhibit similar features. Both Mössbauer spectra exhibit broad magnetic sextets, that are observed for distributed chemical environments of Fe nucleus, accounting for the short-range-order encountered in Fe-rich amorphous ribbons (Figure 2.12). The XRD diagrams (Figure 2.8) are also highly similar, with Bragg lines indexed as belonging to the disordered fcc $A1$ FePt-rich solid solution, and one small but sharp Bragg peak corresponding to the superlattice $(1\ 1\ 0)$ of the $L1_0$ phase occurring in both samples. The only difference is the larger linewidth of the $(1\ 1\ 1)$ reflection for the

sample with more boron content (FePt – 2). Due to these features, these samples are promising for formation of tetragonal $L1_0$ phase upon annealing.

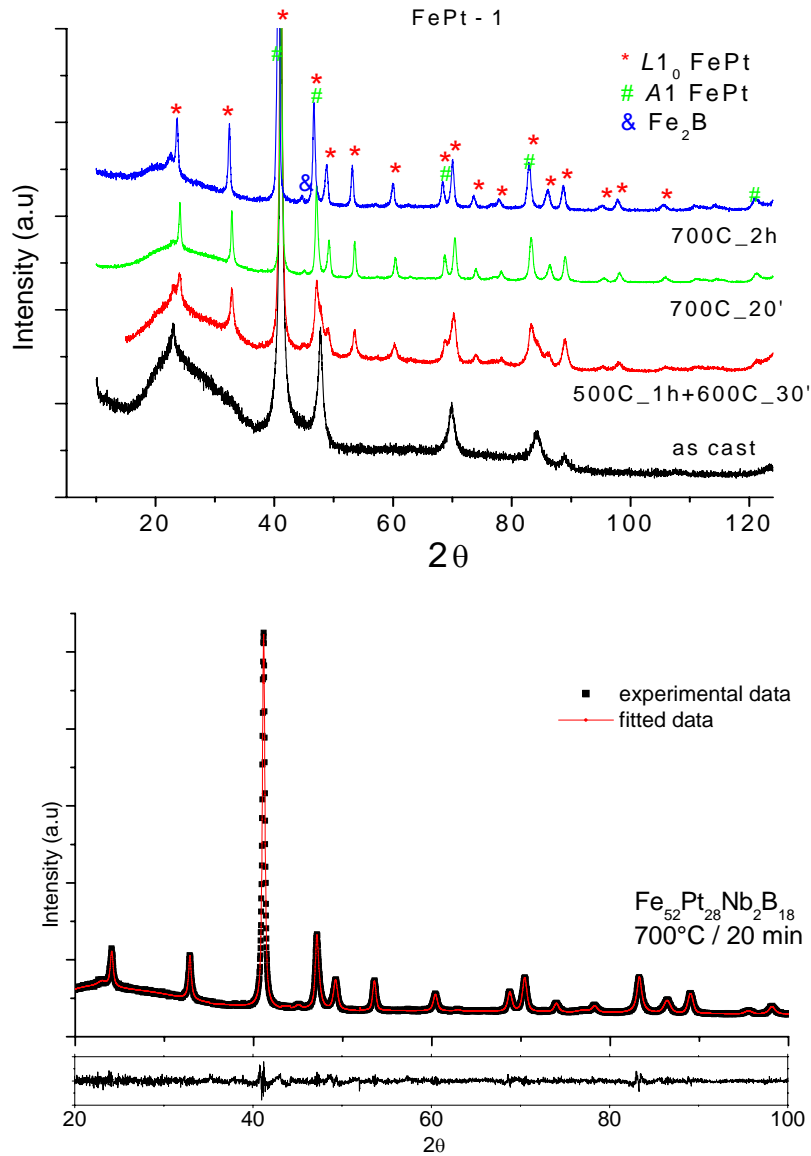
In the DSC curves for the FePt – 1 and FePt – 2 samples (Figure 2.21), a well defined exothermic peak was found for both samples, at around 560°C while some other pre-peaks, also exothermic, were found between 460°C - 480°C. As a consequence we have decided to choose the annealing temperatures at 500°C (after the exothermic pre-peaks), 600°C (after the main exothermic peak, attributed to the crystallization processes and/or $A1 - L1_0$ structural phase transformation) and finally at 700°C. The annealing temperatures have been signalled on the DSC graph with vertical bars for clarity.

In order to obtain the formation of stable microstructure with refined grain sizes and suitable arrangement of alternatively dispersed grains $L1_0$ and $A1$ FePt phases, the two samples were subjected to several annealing treatments:

- Two-steps procedure: annealing at 500°C for 1 hour, followed by annealing at 600°C for 30 minutes. This two-steps annealing has the role to allow first the structural strains to relax, and to obtain a more homogeneous solid solution, prior to crystallization. The relaxation of the stresses induced from the preparation is observed in the DSC scan at around 470°C. Therefore, the annealing that should provide homogenization of the solid solution prior to crystallization, was performed at 500°C. This is followed by an annealing treatment at 600°C, after the crystallization temperature, which in this case is around 560°C. This second annealing is required to ensure the formation of uniform grained nanocrystalline microstructure with not-so-large grain sizes.
- Annealing at 700°C for 20 minutes (40 minutes in the case of FePt – 2). This annealing is performed at higher temperatures without a prior (pre-crystallization) treatment. This is to investigate the effect of crystallization from the solid solution, if the temperature is higher but the annealing time is lower than in the first case.
- Annealing at 700°C for 2 hours. This annealing is performed for a longer period, in order to study the effect of time on the grain arrangements and to ensure the complete crystallization of the sample.
- Annealing at 700°C for 1 hour. At a later stage during the present study, this annealing was performed in order to optimize some of the magnetic properties.

3.3. Phase structure of the annealed Pt-rich alloys

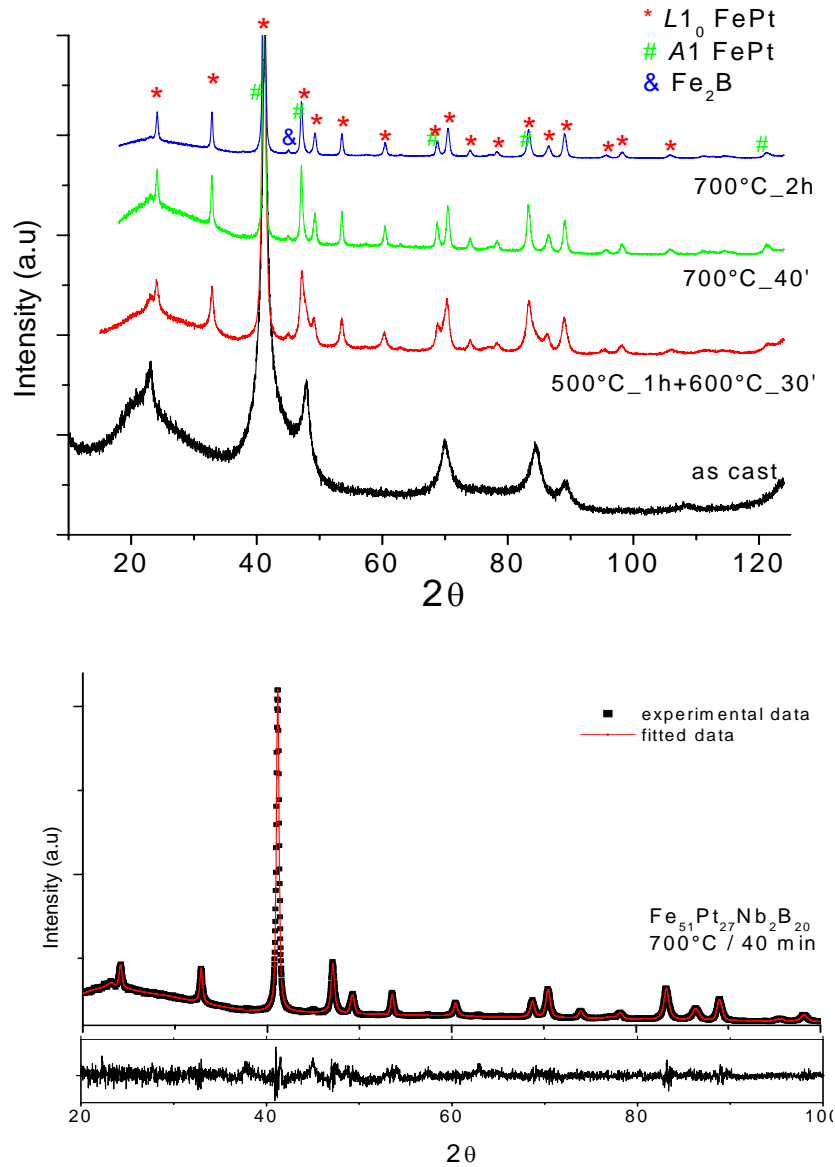
3.3.1 XRD studies



Figures 3.7: XRD diffractograms for as-cast and annealed $(Fe_{65}Pt_{35})_{80}Nb_2B_{18}$ samples (top) and an example of numerical fitting with Matlab (bottom)

Structural characterization of the annealed samples was performed in the same conditions as for the as-cast samples. Figures 3.7 and 3.8 show the X-ray spectra of annealed samples $(Fe_{65}Pt_{35})_{80}Nb_2B_{18}$ – FePt – 1 and $(Fe_{65}Pt_{35})_{78}Nb_2B_{20}$ – FePt – 2,

compared with their as-cast counterparts respectively. Also, an example of fitting with Datlab is provided.



Figures 3.8: XRD diffactograms for as-cast and annealed $(\text{Fe}_{65}\text{Pt}_{35})_{78}\text{Nb}_2\text{B}_{20}$ samples (top) and an example of numerical fitting with Datlab (bottom)

In both samples, it is obvious that the main Bragg lines observed in the fcc FePt solid solution in the as-cast state, undergo a refinement process as the annealing temperature is increased, from bottom to top, similar to what we have seen for *Ib* sample. The main 5 Bragg lines of the cubic A1 FePt solid solution in the as-cast state, from lower

to higher angles, are, in order, attributed to: (1 1 1), (2 0 0), (2 2 0), (3 1 1) and (2 2 2). Contrary to the *Ib* case, here these main reflections are in fact overlapped with the main Bragg reflections of the $L1_0$ FePt tetragonal phase. It is very interesting to observe that already, at the first annealed sample, annealed at 500°C_1h + 600°C_30', the (2 0 0), (2 2 0) and (3 1 1) peaks split into two. It seems that the peaks from the cubic phase are now spectrally separated from those of the tetragonal phase. For the other two annealing treatments, in both Figures 3.7 and 3.8, the separation continues and the peaks become more and more narrow and better separated one from another. The specific signatures of the tetragonal $L1_0$ phase, the superlattice peaks (0 0 1) and (1 1 0), are clearly observed for all the annealed samples at around 24° and 33° (in 2-theta), respectively.

The good separation of the spectral lines allowed us accurate determination by numerical fitting of the peaks positions and linewidths, calculation of the lattice parameters and of the mean grain sizes for each observed crystalline phases. The software used for the fitting and the integral breadth method were largely described in Chapter 2. The obtained results are schematized in Table X.

Table X: Lattice parameters and grain sizes for the as-cast and annealed $(\text{Fe}_{65}\text{Pt}_{35})_{80}\text{Nb}_2\text{B}_{18}$ and $(\text{Fe}_{65}\text{Pt}_{35})_{78}\text{Nb}_2\text{B}_{20}$ samples

Sample	Anneal.	$L1_0$ FePt			A1 FePt	Grain size	Grain size
		a (Å)	c (Å)	c/a	a (Å)	$L1_0$ FePt (nm)	A1 FePt (nm)
$(\text{Fe}_{65}\text{Pt}_{35})_{80}\text{Nb}_2\text{B}_{18}$	500_600	3.8542± 0.0043	3.7127± 0.0067	0.9632	3.8315± 0.0308	15 ± 2	17 ± 3
	700_20'	3.8537± 0.0027	3.7034± 0.0042	0.9609	3.8168± 0.0284	30 ± 3	36 ± 4
	700_2h	3.8524± 0.0049	3.7107± 0.0071	0.9622	3.8579± 0.0247	46 ± 5	49 ± 5
$(\text{Fe}_{65}\text{Pt}_{35})_{78}\text{Nb}_2\text{B}_{20}$	500_600	3.8546± 0.0052	3.7006± 0.0051	0.9600	3.8292± 0.0303	17 ± 3	14 ± 3
	700_40'	3.8565± 0.0034	3.6936± 0.0033	0.9577	3.8309± 0.0320	33 ± 4	44 ± 5
	700_2h	3.8553± 0.0043	3.6911± 0.0047	0.9574	3.8512± 0.0054	45 ± 5	48 ± 5

It can be seen that the lattice parameters, as revealed from the fit of the experimental spectra, do not change drastically for the annealing treatments at 500°C_1h + 600°C_30' and 700_20'. On the contrary, the annealing at 700°C for 2h shows larger lattice parameters for the cubic FePt phase, in the case of FePt – 1 sample. The volume of the unit cell is increased for the 2h annealing time. Here, the crystallization process is

complete and the lattice increases most probably by accommodating larger atoms, such as B and Nb, into the lattice.

The grain size for both $L1_0$ and $A1$ FePt phases in the annealed FePt – 1 and FePt – 2 samples, increases continuously from the as-cast values 11 nm (7 nm respectively) as the annealing temperature / time increases. At 700°C / 20' annealing, the grain size in the FePt – 1 is about 30 nm while the same annealing for the FePt – 2 sample has led to slightly larger values for both $L1_0$ and $A1$ FePt phases.

In conclusion, in the annealed FePt – 1 and FePt – 2 samples, using structural data, we have unambiguously proven the coexistence of the hard and soft magnetic phases with well-refined grain sizes. The ultrafine grained microstructure has been observed also by transmission electron microscopy (TEM). These observations may be made quantitative with the help of the Mössbauer spectroscopy where the relative fraction of each of the phases present in the samples may be derived. In the next Chapter, the magnetic properties will be thoroughly studied and deeply investigated.

3.3.2. Transmission electron microscopy

In order to investigate the morphology of the grain dispersion within the sample, we have performed transmission electron microscopy imaging on some of the most promising samples from the point of view of magnetic properties. The TEM observations are also meant to derive the grain sizes, since the values obtained from XRD spectra are only estimations more or less accurate, depending on various X-ray scattering factors and supplemental instrumental broadening that sometimes cannot be correctly taken into account. The TEM images, performed at the Institute of Experimental Physics, Slovak Academy of Sciences, Bratislava, have been taken using a JEOL JEM 2100 electron microscope with a 200kV acceleration voltage and 2 nm beam resolution, both in dark and bright field. The samples to image were thinned down to be transparent to the electron beam, by reactive ion etching by plasma discharge.

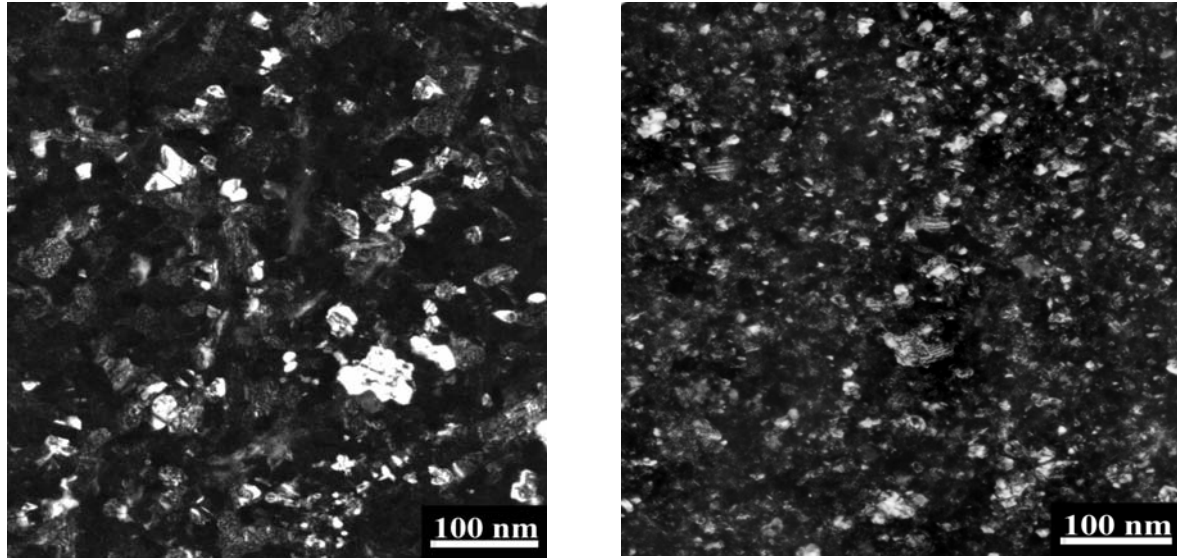


Figure 3.9: Dark field TEM image for the sample $\text{Fe}_{51}\text{Pt}_{27}\text{Nb}_2\text{B}_{20}$ (left) and $\text{Fe}_{52}\text{Pt}_{28}\text{Nb}_2\text{B}_{18}$ (right) annealed at $500^\circ\text{C}/1\text{h}$ $600^\circ\text{C}/0.5\text{h}$

Figure 3.9 shows the dark field transmission electron microscopy image of the two Pt-rich samples annealed at $500^\circ\text{C}/1\text{h}+600^\circ\text{C}/30\text{min}$. A microstructure consisting of well-defined, almost regularly dispersed faceted grains with different image contrast is observed in both samples. The contrast difference indicates the multiple phase character of the observed grains. It is likely that the grains with strained top surface and those which give brighter contrast would be the FePt cubic or tetragonal grains, since Pt is the heavier element and the contrast is proportional to the Z number of the elements. The diffuse, out of focus, dark regions may belong to the residual soft magnetic matrix that is rich in boron, a much lighter element which does not furnish a lot of contrast in the electron beam.

Among the well-dispersed grains, some large clusters of grains are also observed. These are not large bulk-like forms, but more probably, clusters of grains that coalesce one near the other on the linear facets of individual grains. By direct measurement of only the grains with visible edges, the mean grain size averaged over the visible grains in the

images, was determined to be about 16 nm in FePt – 1 and 24 nm in FePt – 2, respectively.

Taking into account the fact that only a small part of the microstructure is imaged by TEM and the results derived are highly local, the agreement with the grain size derived from the XRD (Table X) is quite remarkable.

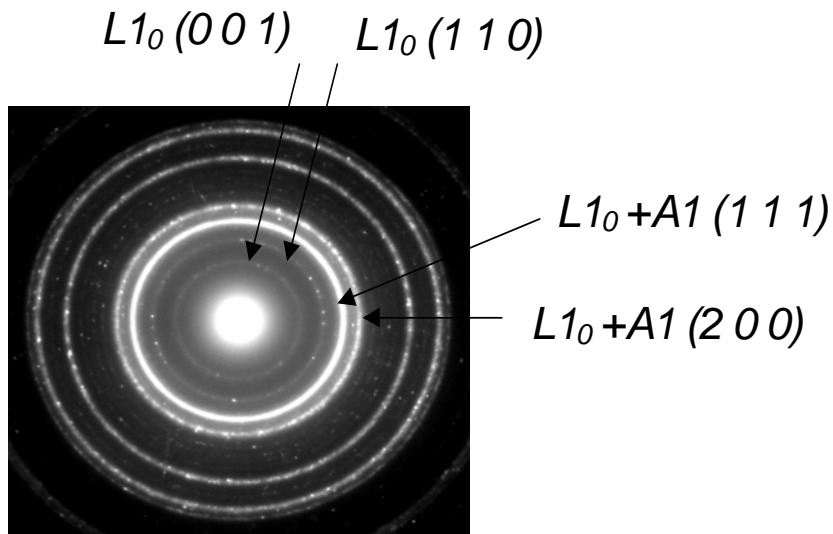


Figure 3.10. Electron diffraction patterns (EDP) of the FePt – 1 sample annealed at 500°C/1h 600°C/0.5h

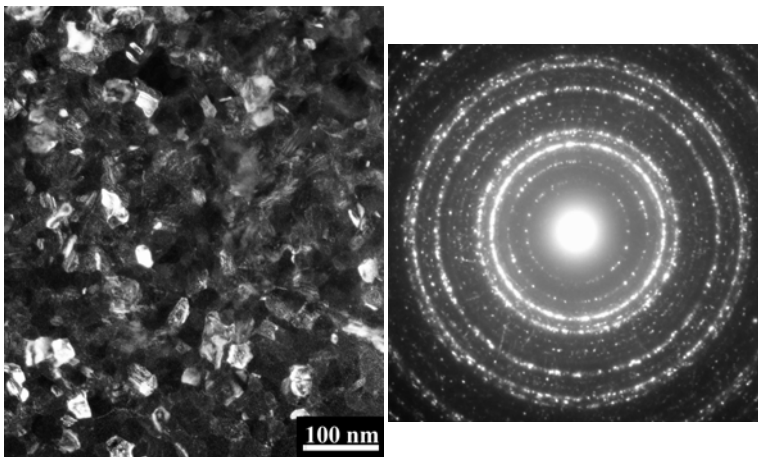


Figure 3.11 TEM image and Electron diffraction patterns (EDP) of the FePt – 1 sample annealed at 700°C/1h

Nevertheless, since the grain sizes obtained from XRD, a measurement that gives information on a much larger area from the sample, are only between 14 and 17 nm, for

both $L1_0$ and $A1$ FePt phases, we can infer that the few large agglomerates observed in the TEM image of FePt – 2 sample does not represent an important volume fraction of the sample.

The electron diffraction pattern from the TEM image of the FePt – 1 sample annealed at $500^\circ\text{C}/1\text{h}$ $600^\circ\text{C}/0.5\text{h}$ (Figure 3.10) has been indexed with the most important reflections of the $L1_0$ and $A1$ FePt phases. The diffraction rings closest to the central spot of light are the two superlattice peaks of the $L1_0$ FePt phase (0 0 1) and (1 1 0) while the following ones, the most bright, belong to the main Bragg reflections of both $L1_0$ and $A1$ FePt phases, the (1 1 1) and (2 0 0) reflections as it has been indexed on Figure 3.10. The TEM image and corresponding EDP for the FePt – 1 sample annealed at $700^\circ\text{C}/1\text{h}$ are presented in Figure 3.11. While the same morphology of well dispersed nanograins of rather uniform size is observed as in the case of $500^\circ\text{C}/1\text{h}$ and $600^\circ\text{C}/0.5\text{h}$ annealing, the average grain size in that case is larger, being about 35-45 nm, as expected due to the higher annealing temperature. Also, the EDP shows almost similar system of rings, from the same $L1_0$ and $A1$ FePt phases but the rings are highly discontinued which is a feature characteristic of diffraction patterns of polycrystals, with more coarsened grain structure.

We can conclude that indeed the microstructure of the annealed samples is made of well-dispersed and small hard and soft magnetic grains, an important prerequisite of obtaining an exchange spring magnet. The direct imaging of the grain sizes give rather good agreement with the results obtained from XRD, confirming thus our method of calculations based on the integration of the diffraction peaks following the integral breadth method.

3.3.3. Mössbauer spectrometry on annealed ribbons. Identification of the phase structures.

The key factor to obtain a material with good exchange spring magnetic behavior is the coexistence of hard and soft phases at a nanometric scale, in a suitably dispersed microstructure. These hard and soft phases need to be unambiguously identified, characterized and their relative abundance needs to be weighted in order to understand and correctly interpret the magnetic behavior.

As pointed out in the previous Chapter, to distinguish between $A1$ and $L1_0$ FePt phases in XRD data, is difficult. The superstructure (0 0 1) and (1 0 0) peaks are the only valid signature of the presence of the tetragonal $L1_0$ FePt phase in the alloy. On the other hand the accuracy of deconvoluting for example the main (1 1 1) peak that belongs to both $A1$ and $L1_0$ FePt phases, is much lower in the case of XRD.

To identify correctly the phases present in the microstructure of the samples we will make use again of the Mössbauer spectroscopy (MS). There are several advantages of the use of this technique in the specific case of our multiple phased samples.

- MS is extremely sensitive to the chemical environment of the Fe nucleus and it provides three different hyperfine parameters that may be used in order to distinguish between different symmetries of the same FePt alloy. These parameters, obtained from the fitting of Mössbauer spectra, are: the isomer shift (IS), the quadrupole splitting (QS) and the hyperfine field (B_{hf}). Combined with the XRD results, this set of parameters uniquely characterize a given phase structure.
- MS also provides a reliable quantitative analysis of the amount of a given phase structure in the sample via the relative abundance parameter that is also obtained from the fitting of the Mössbauer spectra.

Therefore, combined with magnetic measurements, MS may be used to obtain information about the magnetic configurations in the sample and more precisely in our alloys, if the sample has a microstructure with multiple FePt phases.

In the literature, the reports on the Mössbauer parameters of different FePt phases are relatively scarce. Goto [24] and Spada et al [81] have reported that the Mössbauer spectrum of $A1$ cubic FePt phase can be fitted with a single component with a hyperfine field of about 30 T. But the reports on the hyperfine parameters of the tetragonal $L1_0$ FePt phase are more controversial. Goto [24] has reported that the Mössbauer spectrum of the tetragonal FePt can be fitted with 3 sublattices. The hyperfine field values are though strongly dependent on the conditions of synthesis and annealing of the samples and on the relative Fe:Pt amount. Nevertheless, other reports suggest that the tetragonal phase is characterized by a single sublattice having the hyperfine field of about 27.7 T and quadrupole shift of 0.29 mm/s.

In order to avoid misinterpretation of the fitting results and to provide correct assignation to both $A1$ cubic and $L1_0$ tetragonal FePt phases, we have synthesized binary FePt alloys with the following compositions: $\text{Fe}_{25}\text{Pt}_{75}$, $\text{Fe}_{50}\text{Pt}_{50}$ and $\text{Fe}_{75}\text{Pt}_{25}$ (Fe_3Pt). We have then recorded the Mössbauer spectra of the three alloys and we derived in that way the correct hyperfine parameters for all the necessary phases. Having obtained the parameters for the FePt phases of interest, the assignation of the fitted sublattices to the corresponding phases and interpretation of the hyperfine parameters obtained from the fit provided reliable results. Details are given in Annex I.

^{57}Fe Mössbauer analysis on all the samples has been performed at the LPEC, Université du Maine, Le Mans, using a conventional setup in transmission geometry. The Mössbauer source is ^{57}Co embedded in a Rh matrix. Measurements were carried out at ambient temperature and also at 77K. The as-cast and annealed $\text{Fe}_{51}\text{Pt}_{27}\text{Nb}_2\text{B}_{20}$ and $\text{Fe}_{52}\text{Pt}_{28}\text{Nb}_2\text{B}_{18}$ samples have been investigated and their Mössbauer spectra, recorded at -10 +10 mm/s velocity range, have been fitted, as we have already mentioned, with the Mosfit [55] fitting program. The fitting procedure was the same for all the annealed samples, in order to avoid artifacts due to changes in the fitting procedure, and the hyperfine parameters were all free parameters during the fitting. The FePt – 1 and FePt - 2 as-cast samples present broad patterns that are typical for amorphous Fe-based alloys, as it has been already seen in the previous Chapter (Figure 2.12). This is a result of a chemically disordered environment of the Fe nuclei that give rise to a distribution of hyperfine fields which produces the broadening of the magnetic sextet. The hyperfine field distribution was found to be of bimodal shape and the average hyperfine field for the as-cast samples were 21.8 T and 22.2 T (see section 2.3.4).

In Figure 3.12 the Mössbauer spectra of three of the annealed $\text{Fe}_{52}\text{Pt}_{28}\text{Nb}_2\text{B}_{18}$ (FePt – 1) samples are presented together with the subspectra, as identified from the fitting. All the hyperfine field parameters obtained from the fit are depicted in Table X. The components used for the fitting are of the same color as their hyperfine parameters, for an easier identification.

Mössbauer spectra of the annealed samples show different and more complex hyperfine features. Indeed the Mössbauer patterns consist of sextets with much narrower lines which indicate that the samples are crystallized. The fitting model chosen to adjust the spectra of annealed samples takes into account the TEM and XRD results where a microstructure consisting of multiple phases was proven. The spectra have been fitted with a number of subspectra that were indexed and assigned to the phases identified in the XRD.

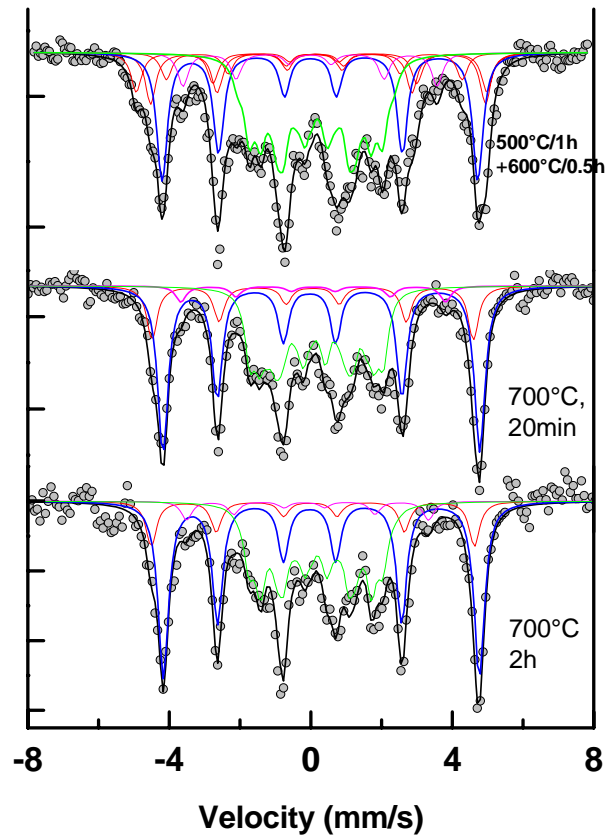


Figure 3.12: Mössbauer spectra for $\text{Fe}_{52}\text{Pt}_{28}\text{Nb}_2\text{B}_{18}$ annealed samples

Table XI: Hyperfine parameters as resulted from fitting of the Mössbauer spectra (Fig. 3.12)

Samples	IS (mm/s)	$\Gamma/2$ (mm/s)	2ε (mm/s)	B_{hf} (T)	%	Phase
500°C/1h 600°C/0.5h	0.21	0.18	-0.1	30.5	8	A1(FePt)
	0.30	0.18	0.1	29.2	10	A1(FePt)
	0.27	0.18	0.27	27.6	28	L1 ₀ (FePt)
	0.23	0.18	0.1	25.8	7	Fe ₃ B
	0.12	0.18	0	22.1	7	Fe ₂ B
700°C/20 min	0.20	0.18	0	28	13	A1(FePt)
	0.28	0.18	0.33	27.6	43	L1 ₀ (FePt)
	0.12	0.18	0	22.8	5	Fe ₂ B
	0.28	0.18	0.06	9.5	39	(Fe _{0.56} B _{0.44}) ₉₅ Nb ₅
700°C/2h	0.17	0.18	0.06	28.1	12	A1(FePt)
	0.28	0.18	0.33	27.5	44	L1 ₀ (FePt)
	0.11	0.18	0	22	6	Fe ₂ B
	0.29	0.18	0.1	9.5	38	(Fe _{0.55} B _{0.45}) ₉₄ Nb ₅

The estimated errors are: ± 0.02 mm/s for IS and QS/ 2ε , ± 0.1 T for B_{hf} and ± 1 for the relative proportion

The Mossbauer spectra of the sample annealed at 500°C/1h-600°C/30min has been fitted with 6 subspectra, a fitting model that corresponds to the situation observed in the XRD data. The same model has used for all annealed samples in order to ensure the correctness of the fittings and the reliability of the obtained hyperfine parameters.

The two subspectra designed by the red line in Figure 3.12 have been assigned to the A1 cubic FePt phase. The hyperfine parameters are depicted in the Table XI. The quadrupole shift value suggests a cubic symmetry while the hyperfine field of 30 T is typical for A1 FePt phase that is consistent with the results on *Ib* sample and on the binary alloy. The relative proportion of the cubic phase, as resulted from the fit, is 18%. The HF parameters obtained are consistent with results reported in the literature [24] and with those obtained from the investigation on the binary alloys.

The subspectrum designed by the blue line in Figure 3.13 has been assigned to the L1₀ FePt phase. The quadrupole splitting of 0.27 mm/s suggests a tetragonal symmetry and the hyperfine field of 27.6 T corresponds to the value found for the binary equiatomic alloy. Its hyperfine parameters, depicted in Table XI are again consistent with those from the corresponding equiatomic binary alloy. For the annealing at 500_600°C this phase is the most abundant in the sample. Its relative proportion, as revealed from the fit, is 28%. This indicates that the disorder-order phase transition has started and an important

fraction of the initial cubic FePt solid solution is already transformed into tetragonal $L1_0$ FePt.

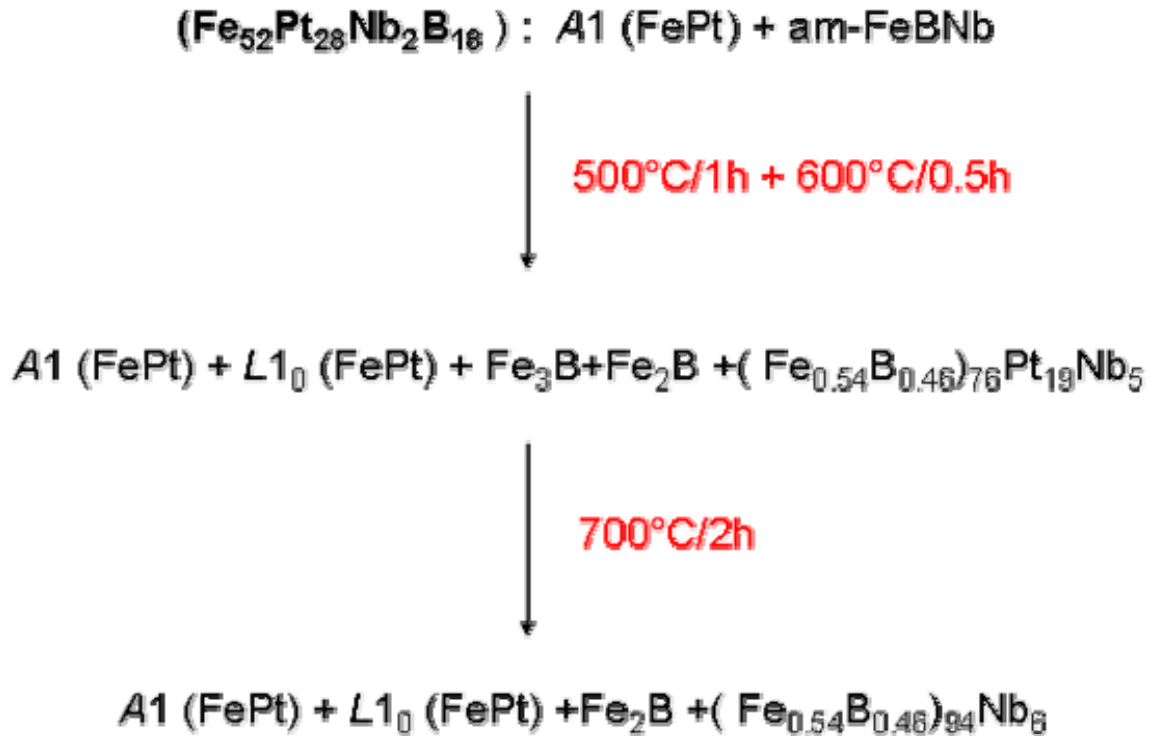
The pink lines are the components of the boride phases. Fe_2B has been already observed in the *1b* sample. Fe_3B is a metastable phase that may be formed in intermediate stages of annealing. It has been documented that after $600^\circ C$ Fe_3B decomposes into α -Fe and Fe_2B [82]. Their total relative intensity amounts to 14%.

The central part of the spectrum was fitted with a HF distribution between 3.5 and 18.5 T. These contributions are represented convoluted as one contribution (green) in Figure 3.13. The average hyperfine field of these low-field contributions is 9.9 T and its relative intensity amounts to 40%. From the HF value we can assume that this low-field contribution to the Mössbauer spectrum may be attributed to the disordered FeB-rich phase. Its composition has been calculated taking into account the other crystalline phases observed in the spectra and their relative proportion. The calculated stoichiometry is given in Table XI, for each annealed sample. The quadrupole shift close to 0 sustains the argument of a cubic symmetry of this phase. The low hyperfine field of this contribution suggests that is a Fe-poor phase. From all of the arguments we consider that the green contribution may be a disordered FeB phase with Pt atoms interstitially inserted or randomly occupying the Fe sites. This phase is probably located in interfacial regions between the nanocrystalline grains and in grain boundaries.

The Mössbauer spectra of the sample annealed at $700^\circ C$ 20 min and $700^\circ C$ -2h have the same complex pattern as the previous one, but with better resolved lines. The spectra were fitted using the same fitting model. The parameters were consistent throughout the series of measurements. From Table XI one can observe the phase evolution with the annealing conditions as well as the relative abundance of the $A1$ and $L1_0$ FePt phases. The tetragonal phase increases slightly up to 44% while Fe_3B decomposes. It can be seen that Fe_2B relative abundance does not increase therefore we may assume that from the decomposition of Fe_3B , Fe helps the formation of $L1_0$ FePt and B is incorporated into the FeB-rich residual phase. With increasing annealing

temperature, all the phases that decompose help formation of $L1_0$ phase, which is the most ordered one, in the ribbon microstructure.

In agreement with the XRD and Mössbauer results the processes of transformation upon annealing may be schematized as:



The Mössbauer spectra of three of the annealed $\text{Fe}_{51}\text{Pt}_{27}\text{Nb}_2\text{B}_{20}$ (FePt – 2) ribbons are presented in Figure 3.13.

Components assigned to the $A1$ cubic (red) and $L1_0$ tetragonal (blue) FePt phases were fitted to all the annealed samples and their hyperfine parameters (Table XII) were consistent throughout the whole series of annealings in both samples. Other components used for fitting the spectra (green) correspond to disordered FeB-rich crystalline phases with low hyperfine fields, that emerge from the residual matrix in secondary stages of crystallization. These components are almost constant in relative intensity at about 39% for all the annealings. The same thing for the Fe_2B (pink) whose relative intensity, as in the previous case, is at around 5% for all the annealings.

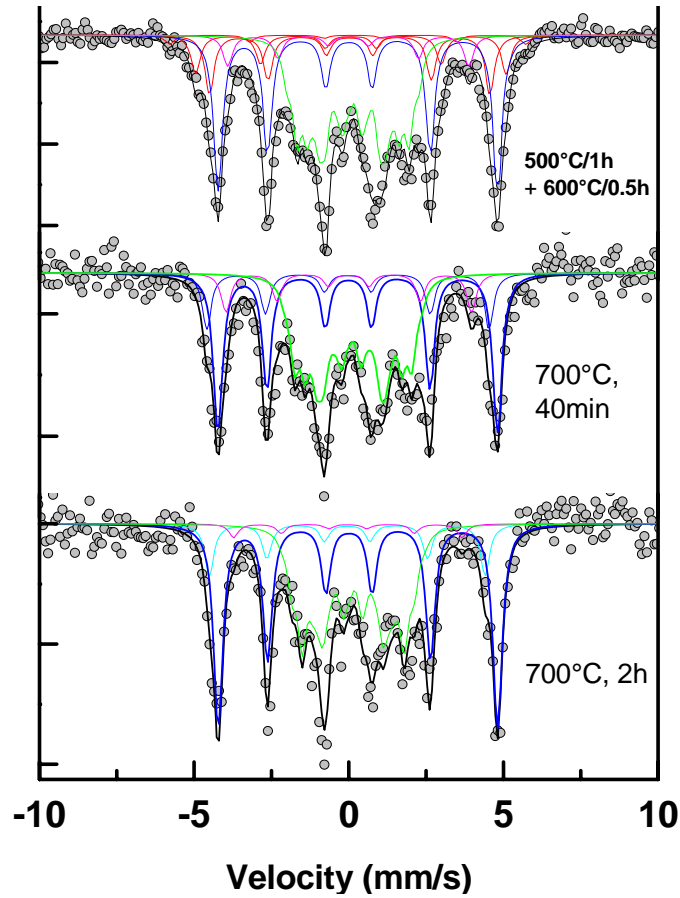


Figure 3.13: Mössbauer spectra for $\text{Fe}_{51}\text{Pt}_{27}\text{Nb}_2\text{B}_{20}$ annealed samples

Table XII: Hyperfine parameters as resulted from fitting of the Mössbauer spectra (Fig. 3.13)

Samples	IS (mm/s)	$\Gamma/2$ (mm/s)	2ε (mm/s)	B_{hf} (T)	%	Phase
500°C/1h 600°C/0.5h	0.20	0.18	-0.18	35.5	2	A1(FePt)
	0.22	0.18	0	30.9	8	A1(FePt)
	0.18	0.18	0	27.9	12	A1(FePt)
	0.30	0.18	0.29	27.8	32	L1₀(FePt)
	0.13	0.18	0	23.9	6	Fe₂B
700°C/40 min	0.28	0.17	0	9.8	40	(Fe_{0.55}B_{0.45})₉₅Nb₅
	0.12	0.18	0	28.3	14	A1(FePt)
	0.29	0.18	0.3	28	42	L1₀(FePt)
	0.15	0.18	0	24.6	5	Fe₂B
	0.27	0.17	0.06	9.9	39	(Fe_{0.55}B_{0.45})₉₅Nb₅
700°C/2h	0.10	0.18	0	27.6	11	A1(FePt)
	0.30	0.18	0.29	28	45	L1₀(FePt)
	0.12	0.18	0	22.8	5	Fe₂B
	0.29	0.18	0	10	39	(Fe_{0.55}B_{0.45})₉₄Nb₅

The estimated errors are: ± 0.02 mm/s for IS and QS/2 ε , ± 0.1 T for B_{hf} and ± 1 for the relative proportion

The relative intensities of cubic and tetragonal FePt are unbalanced. From these two, the tetragonal hard magnetic $L1_0$ seems to be the most intense phase in all samples.

For the annealing at 500_600°C the $\text{Fe}_{51}\text{Pt}_{27}\text{Nb}_2\text{B}_{20}$ ribbons have slightly higher relative intensities for the cubic $A1$ and tetragonal $L1_0$ FePt phase compared with the $\text{Fe}_{52}\text{Pt}_{28}\text{Nb}_2\text{B}_{18}$ ribbons annealed in the same conditions. Nevertheless, the total amount of the crystallized fraction (where we include both $A1$ and $L1_0$ phases) is the same as for $\text{Fe}_{52}\text{Pt}_{28}\text{Nb}_2\text{B}_{18}$ ribbons.

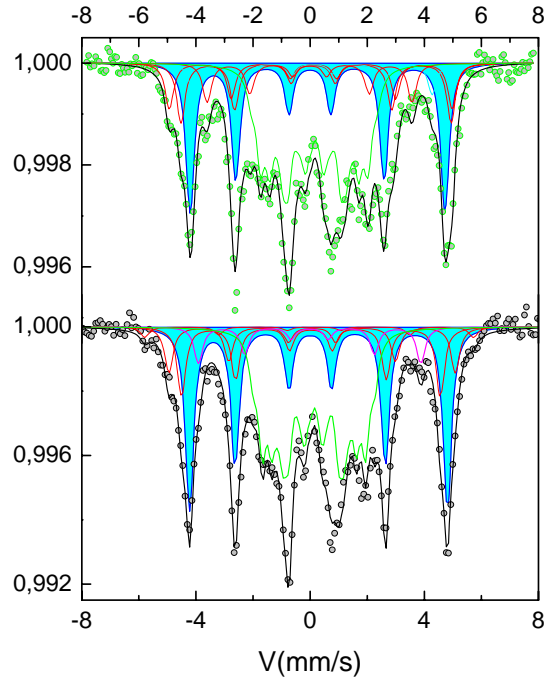


Figure 3.14. Fitted Mössbauer spectra of $\text{Fe}_{51}\text{Pt}_{27}\text{Nb}_2\text{B}_{20}$ (bottom) and $\text{Fe}_{52}\text{Pt}_{28}\text{Nb}_2\text{B}_{18}$ (top) ribbons annealed at 500°C_600°C together with their sublattices as identified by the fit. Blue highlighted component is the contribution due to $L1_0$ tetragonal FePt phase

If we compare the two samples at the same annealing conditions, 500°C_600°C, spectra plotted for comparison in Figure 3.14, we can say that the $\text{Fe}_{51}\text{Pt}_{27}\text{Nb}_2\text{B}_{20}$ ribbons (bottom) should have better hard magnetic properties than the $\text{Fe}_{52}\text{Pt}_{28}\text{Nb}_2\text{B}_{18}$ ribbons (top), since the relative intensity of the hard phase in the microstructure obtained after annealing is higher.

It can be seen that the relative intensity of the $L1_0$ phase, the area encompassed by the sextet highlighted in blue, is lower for the $\text{Fe}_{51}\text{Pt}_{27}\text{Nb}_2\text{B}_{20}$ ribbons. It has to be mentioned that the hyperfine parameters of the $A1$, $L1_0$ and disordered phases are highly

similar for the two compared spectra, as it can be seen in Tables XI and XII. Whilst the crystallization of tetragonal and cubic FePt phase occurs in the FePt – 2 sample directly from the disordered as-cast precursor, in the FePt – 1 sample, this process seems to occur partially via the metastable precursor Fe₃B, which at this annealing temperature, has a relative intensity of 7% in the FePt -1 while in the FePt – 2, this phase has not been indexed in the spectrum. Nevertheless, the most important difference between the two samples is provided by the average grain sizes, as revealed by TEM. As the grain size is smaller in the FePt – 1 sample, this has more chance to provide a suitable hard-soft microstructure with exchange coupled grains.

Maximum relative intensity of the hard magnetic phase is obtained for the samples annealed at 700°C and this is in agreement with the magnetic results, as we will point out in the following section.

The detailed Mössbauer spectra analysis results confirm the XRD data and prove furthermore the coexistence of the hard magnetic *L1*₀ FePt with soft magnetic phases in a refined grain microstructural arrangement. The effect of such refined grain microstructure consisting of hard magnetic *L1*₀ grains, alternatively disposed with *A1* soft magnetic grains, and a disordered residual FeB-rich phase, on the magnetic properties of the annealed ribbons, will be pointed out in the next Section.

Chapter 4:

Magnetic properties of the $\text{Fe}_{51}\text{Pt}_{27}\text{Nb}_2\text{B}_{20}$ and $\text{Fe}_{52}\text{Pt}_{28}\text{Nb}_2\text{B}_{18}$ annealed ribbons. Exchange spring effects and energy product for exchange coupled magnets.

4.1. Hysteresis loops for the $\text{Fe}_{51}\text{Pt}_{27}\text{Nb}_2\text{B}_{20}$ and $\text{Fe}_{52}\text{Pt}_{28}\text{Nb}_2\text{B}_{18}$ annealed ribbons.

Hysteresis loops at 5 K and 300 K, in parallel and perpendicular applied field have been recorded for all the annealed $\text{Fe}_{51}\text{Pt}_{27}\text{Nb}_2\text{B}_{20}$ and $\text{Fe}_{52}\text{Pt}_{28}\text{Nb}_2\text{B}_{18}$ ribbons. The measurements were taken with a SQUID operating with applied field up to 5.5 T at temperatures of 5 K and 300 K. SQUID measurements were performed at the Université de Rennes.

4.1.1. $\text{Fe}_{51}\text{Pt}_{27}\text{Nb}_2\text{B}_{20}$ annealed ribbons

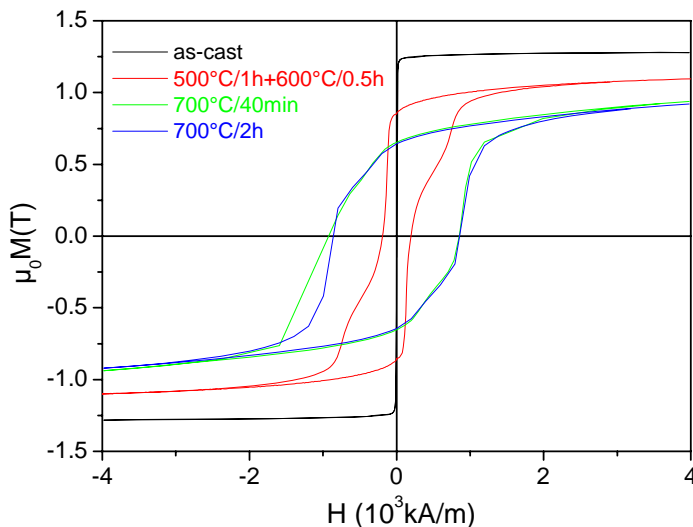


Figure 4.1: 300K Hysteresis loops for as-cast and annealed $\text{Fe}_{51}\text{Pt}_{27}\text{Nb}_2\text{B}_{20}$ ribbons in parallel field

The hysteresis loops for the as-cast and annealed $\text{Fe}_{51}\text{Pt}_{27}\text{Nb}_2\text{B}_{20}$ ribbons, recorded at 300 K with magnetic field applied parallel to the ribbons plane, are plotted in Figure 4.1. The loop for the as-cast ribbons is typical for soft ferromagnets. The magnetization saturates almost immediately after applying a small magnetic field. The saturation reaches 1.3 T while the loop shows very low hysteresis (around 30 mT).

The sample annealed at 500°_600°C shows completely different behavior. The magnetization has a slower approach to saturation than in the as-cast state. This may be explained by the presence of a significant fraction of hard $L1_0$ grains. The value of the maximum magnetization is about 15% lower than that of the as-cast sample, reaching about 1.1 T. Upon decreasing the field, a large value of remanent magnetization is noticed, as is the case for hard magnetic materials. The remanence observed in this case is 0.85 T, which gives a remanent-to-saturation ratio of about 0.77.

By applying negative fields the magnetization drops rapidly to zero giving rise to a small coercivity value of 194 kA/m. It must be noticed that the hysteresis loops show two inflection points on each branch, completely retrievable and symmetrical on the other branch. Such behavior of the hysteresis is usually encountered in hard – soft magnetic bilayers. When the negative applied fields start to be applied, the soft magnetic moment reorient faster than the hard magnetic moments, if the hard and soft magnetic grains are not fully exchange coupled. This would give rise to the inflection point in the hysteresis loop. The small value of coercivity is a proof that the soft magnetic phases are predominant in the sample, at this annealing stage.

The second point of inflection which occurs at negative fields larger than the coercive field proves that the reversal of hard magnetic moments occur after the soft magnetic ones have already reversed, in the quadrant with negative magnetization. The switching field for the soft phase is about 39 kA/m. As stated before, at this stage of annealing the soft magnetic grains are predominant in the sample and the coercivity is rather low, even if the remanence-to-saturation ratio is at values comparable with good permanent magnets. Therefore, these inflection points show the existence of two magnetic phases, one hard, the other soft, that are not completely exchange coupled.

The sample annealed at 700°C for 40 minutes shows a different aspect, with the hysteresis loop opened even more. The magnetization has same slow approach to saturation as in the previous case and the maximum magnetization is 0.9 T. The remanent magnetization is in this case 0.63 T thus giving a remanence-to-saturation ratio of about 0.7.

The shape of the hysteresis loop with two inflection points is preserved also in this case, but here the hard magnetic phase is predominant and the exchange coupling

between the hard and the soft magnetic phases is more effective. Therefore, the coercive field is extremely high, comparing with the annealing at 500_600°C. The coercivity reaches in this case 847 kA/m, more than 3 times increased, comparing with the annealing at 500_600°C. The switching field of soft magnetic phase is smaller than the coercive field, which indicates a better exchange coupling between the grains. The value for the switching field is 155 kA/m for the soft magnetic grains, increasing substantially compared with the annealing at 500_600°C.

The sample annealed at 700°C for 2h presents almost similar hysteresis loop as the sample annealed at the same temperature for 40 minutes. While the coercivity is slightly higher than before (877 kA/m), the remanent and the maximum magnetization are almost identical to the previous annealing with a remanent-to-saturation ratio of about 0.7. The energy product for all the samples is calculated using the B-H loops, not shown here. The highest $(BH)_{\max}$ values of 64 kJ/m³ are obtained for the two samples annealed at 700°C. All the magnetic parameters obtained for these samples at 300 K in parallel field are depicted in Table XIII.

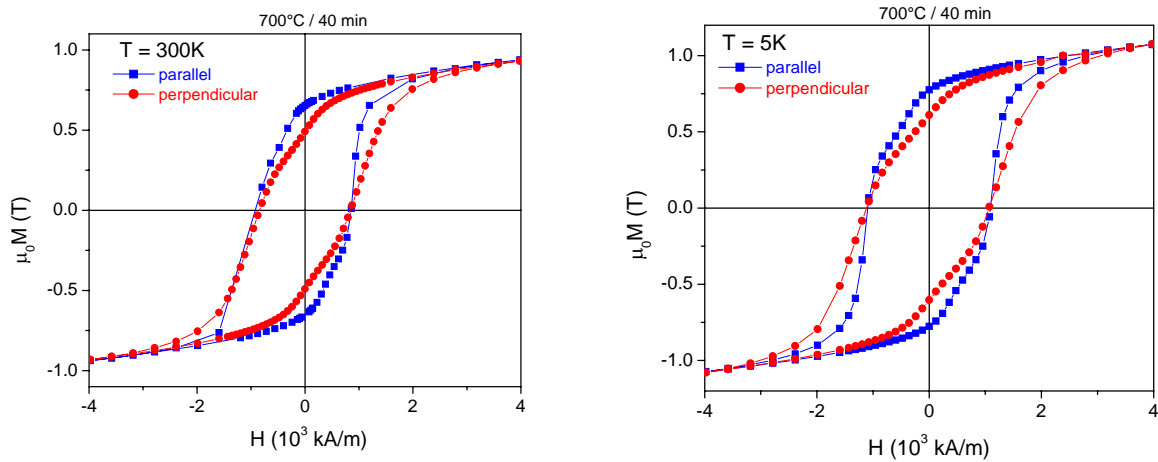


Figure 4.2: Hysteresis loops at 300K and 5K for Fe₅₁Pt₂₇Nb₂B₂₀ annealed samples at 700°C/40 min in parallel and perpendicular field

Table XIII. Magnetic parameters obtained for FePt – 2 annealed samples at 300 K in parallel field

Annealing conditions	H _c (kA/m)	μ ₀ M _S (T)	μ ₀ M _r (T)	M _r /M _s	(BH) _{max} (kJ/m ³)
500°C/1h 600°/0.5h	194	1.1	0.85	0.77	61
700°C/40min	847	0.9	0.63	0.70	64
700°C/2h	877	0.9	0.63	0.70	64

The same hysteresis loops were also recorded in perpendicular applied field and at 5 K. As the thermal fluctuations are reduced we witness an increase of all magnetic parameters, as expected. Figures 4.2 – 4.3 show the samples annealed at 700°C for 40 min and 2h in both perpendicular and parallel applied field.

At 5 K the loops preserve the same shape with enhanced coercivity and large saturation and remanent magnetization values. In parallel applied field the saturation magnetization reaches 1.1 T and the remanence 0.8 T, while in perpendicular field the saturation has about the same value and the remanence is decreased to 0.6. Nevertheless, the coercivity is strongly enhanced (1140 kA/m) comparing with that at 300K, and is the same in both parallel and perpendicular applied fields. Both at 5K and at 300 K the saturation magnetization for the perpendicular applied field is similar to the one for parallel applied field. This means that there is no significant out-of-plane component of the magnetocrystalline anisotropy and the grain magnetizations are randomly oriented.

The FePt – 2 sample annealed at 700°C for 2 hours shows similar behavior. Both at 5 K and 300 K (Figure 4.3), the saturation magnetization is again similar in the loops recorded with perpendicular and parallel applied field. While the coercivity remains the same for the two different orientations, being higher for the 5K loop (around 1140 kA/m), the remanence decreases from 0.63 to 0.5 T for perpendicular applied field at both temperatures.

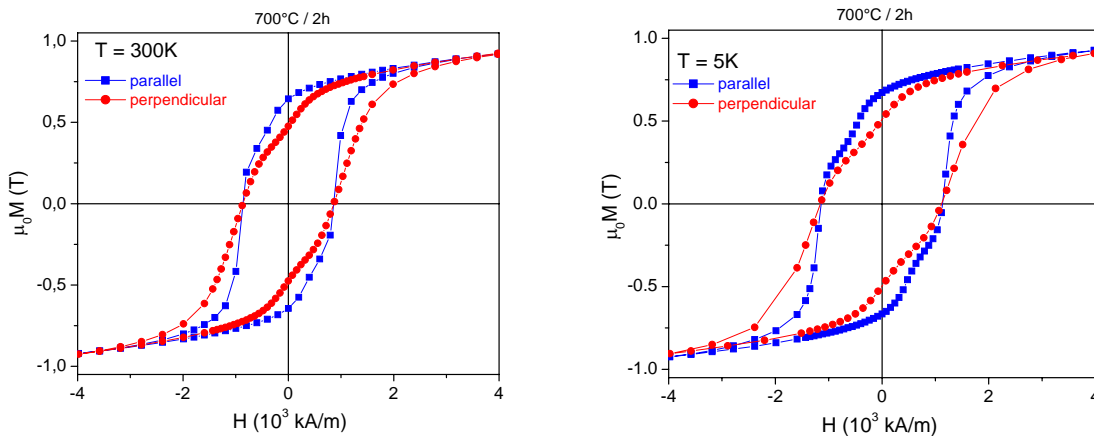


Figure 4.3: Hysteresis loops at 5K and 300K for Fe₅₁Pt₂₇Nb₂B₂₀ samples annealed at 700°C/2h

4.1.2. $Fe_{52}Pt_{28}Nb_2B_{18}$ annealed ribbons

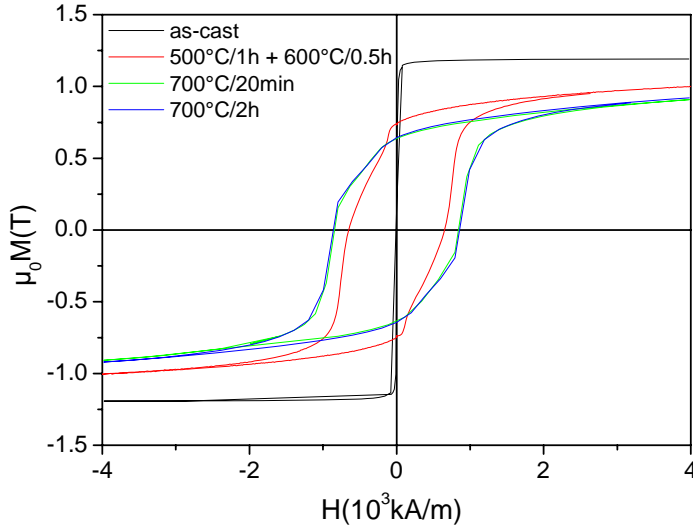


Figure 4.4: Hysteresis loops for as-cast and annealed samples $Fe_{52}Pt_{28}Nb_2B_{18}$

In the case of FePt – 1 annealed samples, the hysteresis loops recorded for the as-cast and the annealed samples in parallel field at 300 K are plotted in Figure 4.4. All the magnetic properties of the samples at 300K in parallel field are depicted in Table XIV. As in the previous case, the as-cast sample shows typical soft magnetic behavior with saturation magnetization of 1.2 T and very low coercive field of only 10 mT.

Among the annealed samples, the 500°C_600°C annealing show the highest saturation magnetization of 1 T. This is due to the small grain size and also due to the high fraction of soft phases, as seen in the Mössbauer study. The two inflection points are again observable, as a sign that the hard and soft phases are not fully exchange coupled. Switching field of the soft phase is about 140 kA/m, higher than in the FePt – 2 sample in the same annealing conditions. This may be explained by the fact that smaller grain size was determined for the microstructure of the FePt-1 than for FePt-2 sample, as proved by TEM. Since the grains are smaller, a better coupling among grains is possible and the switching field would be higher. The coercive field is 645 kA/m and the remanence reaches about 0.75.

As the annealing temperature increases up to 700°C the saturation magnetization diminishes while the coercivity increases. The two FePt – 1 samples annealed at 700°C for 20 minutes and 2 hours, respectively, show almost identical hysteresis loops. The inflection points in the demagnetization quadrant are still visible. The highest coercivity (858 kA/m) is reached for the annealing at 700°C for 2 hours while the $(BH)_{\max}$ is about kJ/m^3)

In Figures 4.5, a comparison between the two samples annealed at 500°C_600°C is shown. It can be seen that while the saturation magnetization is higher in the case of FePt – 2 sample, the FePt – 1 sample has sensibly higher coercivity than the FePt – 2 sample. This feature is consistent with the TEM observations where large difference in the grain sizes was observed.

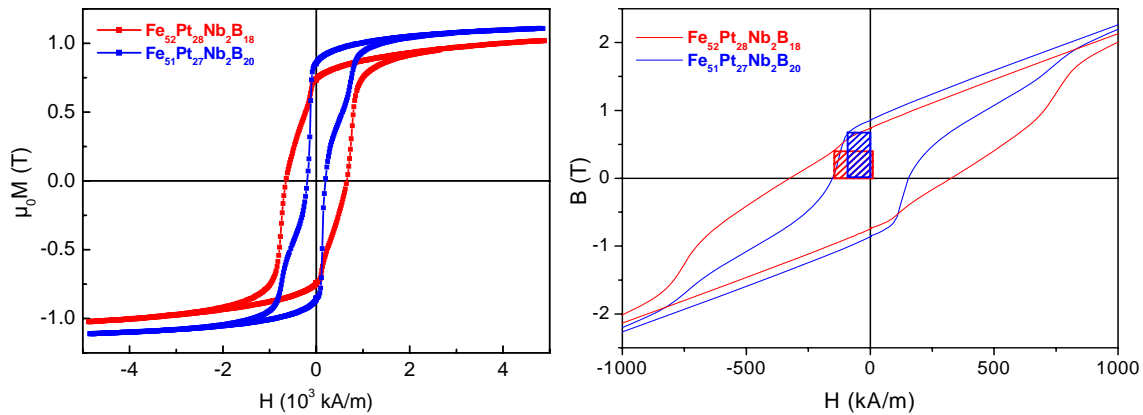


Figure 4.5 300K hysteresis loops for $\text{Fe}_{51}\text{Pt}_{27}\text{Nb}_2\text{B}_{20}$ and $\text{Fe}_{52}\text{Pt}_{28}\text{Nb}_2\text{B}_{18}$ samples annealed at 500°C/1h 600°/0.5h. Left: M-H, Right: B-H loops.

It is expected that due to the smaller coercivity, the energy product should also be smaller in the case of FePt – 2 sample. But in the B-H loops, the difference in the coercivity is less important in the calculation of $(BH)_{\max}$ as is the squareness of the loop, as it is shown in Figure 4.5 right. Therefore, even if the coercive field is much smaller in FePt – 2, the $(BH)_{\max}$ shown as the shaded areas in this Figure are almost similar, even slightly higher for FePt – 2 (see also the values depicted in Tables XIII and XIV).

The 5 K and 300 K hysteresis loops of FePt – 1 samples annealed at 700°C for 20 minutes and 2 hours, in both parallel and perpendicular applied field are shown in Figures 4.6 and 4.7. At 5 K, a maximum coercivity of 1090 kA/m and a saturation magnetization of 0.96 are reached for the sample annealed at 700°C for 20'. For the sample annealed at 700°C for 2 hours, the maximum coercivity was 1107 kA/m and the saturation magnetization was about 0.97 T. In both figures the perpendicular and parallel loops are also quite similar, as in the case of FePt – 2 samples. Also, in both figures there is a decrease of remanence for the perpendicular applied field, implying that there is a slight in-plane preferential orientation of the grain magnetization in all samples.

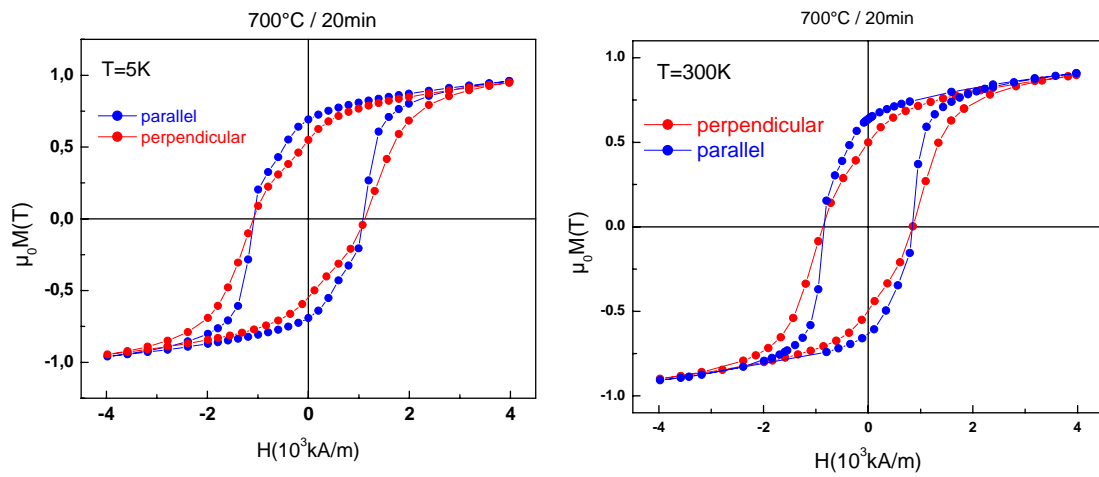


Figure 4.6: Hysteresis loops at 5K and 300K for $\text{Fe}_{52}\text{Pt}_{28}\text{Nb}_2\text{B}_{18}$ samples annealed at 700°C/20 min

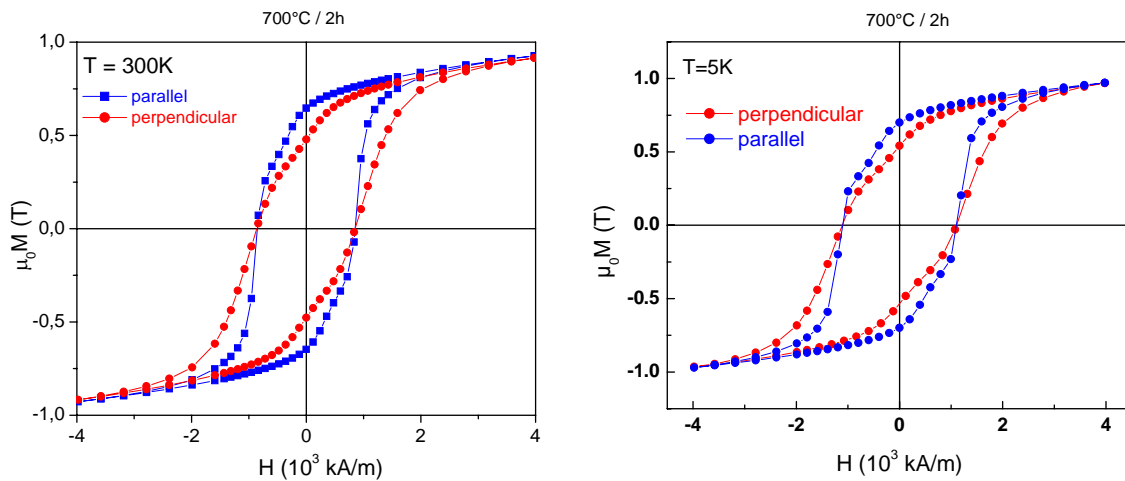


Figure 4.7: Hysteresis loops at 5K and 300K for $\text{Fe}_{52}\text{Pt}_{28}\text{Nb}_2\text{B}_{18}$ samples annealed at 700°C/2 hours

Table XIV. Magnetic parameters obtained for FePt – 1 annealed samples at 300 K in parallel field

Annealing conditions	H _c (kA/m)	$\mu_0 M_S$ (T)	$\mu_0 M_r$ (T)	M_r/M_s	$(BH)_{max}$ (kJ/m ³)
500°C/1h 600°/0.5h	645	1	0.75	0.75	60
700°C/20min	840	0.92	0.63	0.68	64
700°C/1h	820	0.95	0.65	0.68	69
700°C/2h	858	0.92	0.64	0.69	59

As seen in Table XIV, the best values for the energy product and coercivity in the annealed samples at 700°C for 20 (or 40) minutes and 2 hours were around 64 kJ/m³ and 858 kA/m, values that are comparable with those reported until now in FePt-based alloys. This achievement has yet to be improved since we have seen that the magnetic loops still have the inflection points that witness a non-complete exchange coupling for the hard and soft magnetic phases. Besides, it is also necessary to check for the fulfilling of the exchange spring magnet criteria, as established in the first Chapter. This will be done in the following.

4.2. The exchange spring magnets criteria. Reversibility effects.

Some of the criteria established for an exchange spring magnet, since the early works of Kneller and Hawig [16] and Skomski and Coey [17] are the following:

- the hard and soft phases must emerge from a common metastable precursor,
- the hysteresis loop must show reversibility in any point of the demagnetization curve,
- the hard and soft grains must be suitably dispersed, and their sizes have to be of the same order as the exchange correlation length,
- complete exchange coupling must be ensured in order to avoid pinning effects.

We have shown by a number of different experimental techniques that in our samples, the hard and soft magnetic phases emerge from the same metastable precursor that is crystallographically compatible with the crystallization products.

We have documented the refined grain microstructure, with grains dispersed / embedded in soft magnetic matrix and the grain sizes for the annealing of interest were as low as 16-30 nm.

We need to show the reversibility of the demagnetization curve.

We need to ensure full exchange coupling, i.e to ensure demagnetization curves where the magnetization reversal shall occur simultaneously without the observed inflection points that witness differences in the switching fields of the hard and soft phases.

We have measured the hysteresis loop for the $\text{Fe}_{52}\text{Pt}_{28}\text{Nb}_2\text{B}_{18}$ samples annealed at $500^\circ\text{C}/1\text{h}$ $600^\circ\text{C}/0.5\text{h}$ and in three points on the descending branch we have performed reversibility curves both at 300K and 5K. These measurements, plotted in Figure 4.8, show that the hysteresis loop is fully reversible both at 5K and 300K and the coercivity is indeed caused by a strong hardening of the samples due to exchange coupling effects between hard and soft magnetic grains.

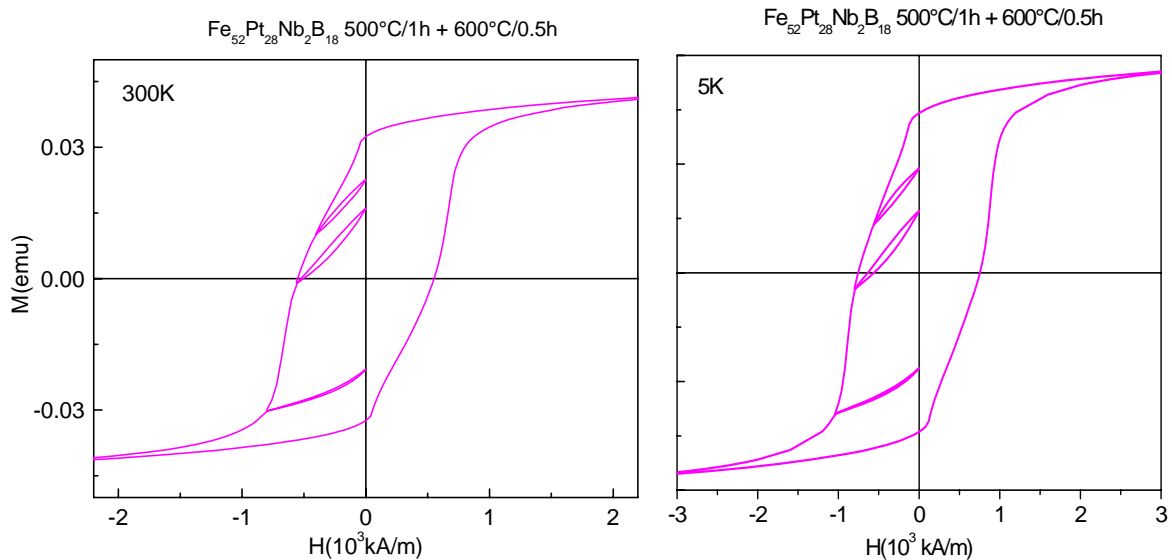


Figure 4.8: Reversibility curves at 300K and 5K for $\text{Fe}_{52}\text{Pt}_{28}\text{Nb}_2\text{B}_{18}$ annealed samples at $500^\circ\text{C}/1\text{h}$ $600^\circ\text{C}/0.5\text{h}$

We have performed one final annealing treatment on the FePt – 1 alloy. This annealing has been done for 1 hour at 700°C with a heating rate of 5 K/min. The annealing time was set to be in between the 20 min and 2 h of the precedent annealing. We have measured the hysteresis loops of the obtained sample in same conditions. They are plotted in Figure 4.9. The hysteresis loop has showed this time no inflection point on both branches of the loop. The right image is the magnification of the descending part of the branch where one can observe the smooth descent without any inflection.

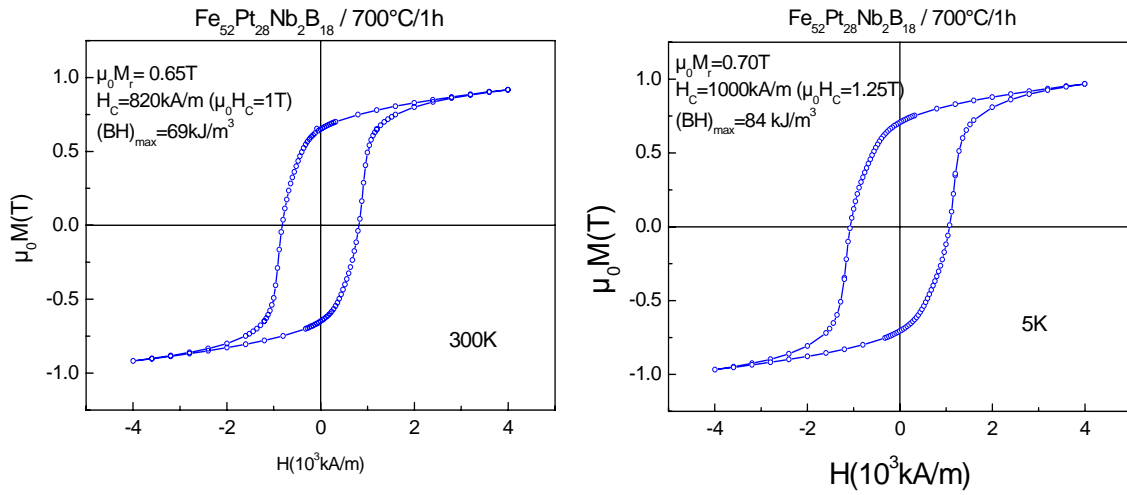


Figure 4.9 Hysteresis loops of $\text{Fe}_{52}\text{Pt}_{28}\text{Nb}_2\text{B}_{18}$ sample annealed at $700^\circ\text{C}/1\text{h}$

It means that at this annealing the hard and soft magnetic grains existent in the microstructure are completely exchange coupled and the energy product and the other magnetic parameters are optimized. As it can be seen, the energy product for this last sample has reached at 300 K a maximum among all the other investigated samples of 69 kJ/m^3 (see Table XIV) while at 5K the sample exhibits a coercive field of 1000 kA/m and 84 kJ/m^3 for the energy product.

For certifying the existence and quantifying the magnitude of the magnetic interactions between hard- and soft-magnetic phases, one of the most suitable technique is based on the so-called Henkel plots. [83]. The Henkel plot is employed to quantify the strength of the exchange coupling between magnetic entities (grains, layers, regions) in magnetic materials. A brief explanation of this technique is provided below.

On the initial magnetization curve, the measurement is stopped at various intermediate applied field, the field is suddenly removed and the remanence at that intermediate field is measured. These values are noted m_r . After several determinations and a series of $m_r(H)$ values is obtained, the procedure is repeated, this time on the demagnetization curve. After applying negative fields and sudden removal, the remanence at demagnetization m_d is measured. After several determinations, a series of $m_d(H)$ values is obtained. Wohlfarth [84] concluded from the experimental data the experimental relation linking the two sets of data: $m_d(H) = 1 - 2m_r(H)$ where m_d is the

remanence measured upon applying negative field on the demagnetization curve, and m_r is the remanence measured upon applying positive field, on the initial magnetization. Henkel [83] developed this relation by plotting the curve of $m_d(H)$ vs $m_r(H)$. Any deviations from the idealized straight line are interpreted as being due to interactions. Mayo et al. [85] improved this technique by plotting $\Delta m = m_d - (1 - 2m_r)$ as a function of the applied field. It is known that non-interacting systems in general show linear Henkel plots, while interacting systems show curved plots [86]. If Δm has positive value on the whole applied field interval, it is considered a proof of intergrain exchange coupling while the negative values are a sign of the existence of dipolar interactions. The decrease of intergrain exchange coupling results in the drop of the value of Δm .

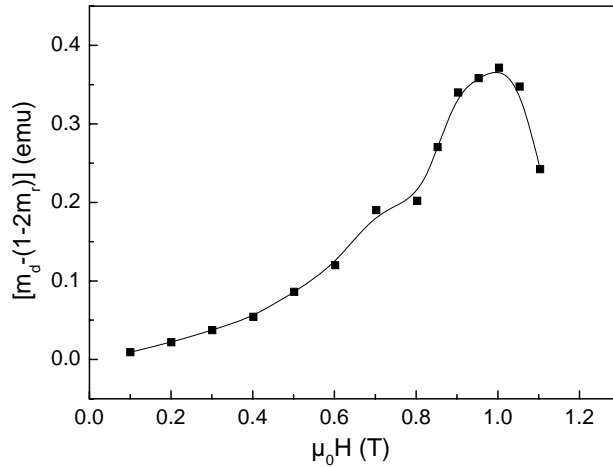


Figure 4.10: The $m_d - (1 - 2m_r)$ vs. $\mu_0 H$ Henkel plot for the FePt – 1 sample annealed at 700°C for 1h.

We have determined m_r and m_d remanence values for several applied fields in the range 0.1 – 1.1 T for the FePt – 1 sample annealed at 700°C for 1h and we have plotted in Figure 4.10 $m_d - (1 - 2m_r)$ as a function of the applied field. It can be seen that all the Δm values are positive for the investigated range, with a maximum for an applied field of 1T. This fact proves that in our sample, the hard and soft grains are coupled via exchange interactions. This confirms the other magnetic findings, presented up to here.

By this, we have proved the full coupling by exchange interactions of the hard and soft phases, we have checked all the criteria for an exchange spring magnet, as mentioned above, and we have optimized both the composition and the annealing procedures for obtaining values for the energy products and other magnetic parameters in view of applications of such materials as the future class of exchange coupled nanocomposite magnets.

Conclusions

The present work is aimed to substantially contribute to the development of high-performance FePt-based permanent magnets. More precisely, the coexistence of the hard magnetic, highly anisotropic $L1_0$ FePt with the soft magnetic A1 and $L1_2$ FePt phases, phases emerged from the same metastable precursor and therefore crystallographically coherent, obtained after carefully chosen annealing procedures, has been shown to lead to a potential exchange coupled nanocomposite magnet, with high chemical stability and suitable for high temperature technological applications.

Based on consideration linked to an appropriate hard/soft relative proportion needed for optimal magnetic properties and to the possibility of obtaining the desired phases if the composition is chosen to be in the region where $L1_0$ phase is formed, we have conceived 5 different alloys synthesized by the melt spinning method. These alloys have been deeply analyzed by means of a large range of experimental techniques: X-ray diffraction, transmission electron microscopy and electron diffraction, energy dispersion spectroscopy, differential scanning calorimetry, *in situ* temperature and pressure-dependent X-ray diffraction of synchrotron radiation, Mössbauer spectrometry, SQUID and vibrating sample magnetometry for the determination of magnetic properties.

The as-cast state of the alloys has been shown to be crucial to the development, after appropriate annealing of the desired microstructure of alternatively disposed hard and soft magnetic nanosized grains. Among the 5 studied alloys, two Fe-rich alloys casted in an already crystalline state were shown to be not suitable for exchange coupled nanocomposite magnets, since their structure did not change with annealing and the FePt phase transformation with formation of the hard magnetic fraction did not occur. On the contrary, the 3 other alloys, where the as-cast state was shown to be disordered, developed after appropriate annealing the desired co-existence of hard and soft magnetic phases with refined grain sizes and good properties as permanent magnets.

The formation and evolution of the crystalline phases from the as-cast precursor were investigated by using differential calorimetry as well as a unique tool, the *in situ* temperature-dependent and pressure-dependent X-ray diffraction of synchrotron radiation, a highly original approach, never used before for the FePt-based nanocomposite magnets. We have been able to estimate, based on these results, the

temperature and activation energy of the phase transformation and the range of temperatures where hard and soft magnetic phases coexist, and we monitored the evolution of these phases as crystallization products emerged from the same precursor.

The application of a small pressure the formation of $L1_0$ phase may be promoted even in sample *2a* which does not change with temperature, in conventional annealing procedures.

Based on these results, we have performed annealing procedures using information obtained during the thermal analysis study and the annealed samples have been investigated with all suitable characterization techniques described above. The most promising alloys were proven to be the two Pt-rich compositions where a microstructure with nanograins smaller than 30 nm, of hard and soft magnetic nature, alternatively dispersed in a homogeneous and uniform manner, was obtained, as proven by the TEM observations and the formation of $L1_0$ hard magnetic phase was documented using XRD, MS and magnetic measurements.

The hyperfine parameters of the $L1_0$, A1 and $L1_2$ phases, observed in these alloys were obtained with accuracy and are consistent along the whole range of annealing conditions. In order to accurately obtain the hyperfine parameters of each of the FePt phase involved we have synthesized and analyzed three other binary alloys of compositions: Fe_3Pt , FePt and $FePt_3$. Based on these results the schematics of phase transformation and phase evolution in various annealing stages were precisely derived and explained.

For the first time, a quantitative analysis of the phase composition was obtained at each annealing stage. Using Mössbauer spectrometry we have been able to correctly determine the relative abundance of hard magnetic tetragonal $L1_0$ phase as well as of the soft magnetic cubic FePt and tetragonal Fe₂B phases. Also, the relative abundance and the correct composition were found for the residual intergrain phase which has been proven to be FeB-based.

The magnetic properties of the most promising alloys were exhaustively studied using both MS and vibrating sample magnetometry (VSM) at 300K and 5K. We have shown that large values of coercivity, associated with high saturation magnetization and enhanced remanence are obtained for annealing treatments ranging between 500/600°C

and 700°C, with an optimum of these parameters and of the calculated maximum energy product at about 700°C annealing temperature.

Moreover, we have checked the well established criteria for an exchange spring magnet. We have observed the complete reversibility of the hysteresis loop. Moreover, we have shown that for an annealing at 700°C for 1 hour, in the two Pt-rich samples, the demagnetization part of the hysteresis loops, does not exhibit anymore the inflection points: that signifies the two-phase behavior of the hard-soft grain mixture. The disappearance of this inflection point is the proof that the hard and soft magnetic grains are fully exchange coupled. Henkel plots were used in order to prove the existence of intergrain exchange coupling. By this we were able to prove that we have built a truly exchange spring magnet with optimal magnetic properties. At room temperature, these optimal properties were: maximum energy product of about 70 kJ/m³, coercivity of about 860 kA/m, saturation magnetization of about 1.1 T and remanence-to-saturation ratio of 0.8. The optimal properties in our samples were found for samples where the hard magnetic L1₀ phase has a relative abundance of 40-45%.

In this way, the present work is aimed to bring a clear advancement in the field of FePt-based intermetallic alloys and may be seen as a breakthrough in the search for a future class of exchange spring nanocomposite magnets, corrosion resistant and stable at high temperatures, as in the case of the investigated FePtNbB alloys.

Perspectives

The present work opens a wide range of potential research aimed to better understand the mechanisms of further optimization of the desired magnetic properties.

The evolution of the microstructure and the phase composition have yet to be studied in a wider range of annealing parameters. It is possible to prove that indeed the microstructure of hard and soft magnetically coupled grains is stable at higher temperatures, as it has been inferred from our synchrotron XRD studies. The high-temperature annealing has to be performed in accordance with the schematics of phase transformation that we have derived.

A more detailed compositional study is required having as starting point the optimal compositions found in the present work. Inclusion of small amount of magnetic

elements such as Co, aimed at increasing the uniaxial anisotropy of the hard phase may be envisaged for a future work.

Moreover, more detailed study of the nature and strength of the magnetic interactions among the hard and soft magnetic grains is needed, in a conjugated effort to understand the interplay between the optimized microstructure with refined grain sizes and the optimal magnetic properties, and to understand the intrinsic mechanisms that lead to enhanced coercivity and energy products in these alloys.

The pursue of the *in situ* studies of the effects of dynamic annealing and of the applied pressure in the activation of the disorder-order phase transformation that has as effect the occurrence of hard magnetic $L1_0$ grains with well-controlled sizes, is also a potential direction of research with wide perspectives for deepening the knowledge acquired in this study about the formation and evolution of the crystallization products and schematics of phase transformation in various stages of annealing.

Also, studies of the behavior of these magnets in reactive media are aimed to prove the high resistance to the corrosion in view of potential technological applications as permanent magnets.

Compaction of these annealed ribbons followed by high temperature sintering will be needed, as a prerequisite for bringing the FePtNbB alloys in the phase of potential applications, but the effects of these procedures on the hard-soft microstructure are not yet studied, a wholly different research direction being envisaged for studies of the impact on the microstructure and ultimately on the magnetic properties.

Altogether, these future research efforts will aim at a substantial advancement of the global knowledge in the field of exchange-coupled nanocomposite magnets, based on FePt and moreover, will serve as a departure point for possible technological applications in fields where performant magnets stable at high temperatures are required.

References:

- [1] H. Kronmüller and J.M.D. Coey, "Magnetic Materials", in European White Book on Fundamental Research in Materials Science, Max-Planck-Gesellschaft (2000), 92-96.
- [2] S. Sun, C.B. Murray, D. Weller, L. Folks, A. Moser, *Science* **287** (2000) 1989.
- [3] M. Chen and D.E. Nikles, *Journal of Applied Physics* **91** (2002) 8477.
- [4] V. Skumryev, S. Stoyanov, Y. Zhang, G. Hadjipanayis, D. Givord, J. Nogues, *Nature* **423** (2003) 850.
- [5] G.A. Prinz, *Science* **282** (1998) 1660
- [6] H. Presting, U. König, *Materials Science and Engineering C* **23** (2003) 737.
- [7] C.A. Berven, M.N. Wybourne, L. Longstreth, J.E. Hutchison, *Physica E* **19** (2003) 246.
- [8] Hilger I, Kiessling A, Romanus E, Hiergeist R, Hergt R, Andra W, Roskos M, Linss W, Weber P, Weitschies W and Kaiser W A *Nanotechnology* **15** (2004) 1027.
- [9] P. Tartaj, M. del Puerto Morales, S. Veintemillas-Verdaguer, T. González-Carreño, C.J. Serna, *Journal of Physics D: Applied Physics* **36** (2003) R182
- [10] J.M.D. Coey, *Journal of Magnetism and Magnetic Materials* **248** (2002) 441-456.
- [11] G.C. Hadjipanayis, *Journal of Magnetism and Magnetic Materials* **200** (1999) 373-391.
- [12] F. Weitzer, K. Hiebl, P. Rogl, *Journal of Applied Physics* **69** (1991) 7215.
- [13] R.A. Dunlap, Z. Wang, M. Foldeaki, *Journal of Applied Physics* **76** (1994) 6737.
- [14] J.-L. Wang, F. Yang, N. Tang, X.-F. Han, H.-G. Pan, J.-F. Hu, *Journal of Applied Physics* **79** (1996) 2012.
- [15] W.-Z. Li, N. Tang, J.-L. Wang, F. Yang, Y.W. Zeng, J.J. Zhu, F.R. de Boer, *Journal of Applied Physics* **76** (1994) 6743.
- [16] E.F. Kneller, R. Hawig, *IEEE Transactions on Magnetics* **27** (1991) 3588.
- [17] R. Skomski, J.M.D. Coey, *Physical Review B* **48** (1993) 15812.
- [18] R. Coehoorn, D.B. de Mooij, C. de Waard, *Journal of Magnetism and Magnetic Materials* **80** (1989) 101.
- [19] Y.Q. Wu, D.H. Ping, K. Hono, M. Hamano, A. Inoue, *Journal of Applied Physics* **87** (2000) 8658.
- [20] T. Zhao, Q.F. Xiao, Z.D. Zhang, M. Dahlgren, R. Grossinger, K.H.J. Buschow, F.R. de Boer, *Applied Physics Letters* **75** (1999) 2298.
- [21] V. Kuncser, M. Valeanu, F. Lifei, D. Predoi, P. Palade, G. Schinteie, O. Crisan, G. Filoti, *Journal of Magnetism and Magnetic Materials* **272** (2004) 797.

- [22] L. Schulz, K. Schnitzke, J. Wecker, M. Katter, C. Kurth, *Journal of Applied Physics* **70** (1991) 6339.
- [23] E.E. Fullerton, J.S. Jiang, C.H. Sowers, J.E. Pearson, S.D. Bader, *Applied Physics Letters* **72** (1997) 380.
- [24] T. Goto, H. Utsugi, K. Watanabe, *Hyperfine Interactions* **54** (1990) 539.
- [25] Y.V. Baldokhin, P.Y. Kolotyarkin, Y.I. Petrov, E.A. Shafranovsky, *Journal of Applied Physics* **82** (1997) 3042.
- [26] H. Zeng, J. Li, J. P. Liu, Z. L. Wang, S. Sun, *Nature* **420** (2002) 395.
- [27] C-B Rong, V Nandwana, N Poudyal, Y Li, J Ping Liu, Y Ding Z Lin Wang, *Journal of Physics D: Applied Physics* **40** (2007) 712
- [28] J. Lyubina, K. Khlopkov, O. Gutfleisch, K.-H. Müller, L. Schultz, *Journal of Applied Physics* **99** (2006) 08E903.
- [29] J. Lyubina, K. Khlopkov, O. Gutfleisch, K.-H. Müller, L. Schultz, *Journal of Applied Physics* **95** (2004) 7474
- [30] X. Rui, J.E. Shield, Z. Sun, L. Yue, Y. Xu, D.J. Sellmyer, Z. Liu, D.J. Miller, *Journal of Magnetism and Magnetic Materials* **305** (2006)76-82
- [31] J.A. Christodoulides, M.J. Bonder, Y. Huang, Y Zhang, S. Stoyanov, G.C. Hadjipanayis, A. Simouopoulos, D. Weller, *Physical Review B* **68** (2003) 054428
- [32] S. Simizu R.T. Obermyer, B. Zande, V.K. Chandhok, A. Margolin, S.G. Sankar, *Journal of Applied Physics* **93** (2003) 8134
- [33] J.P. Liu, CP. Luo, Y;Liu, D.J. Sellmyer, *Applied Physics Letters* **72** (4) (1998) 483
- [34] K.Inomata, T.Sawa, S.Hashimoto, *Journal of Applied Physics* **64** (1988) 2537
- [35] W Zhang, K Yubuta, P Sharma, A. Makino, A Inoue, *Journal of Applied Physics* **101** (2007) 09K518
- [36] W Zhang, K Yubuta, P Sharma, A Inoue, *Journal of Applied Physics* **99** (2006) 08E914
- [37] W Zhang, P Sharma, K Shin, D-V Louzguine, A Inoue, *Scripta Materialia* **54** (2006) 431
- [38] A. Inoue, W. Zhang, *Journal of Applied Physics* **97** (2005) 10H308.
- [39] W. Zhang, D.V. Louzguine, A. Inoue, *Applied Physics Letters* **85** (2004) 4998.
- [40] E. Bruck, Q.F. Xiao, P.D. Thang, M.J. Toonen, F.R. de Boer, K.H.J. Buschow, *Physica B* **300** (2001) 215.
- [41] A. Makino, T. Bitoh, A. Inoue, Y. Hirotu, *Journal of Alloys and Compounds* **434** (2007) 614
- [42] A. Makino, T. Bitoh, M. Nagagawa, *Journal of Non-Crystalline Solids* **353** (2007)
- [43] A. Makino, T. Bitoh, A. Inoue, Y. Hirotu, *Materials Science and Engineering A* **449** (2007) 66

- [44] A. Makino, T. Bitoh, *Journal of Applied Physics* **95** (2004) 7498.
- [45] T. Bitoh, A. Makino, M. Nagagawa, *Journal of Applied Physics* **97** (2005) 10H307
- [46] O. Gutfleisch, J. Lyubina, K.-H. Müller, L. Schultz, *Advanced Engineering Materials* **7** (2005) 208
- [47] D. McKie, M. McKie, *Crystalline Solids*, Thomas & Sons, (1974) 337
- [48] Y. Yoshizawa, S. Oguma, and K. Yamauchi, *Journal of Applied Physics* **64**, (1988) 6044
- [49] G. Herzer, *IEEE Trans. Magn.*, **25** (1989) 3327
- [50] G. Herzer, *IEEE Trans. Magn.*, **26** (1990) 1397
- [51] J.M. Greneche, *Hyp. Int.*, **110** (1997) 81
- [52] A. Slawska-Waniewska, M. Gutowski, H.K. Lachowicz, T. Kulik, H. Matyja, *Phys. Rev. B* **46** (1992) 14594
- [53] G. Herzer, *J. Magn. Magn. Mater.* **157/158** (1996) 133
- [54] V.I. Goldanskii, R.H. Herber, eds, *Chemical Applications of Mössbauer Spectroscopy*, Acad. Press (1968) 24
- [55] F. Varret, J. Teillet, *Unpublished Mosfit Program*, Universite du Maine, France
- [56] <http://www.ing.unitn.it/~maud/>
- [57] K. Syassen, Datlab, unpublished software, *Max-Planck Institute for Solid State Research*, Stuttgart
- [58] H.P. Klug, L.E. Alexander, *X-ray Diffraction Procedures*, 2nd edition John Wiley, New York (1974)
- [59] D. Balzar, H. Ledbetter, *Journal Applied Crystallography* **26** (1993) 97
- [60] D. Balzar, *Journal of Research of the National Institute of Standards and Technology* **98** (1993) 321
- [61] B.E. Warren, *X-ray Diffraction*, Addison Wesley, Reading, MA, (1969)
- [62] B. Marinkovic, R.R. de Avillez, A. Saavedra et al, *Materials Research* **4** (2001) 71
- [63] C. E. Krill, L. Helfen, D. Michels, H. Natter, A. Fitch, O. Masson, and R. Birringer *Physical Review Letters* **86** (2001) 842
- [64] Th. H. de Keijser, E. J. Mittemeijer, and H. C. F. Rozendaal, *J. Appl. Cryst.* **16** (1983) 309-316
- [65] Q.F. Xiao, E. Bruck, Z.D. Zhang, F.R. de Boer, K.H.J. Buschow, *Journal of Alloys and Compounds* **364** (2004) 315
- [66] Ai-Lin Xia, Hong-Liang Ge, et al, *Journal of Magnetism and Magnetic Materials* **305** (2006) 336
- [67] D. V. Louzguine-Luzgin, W. Zhang, A. Inoue, *Journal of Alloys and Compounds* **402** (2005) 78

- [68] O. Crisan, *Etude structurale et magnétique d'alliages amorphes et nanocristallins - Influence d'éléments terre rare*, PhD Thesis, Univ. Rouen, France (1998)
- [69] C.W. Chang, H.W. Chang, C.H. Chiu, W.C. Chang, *Journal of Applied Physics* **97** (2005) 10N117
- [70] J-M Le Breton, A Zorkovska and M Kasiarova, *J. Phys. Condensed Matter* **16** (2004) 5555
- [71] H.E. Kissinger, *Analytical Chemistry* **11** (1957)1702
- [72] J. Lyubina, O. Gutfleisch, R. Skomski, K.H. Muller, L. Schultz, *Scripta Materialia* **53** (2005) 469
- [73] K. Barmac, J. Kim, S. Shell, *Applied Physics Letters* **80** (2002) 4268
- [74] D. R. dos Santos, D.S. dos Santos, *Materials Research* **4** (2001) 47
- [75] R. De Biasi, M. Grillo, *Journal of Alloys and Compounds* **279** (1998) 233
- [76] J. Vasquez, P.L. Lopez-Aleman, P. Villares, R. Jiménez-Garay, *Journal of Alloys and Compounds* **61** (2000) 493
- [77] M. Iqbal, J.I. Akhter, H.F. Zhang and Z.Q. Hu, *J. Non-Cryst. Sol.* **354** (2008) 5363
- [78] M. Stoica, S. Kumar, S. Roth, S. Ram, J. Eckert, G. Vaughan and A.R. Yavari, *Journal of Alloys and Compounds* (2008) doi:10.1016/j.jallcom.2007.11.150 in press
- [79] O. Crisan, J.M. Le Breton, A.D. Crisan, G. Filoti, *Journal of Alloys and Compounds* **422** (2006) 194
- [80]] R. Pailler 'Caracterisation des solides poreux' Laboratoire des Composites Thermostructuraux, Universite de Bordeaux
- [81] F.E. Spada, F.T. Parker, *Journal of Applied Physics* **94** (2003) 5123
- [82] O. Crisan, J.M. Le Breton, M. Nogues, F. Machizaud, G. Filoti, *J. Phys : Condens. Matter* **14** (2002) 12599
- [83] O.Henkel, *Phys. Status Solidi*, **7** (1964) 919
- [84] E.P.Wohlfarth, *J. Appl. Phys.* **29** (1958) 595
- [85] P.I.Mayo, K.O'Grady, P.E.Kelly, J.Cambridge, I.L.Sanders, T.Yogi and R.W.Chantrell, *J. Appl. Phys.* **69** (1991) 4733
- [86] P. R. Bissell, R. W. Chantrell, H. J. Lutke-Stetzkamp, S. Methfessel, G. W. D. Spratt and E. P. Wohlfarth, *Journal de Physique*, Colloque C8, Supplement no **12** (1988) 1925

Annex I: Structural analysis of binary FePt alloys and determination of their hyperfine parameters.

As it has been mentioned earlier, to distinguish in XRD between the various FePt phases is very difficult due to the overlapping of main Bragg reflections of the fcc and fct phases. Besides that, from the phase diagram (Figure 2.1, Chapter 2) it can be observed that the A1 fcc disordered phase, at compositions rich in Fe, for Pt content below 35%, may transform into the $L1_2$ soft magnetic Fe_3Pt phase that has also fcc symmetry. The alloys with compositions rich in Pt form $FePt_3$ which has also $L1_2$ fcc symmetry ($Pm\bar{3}m$ space group).

On the other hand, as the hyperfine parameters of these phases are far from being fully explored, only very few FePt Mossbauer studies being reported, the assignation of various FePt phases based on interpretation of hyperfine parameters is a very difficult task.

In order to completely understand the nature of the observed contributions to the measured Mössbauer spectra of our samples, the exact hyperfine parameters of the FePt phases need to be known.

For this purpose, we have synthesized by rapid solidification from the melt a batch of ribbons, in the same experimental conditions as the FePtNbB ribbons, having the exact compositions: $Fe_{75}Pt_{25}$ (or Fe_3Pt), $Fe_{50}Pt_{50}$ (or FePt) and $Fe_{25}Pt_{75}$ (or $FePt_3$).

In order to stabilize the microstructure we have performed annealing at $750^\circ C$ for 48 hours. Both the as-cast and the annealed samples have been characterized by XRD, Mössbauer spectrometry and SQUID magnetometry.

The results are presented hereafter.

a. Case of Fe₃Pt

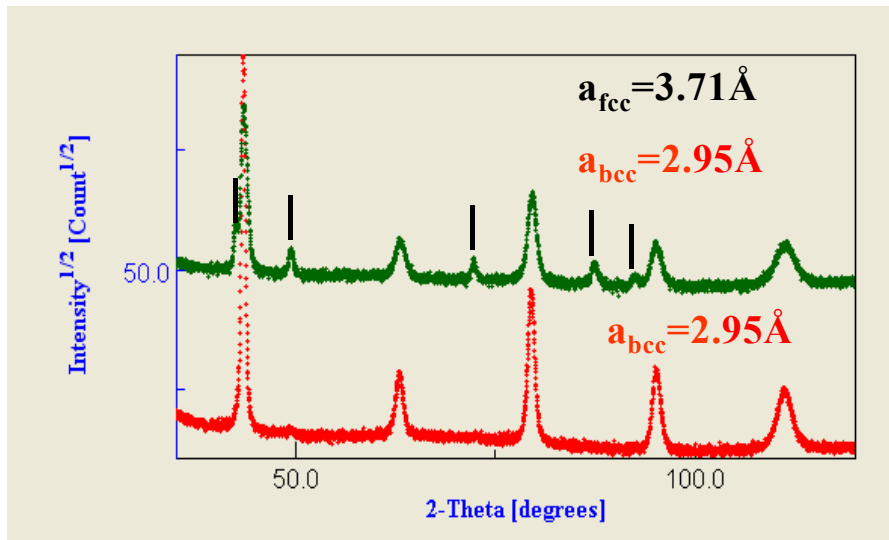


Figure 1. XRD spectrum of the as-cast and annealed Fe₃Pt binary alloy

The XRD diagram shows that the as-cast binary Fe₃Pt is crystallized. The observed Bragg lines correspond to a single phase and may be indexed in a body-centred-cubic symmetry. The bcc Fe₃Pt has the lattice parameter $a_{\text{bcc}}=2.956 \text{ \AA}$. In the XRD diagram of the annealed Fe₃Pt, we note the occurrence of additional Bragg lines, together with the ones from the as-cast state, belonging to the bcc symmetry. These supplemental Bragg lines, of smaller intensity than the bcc ones, could be indexed as belonging to a fcc phase with lattice parameter $a_{\text{fcc}}=3.707 \text{ \AA}$. The fitting with bcc and fcc phases is shown as an example in Figure 2.

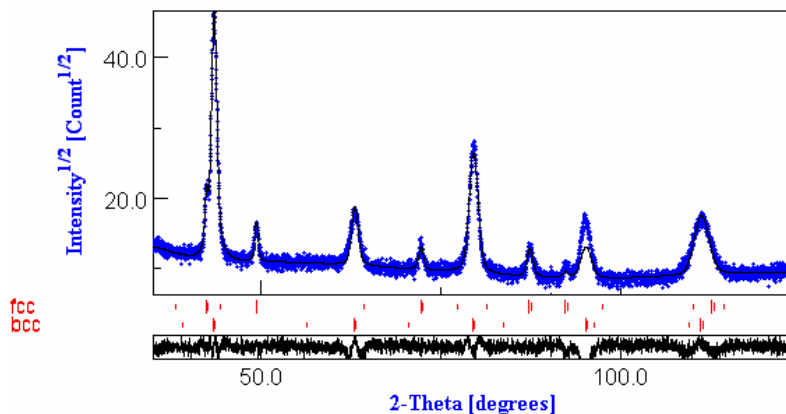


Figure 2. Fitted XRD diagram of the Fe₃Pt binary alloy annealed at 750°C for 48 hours. The only phases indexed are the bcc and fcc.

The 300K and 77K Mössbauer spectra of as-cast and annealed Fe₃Pt binary alloy are illustrated in Figure 3. The 300K Mössbauer spectrum of the as-cast Fe₃Pt presents a distributed magnetic sextet that has been fitted with 3 magnetic components. Since the XRD diagram shows that the sample has single phase, all the magnetic components are attributed to the same bcc Fe₃Pt phase. The large values of the hyperfine fields as well as the isomer shift and quadrupole shift obtained from the fit, are typical for bcc symmetry of Fe environments and confirm this assignment. The hyperfine parameters of the as-cast Fe₃Pt sample are listed in Table I. The average HF value is larger than the one of bcc α -Fe.

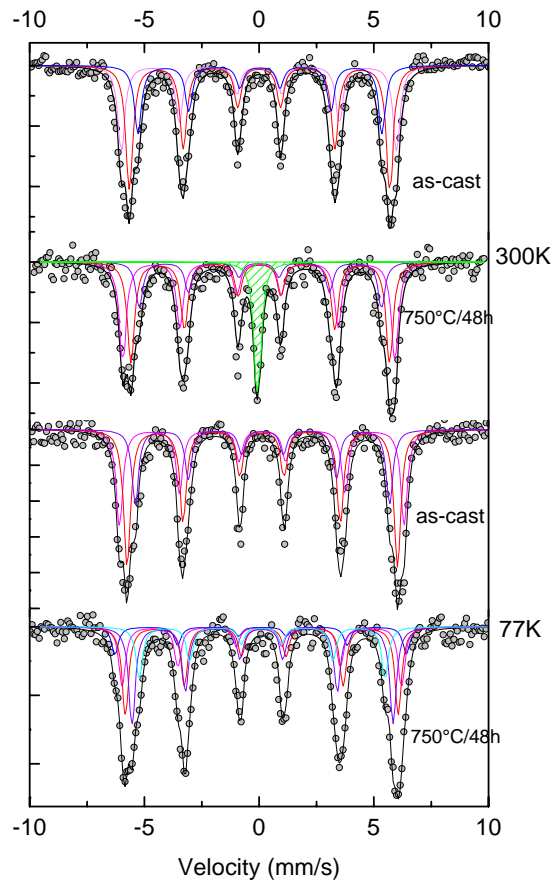


Figure 3. RT and 77K Mössbauer spectra of as-cast and annealed Fe₃Pt binary alloy

In the 300K Mössbauer spectrum of the annealed sample, apart from the 3 sextets from the as-cast, that are retrieved also in the annealed sample with almost the same hyperfine parameters, we have observed and fitted to the spectrum a paramagnetic singlet with hyperfine parameters similar to Fe environments in a fcc symmetry.

Table I: Hyperfine parameters of bcc and fcc phases at 300K and 77K for as-cast and annealed Fe₃Pt.

	IS (mm/s)	$\Gamma/2$ (mm/s)	2ε (mm/s)	B_{hf} (T)	%
As-cast 300K	0,15	0,18	-0,02	37.0	31
	0,16	0,18	0,02	35.0	45
	0,18	0,18	0	32.8	24
750°C/48h 300K	0.14	0.19	-0.01	36.6	36
	0.19	0.19	0.03	34.7	37
	0.17	0.19	0.06	32.5	17
	0.10	0.16	0	0	10
As-cast 77K	0,27	0.18	-0.02	38.3	31
	0,27	0.18	0.02	36.3	45
	0,29	0.18	0.18	34.2	24
750°C/48h 77K	0.27	0.18	-0.08	39.2	9
	0.22	0.18	0.12	37.5	18
	0.32	0.18	-0.08	36.7	27
	0.29	0.18	0.05	35.1	30
	0.28	0.18	0.03	33.0	16

This paramagnetic component has a relative intensity of 10% and is attributed to fcc Fe₃Pt. We have thus confirmed the XRD measurements where we have seen the occurrence of the additional lines belonging to the fcc Fe₃Pt phase. The annealing causes a partial bcc to fcc phase transformation and this fcc phase, in the case of Fe₃Pt, seems to be the same disordered phase as documented in the series of annealed *Ib* samples.

At 77K, the as-cast spectrum is similar to the 300K one and has been fitted with the same model, i.e. 3 sextets with similar hyperfine parameters and HF values higher

than in the 300K as-cast spectrum. The 77K spectrum of annealed Fe₃Pt shows more complicated features. The singlet is no more observed and the spectrum has been fitted to 5 sextets, 3 of them belonging to the bcc phase and the other two to the fcc Fe₃Pt. With decreasing the temperature, the fcc phase becomes magnetically ordered. The same situation has been observed in the case of *Ia* as-cast sample. All the obtained hyperfine parameters are consistent throughout the series of fittings and have been used to correctly identify the phases in the FePtNbB alloys.

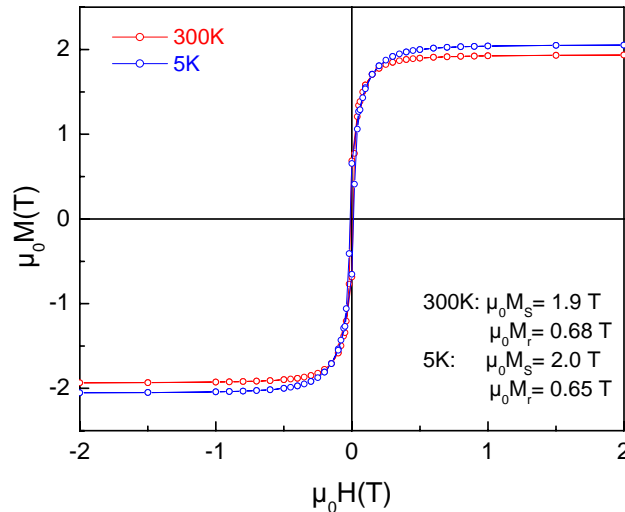


Figure 4: 5K and 300K hysteresis loops in parallel applied field for Fe₃Pt as-cast alloy

From magnetic point of view, the Fe₃Pt alloy in the as-cast state is a soft magnetic one, as proven by the 5K and 300K hysteresis loops, shown in Figure 4. The saturation magnetization reaches 1.9 T while the remanence is about 0.6 T.

b. Case of FePt

Figure 5 depicts the XRD diagrams of the as-cast and annealed FePt binary alloys. Both diagrams were fitted with a single phase, namely the face-centred-tetragonal *L1₀* FePt. The as-cast sample has larger Bragg reflections as expected, while the lines of the annealed sample are well separated. The lattice parameters obtained for the fct *L1₀* FePt were $a=3.862\text{\AA}$ and $c=3.726\text{\AA}$ for both samples. The 300 K Mössbauer spectra of the as-cast and annealed FePt are illustrated in Figure 6. They both exhibit only magnetic feature with narrow absorption lines. As in the XRD diagrams only one, same, single phase has been identified, the spectra were both fitted with one sextet.

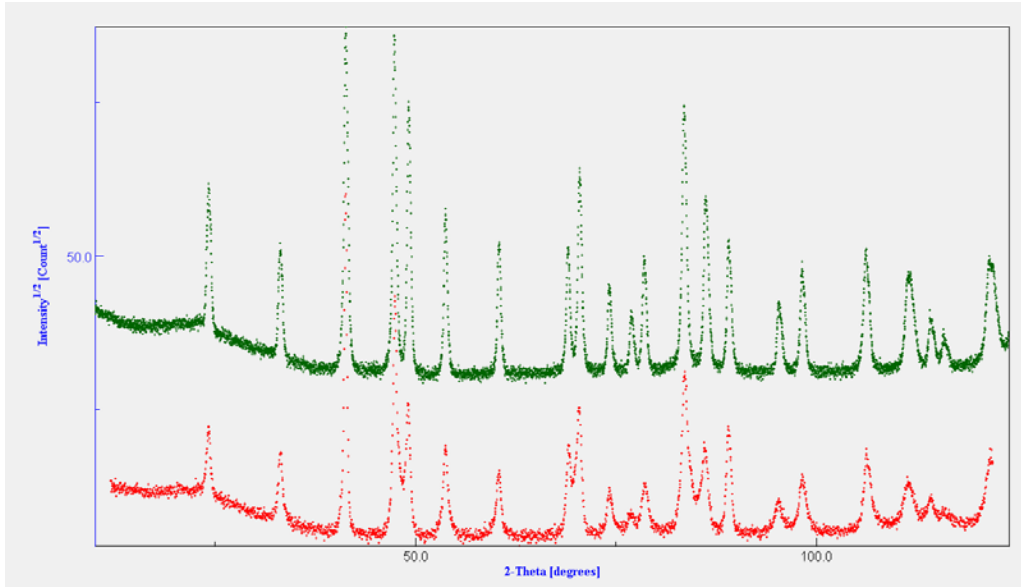
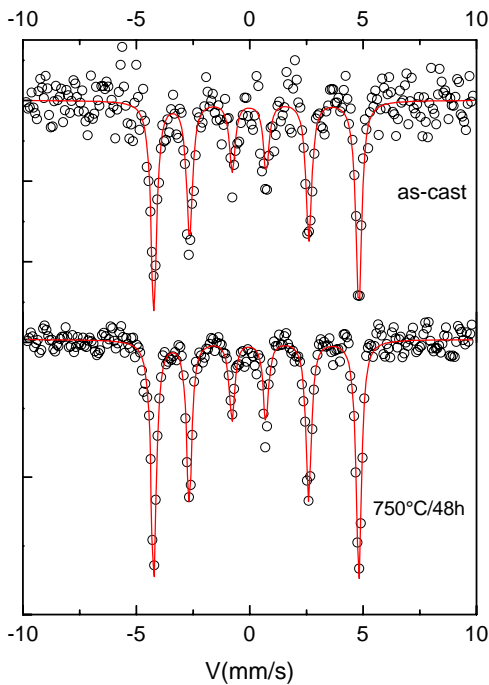


Figure 5: XRD diagrams of the as-cast and annealed FePt binary alloys.



	IS (mm/s)	$\Gamma/2$ (mm/s)	QS (mm/s)	B_{hf} (T)	%
as-cast	0.28	0.16	0.31	27.8	100
annealed	0.28	0.15	0.32	27.8	100

Figure 6: 300K Mössbauer spectra of the as-cast and annealed FePt binary alloys and their hyperfine parameters.

The hyperfine parameters are almost the same, for the two samples. The linewidth is slightly narrower in the case of the annealed sample while the HF is the same, within the experimental errors. The quadrupole shift of around 0.3 mm/s proves that it is a tetragonal type of Fe environment. This study provided us with the correct hyperfine

parameters to use for the correct indexation of the hard magnetic phase in the highly complex Mössbauer spectra of the FePtNbB alloys. On the other hand, the fact that the hyperfine parameters do not change upon annealing proves the high stability and high degree of ordering of the tetragonal phase.

The magnetic state of the FePt binary alloy has again been studied using SQUID magnetometry. Figure 7 presents the as-cast and annealed 300K and 5K hysteresis loops of FePt.

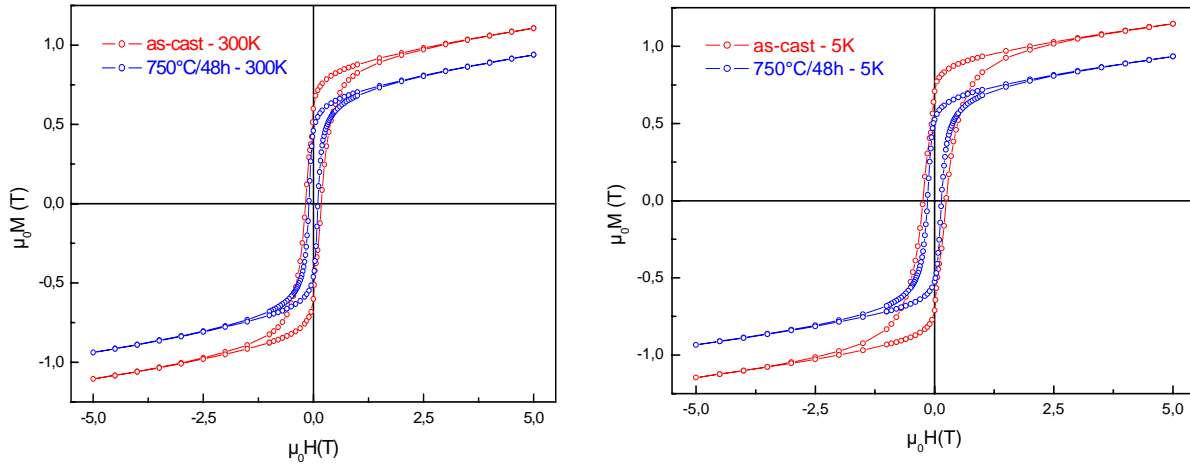


Figure 7: 300K and 5K hysteresis loops of as-cast and annealed FePt. The obtained magnetic parameters are plotted in the Table III.

Table III: Magnetic parameters for as-cast and annealed FePt samples.

	$\mu_0 H_C$ (T)	$J_r = \mu_0 M_r$ (T)
As-cast – 300K	0.18	0.60
As-cast - 5K	0.24	0.71
750°C/48h – 300K	0.10	0.46
750°C/48h – 5K	0.14	0.52

It can be observed that the loops show hard magnetic features with no saturation at the highest applied field of 5 T. Maximum magnetization is slightly lower in the annealed sample (0.93 T) than in the as-cast sample (1.15 T). Both the remanence and the coercivity in the as-cast state are slightly higher than their counterparts from the annealed sample. It should be noted nevertheless that the coercivity is lower than in the annealed FePt – 1 and FePt – 2 samples. This proves once again that the good coercivity in that samples is not only due to the hard magnetic phase but to the exchange spring

mechanisms involving the hard and the soft magnetic phases and to the refined microstructure with lower than 30 nm grain sizes, as we have discussed in Chapter 4.

c. Case of FePt₃

The XRD diagrams of FePt₃ are presented in Figure 8 for both as-cast and annealed samples. Like in the previous case a single phase has been identified in both diagrams, i.e. the cubic $L1_2 - \text{FePt}_3$ with the lattice parameter $a = 3.873\text{\AA}$ for both diagrams.

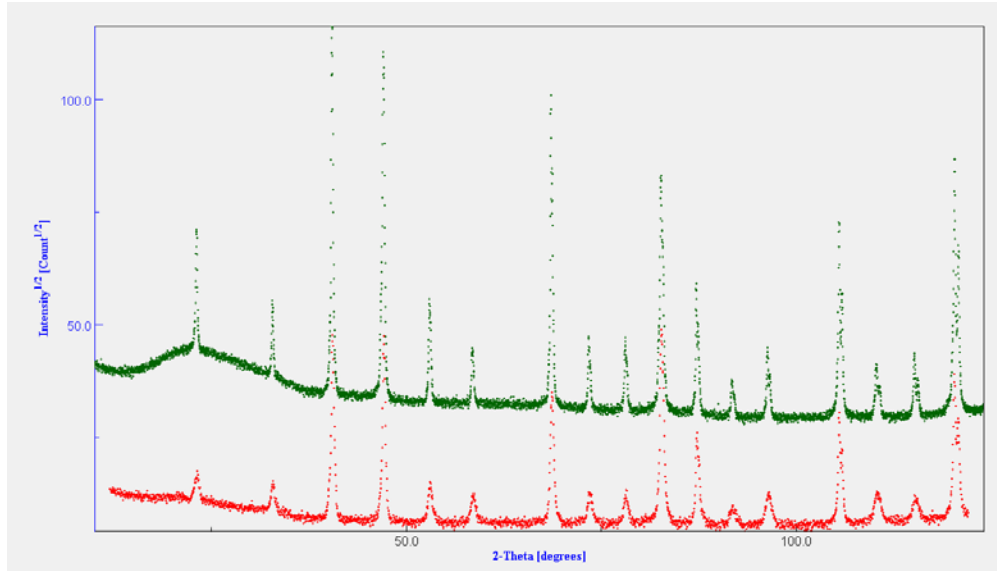


Figure 8: The XRD diagrams of as-cast and annealed FePt₃ samples.

The Mössbauer spectra for the as-cast and annealed FePt₃ samples are plotted in Figure 9. It can be seen that at 300K both as-cast and annealed samples show only one paramagnetic contribution. This is to be expected due to the low Fe content in the sample. The values of the isomer shift and quadrupole shift suggest a cubic Fe environment. Therefore, this component is attributed to magnetically disordered $L1_2$ FePt phase. At 77K in the as-cast state the paramagnetic contribution transforms, like in the case of Fe₃Pt fcc, into two sextets of large hyperfine field of about 27-28 T. All the hyperfine parameters are depicted in Table IV. It is to be noted the high isomer shift value while the quadrupole shift is close to 0. We note thus that at 77K the $L1_2$ FePt phase become magnetically ordered. In the annealed sample, the situation is almost similar, but here the magnetic disorder-order transformation is not complete at 77K, a small paramagnetic component (10%) with large isomer shift value still remaining in the microstructure, as evidenced by the Mössbauer spectrometry.

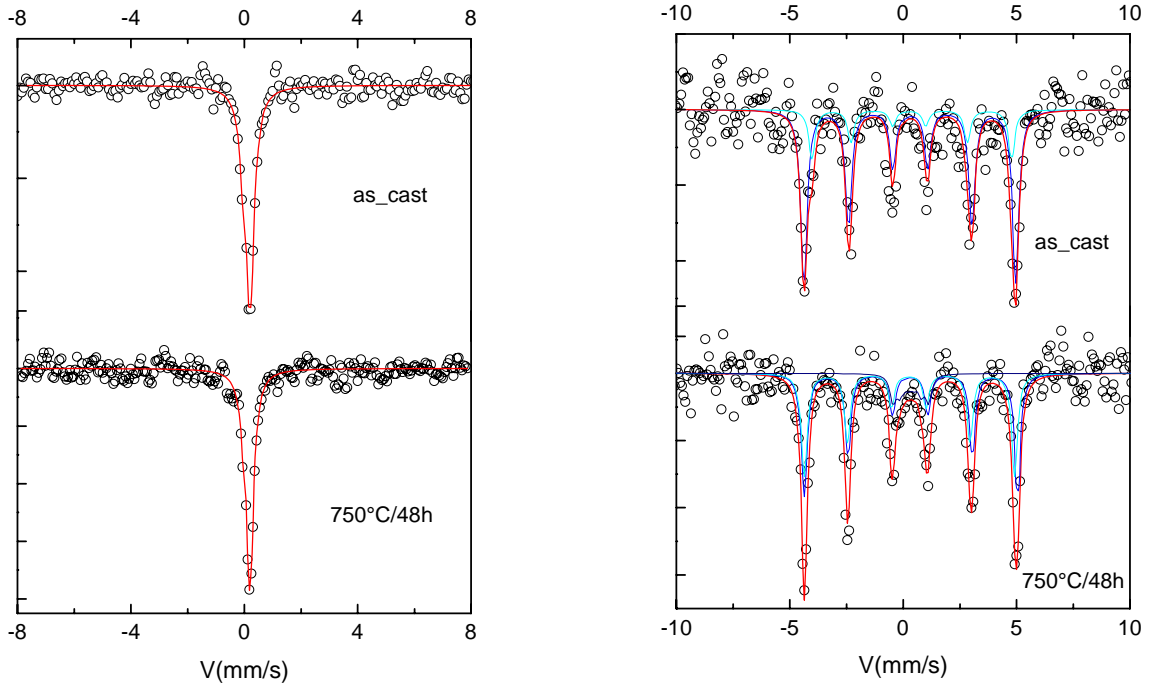


Figure 9: 300K (left) and 77K (right) Mössbauer spectra of as-cast and annealed FePt₃ samples.

Table IV: Hyperfine parameters of 300K and 77K Mössbauer spectra of as-cast and annealed FePt₃ samples.

	IS (mm/s)	$\Gamma/2$ (mm/s)	QS (mm/s)	B_{hf} (T)	%
RT_as-cast	0.31	0.17	0.08	0	100
77K_as-cast	0.45	0.17	-0.02	28.7	78
	0.47	0.17	0.11	27.1	22
	IS	$\Gamma/2$ (mm/s)	QS (mm/s)	B_{hf} (T)	%
RT_annealed	0.31	0.16	0.013	0	100
77K_annealed	0.47	0.16	0.03	28.9	49
	0.41	0.16	0.03	28.5	41
	0.48	0.16	0.01	4.6	10

Annex II: List of published articles

a) Articles ISI

1. O. Crisan, J.M. Greneche, J.M. Le Breton, **A.D. Crisan**, Y. Labaye, L. Berger, G. Filoti, "Experimental and Monte Carlo study of the magnetic behavior of nanocrystalline Finemet alloys", *European Physical Journal B* **34** (2003) 155-162
2. **A. D. Crisan**, J. M. Le Breton, O. Crisan, G. Filoti, "Metastable phases and crystallization products in nanocrystalline Finemet-type alloys with RE addition", *J. Optoelectron. Adv. Mater.* **5**(3) (2003) 709-711
3. M. Angelakeris, O. Crisan, E. Papaioannou, N. Vouroutzis, J. Tsiaoussis, E. Pavlidou, **A.D. Crisan**, I. Kostic, N. Sobal, M. Giersig, N. K. Flevaris, "Fabrication of novel magnetic nanostructures by colloidal bimetallic nanocrystals and multilayers", *Materials Science and Engineering C* **23** (2003) 873-878
4. O. Crisan, M. Angelakeris, E. Papaioannou, **A.D. Crisan**, N.K. Flevaris, N. Vouroutzis, E. Pavlidou, I. Kostic, N. Sobal, M. Giersig, "Magnetic nanostructures obtained by colloidal crystallization onto patterned substrates", *J. Magn. Magn. Mater.* **272-276** (2004) e1285-e1287
5. O. Crisan, J.M. Le Breton, **A. D. Crisan**, F. Machizaud, M. Noguès, "Influence of Gd addition on the magnetism and structure of Finemet-type nanocrystalline alloys", *J. Magn. Magn. Mater.* **272-276** (2004) e1396-e1397
6. O. Crisan, J.M. Le Breton, **A.D. Crisan**, G. Filoti, "Study of crystallization processes in Gd-substituted Finemet alloys", *J. Alloys & Comp.* **422** (1-2) (2006) 194-202
7. O. Crisan, **A.D. Crisan**, I. Skorvanek, J. Kovac "Magnetism and Structural Phase Transformation in Fe / Fe oxide Nanopowders", *J. Phys.: Conference Series* (2008) accepted for publication

b) Book chapter:

8. O. Crisan, J.M. Greneche, Y. Labaye, L. Berger, **A.D. Crisan**, M. Angelakeris, J.M. Le Breton, N.K. Flevaris, « Magnetic Properties of Nanostructured Materials: Monte Carlo simulation and experimental approach for nanocrystalline alloys and core-shell nanoparticles », in: M. Miglierini, P. Svec and B. Idzikowski, editors: « Properties

and Applications of Nanocrystalline Alloys Prepared from Amorphous Precursors », NATO Science Series II **184** (2004) 253-266, Kluwer Academic Publishers.

c) Articles related to / issued from the thesis

9. O. Crisan, **A.D. Crisan**, N. Randrianantoandro, R. Nicula and E. Burkel, “Crystallization processes and phase evolution in amorphous Fe-Pt-Nb-B alloys”, *J. Alloys & Comp.* **440** (1-2) (2007) L3-L7
10. **A.D. Crisan**, R. Nicula, O. Crisan, and E. Burkel, “Thermally and pressure activated phase evolution in Fe-Pt-Nb-B melt spun ribbons“, *Materials Science & Engineering C: Biomimetic and Supramolecular Systems* **27** (2007) 1280-1282
11. **A.D. Crisan**, O. Crisan, N. Randrianantoandro, M. Valeanu, M. Morariu and E. Burkel, “Crystallization Processes in Fe-Pt-Nb-B Melt Spun Ribbons”, *Materials Science & Engineering C: Biomimetic and Supramolecular Systems* **27** (2007) 1283-1285
12. **A. D. Crisan**, O. Crisan, I. Skorvanek, N. Randrianantoandro, “Synthesis and magnetic properties of Fe₅₁Pt₂₇Nb₂B₂₀ melt spun ribbons”, *J. Optoelectron. Adv. Mater.* **10** (4) (2008) 786-789

Annex III : Communications at international conferences related to the thesis:

1. O. Crisan, M. Valeanu, **A.D. Crisan**, F. Lifei, N. Randrianantoandro and E. Burkel, “Formation and stability of magnetic nanostructures in nanocomposite melt-spun Fe-Pt-Nb-B ribbons”, 3rd International Conference on Materials for Advanced Technologies and 9th International Conference on Advanced Materials, ICMAT & ICAM, Singapore, 2005
2. O. Crisan, N. Randrianantoandro, J.M. Greneche, **A.D. Crisan**, M. Valeanu and E. Burkel, “Synthesis and characterization of melt spun Fe-Pt-Nb-B nanocomposite magnets”, presented at the 12th International Symposium on Metastable and Nano Materials ISMANAM 05, Paris, France
3. **A.D. Crisan**, R. Nicula, O. Crisan, and E. Burkel, “Thermally and pressure activated phase evolution in Fe-Pt-Nb-B melt spun ribbons“, presented at „European Materials Research Society E-MRS 06 Spring Meeting“, Nice, may-june 2006
4. **A.D. Crisan**, N. Randrianantoandro, M. Valeanu, M. Morariu, O. Crisan and E. Burkel, “Crystallization processes in Fe-Pt-Nb-B melt spun ribbons“, presented at „European Materials Research Society E-MRS 06 Spring Meeting“, Nice, may-june 2006
5. **A.D. Crisan**, R. Nicula, O. Crisan and E. Burkel, “Pressure-assisted Thermal Phase Evolution in Fe-Pt-Nb-B Alloys Studied with in-situ X-ray Diffraction of Synchrotron Radiation”, presented at 8th International School and Symposium on Synchrotron Radiation in Natural Sciences ISSRNS-8, Zakopane, 2006
6. **A.D. Crisan**, O. Crisan, N. Randrianantoandro, M. Valeanu, M. Morariu, and E. Burkel, “Thermal Analysis of Crystallization Processes in Fe-Pt-Nb-B Melt Spun Ribbons”, presented at 8th International School and Symposium on Synchrotron Radiation in Natural Sciences ISSRNS-8, Zakopane, 2006
7. O. Crisan, **A.D. Crisan**, R. Nicula and E. Burkel, “*In-situ* synchrotron XRD studies of crystallization processes in amorphous Fe-Pt-Nb-B alloys”, presented at the International Conference on Solid Compounds of Transition Elements SCTE06, Krakow, 2006

8. N. Randrianantoandro, O. Crisan, **A. D. Crisan**, J.-M. Greneche, “Magnetic properties of melt-spun nanocomposite FePtNbB ribbons”, International Symposium on Metastable and Nano Materials, ISMANAM 2006, Warsaw, Poland 2006
9. O. Crisan, **A. D. Crisan** and N. Randrianantoandro, “Formation and stability of magnetic nanostructures in nanocomposite melt-spun Fe-Pt-Nb-B ribbons”, Condensed Matter and Materials Physics CMMP Conference, Leicester, UK 2007
10. **A. D. Crisan**, N. Randrianantoandro, I. Skorvanek, O. Crisan, “Nanocrystalline Fe-Pt-Nb-B alloys as novel nanocomposite magnets” 4th International Workshop on Amorphous and Nanostructured Materials, Iasi, Romania, 2007
11. **A.D. Crisan**, O. Crisan, I. Skorvanek, N. Randrianantoandro, “Synthesis and magnetic properties of Fe₅₁Pt₂₇Nb₂B₂₀ melt spun ribbons” 5th International Conference on New Research Trends in Material Science ARM-5 Sibiu, Romania 2007
12. **A.D. Crisan**, N. Randrianantoandro, O. Crisan, “FePt-based nanocomposite ribbons as exchange-coupled magnets”, IEEE International Magnetism Conference, Madrid, Spain, May 2008
13. **A.D. Crisan**, N. Randrianantoandro, O. Crisan, R. Nicula, “Pressure and temperature activated phase evolution in FePt Based nanocrystalline ribbons studied by energy dispersive X-ray diffraction of synchrotron radiation”, 21st International Conference on X-ray and Inner Shell Processes, Paris, France, June 2008

Résumé :

Ce travail de thèse est une contribution à l'étude et au développement d'aimants permanents de type spring magnet. Ces matériaux sont constitués de grains magnétiques durs dispersés dans une matrice magnétique douce. Le couplage des grains magnétiques durs à travers la matrice douce permet d'augmenter significativement la coercivité et l'aimantation rémanente et par conséquent la valeur du produit $(BH)_{\max}$, facteur de qualité ou de mérite des aimants permanents. L'objectif de ce travail est de réaliser ce type d'aimant permanent à partir d'alliages nano cristallisés à base de FePt. Pour cela, la méthode de trempe ultra-rapide sur roue a été utilisée pour produire un précurseur métastable à base de FePtNbB, suivi d'un traitement de dévitrification partielle permettant d'obtenir des grains nano cristallisés de phase dure, de symétrie quadratique à face centrée (phase $L1_0$) avec une forte anisotropie uniaxiale (7MJ/m^3), dispersés dans une matrice résiduelle magnétiquement douce de composition Fe(PtNb). Les mesures par calorimétrie différentielle et diffraction in situ du rayonnement synchrotron en température et sous pression ont permis d'optimiser les paramètres de cristallisation. Les propriétés structurales des échantillons ont été étudiées par diffraction de rayons X, microscopie électronique à transmission, analyse dispersive en énergie X et spectrométrie Mössbauer du ^{57}Fe alors que les caractéristiques magnétiques ont été mesurées avec des magnétomètres SQUID et VSM. Les performances obtenues à 300K montrent que ces échantillons sont de bons candidats comme aimants permanents: coercivité de 850kA/m, champs rémanent de 0.7T et facteur de mérite $(BH)_{\max}$ de 69kJ/m^3 .

Mots clés : alliages nanocristallisés, FePt, couplage d'échange magnétique, *spring magnet*, aimant permanent

Abstract :

The present work is a contribution to the study and development of a new class of permanent magnets based on the exchange spring effect. These materials are made of hard magnetic grains dispersed in a soft magnetic matrix. The coupling of hard magnetic grains through the soft matrix allows a significant improvement of the coercivity and remanence, and by consequence, an improved maximum energy product may be obtained in these alloys. The aim of this work is to synthesize this type of magnetic material starting with nanocrystalline FePt-based alloys. The rapid solidification by melt spinning method has been used to cast metastable precursor alloys with composition FePtNbB. After annealing, a microstructure made of hard magnetic nanograins of face-centred-tetragonal symmetry ($L1_0$ phase) with high uniaxial magnetic anisotropy (7MJ/m^3), dispersed in a residual soft magnetic phase with composition FePt(NbB) has been obtained. The differential scanning calorimetry studies as well as in situ X-ray diffraction of synchrotron radiation in temperature and applied pressure have allowed the optimization of parameters of crystallization of the metastable precursor. The structural parameters of the samples were investigated using X-ray diffraction, transmission electron microscopy, energy dispersive spectroscopy and ^{57}Fe Mössbauer spectrometry while the magnetic parameters were determined using VSM and SQUID magnetometry. The performances obtained at 300K, coercivity 850kA/m, remanence 0.7 T and $(BH)_{\max}$ 69 kJ/m^3 show that these alloys are good candidates as permanent magnets.

Keywords: nanocrystalline alloys, FePt, exchange coupling, exchange-spring, permanent magnet